



THE UNIVERSITY *of* EDINBURGH

This thesis has been submitted in fulfilment of the requirements for a postgraduate degree (e.g. PhD, MPhil, DClinPsychol) at the University of Edinburgh. Please note the following terms and conditions of use:

This work is protected by copyright and other intellectual property rights, which are retained by the thesis author, unless otherwise stated.

A copy can be downloaded for personal non-commercial research or study, without prior permission or charge.

This thesis cannot be reproduced or quoted extensively from without first obtaining permission in writing from the author.

The content must not be changed in any way or sold commercially in any format or medium without the formal permission of the author.

When referring to this work, full bibliographic details including the author, title, awarding institution and date of the thesis must be given.

The physiology of *Escherichia coli* at high osmolarity and its use in industrial ethanol production

Keiran Stevenson

A thesis presented for the degree of
Doctor of Philosophy



THE UNIVERSITY
of EDINBURGH

School of Biological Sciences
Scotland
June, 2019

Abstract

Biofuels are becoming increasingly important in the light of climate change, increasing energy demands and higher fuel prices. Their production must be carefully balanced against the production of foods and use of fresh water, both of which are consumed by crop based biofuels such as corn ethanol. One proposed solution is to instead use waste materials such as plant matter including wood offcuts and plant trimmings. This waste can be turned into syngas (a mix of CO and H_2) and converted to ethanol using microorganisms. Production of ethanol using microorganisms however, is complicated as the ethanol produced by the cells becomes toxic at higher concentrations, inhibiting their growth and further production. The usual method of keeping the toxicity down to allow further production is to continuously distil ethanol off at low concentrations and consequently, a high cost.

Since the mechanisms of ethanol damage to microbes are similar to those that occur during osmotic challenge: damage to the membrane, cytoplasmic dehydration, and protein unfolding, I hypothesized that we can use knowledge of osmoregulatory mechanisms to increase the resistance of cells to ethanol damage and decrease distillation costs. While working under this hypothesis I had to address some of the challenges one faces when understanding the physiology and growth of microbes, and for the purpose I have developed a number of useful techniques; a method for calibrating optical densities to cell number, a neural network for identifying cells and determining their concentrations via microscope imaging and a simple particle diffusion simulation for correcting errors due to confinement of particles within cells. In addition, I have produced a simplified model of industrial production to help evaluate economic impacts that changes to the growth of microbes and the plant process may have.

To study any useful links between osmolarity and ethanol resistance, I chose to use *Escherichia coli* as the model organism due to the large amount of data available on its osmoregulatory mechanisms. It has been long known that when bacteria do grow at high but not lethal osmolarity, they grow at a reduced rate which, even if it increases the ethanol resistance, may have a detrimental effect on the desired production rates. So therefore, in addition to testing the ethanol tolerance of the bacteria under different osmotic conditions, and as a second focus of this project, I have tried to understand why the reduction in growth rates occurs, with the hope of mitigating this effect. This will offer a better understanding of osmotic growth and provide useful insights for industrial bio-production. To this end, I have tried to discern some of the possible reasons for this slower growth by measuring various cell physiological parameters such

as batch-culture yield, cytoplasmic diffusion and proteome allocation using my newly developed techniques. I have found a reduction in the cell yield with increasing osmolarity of 50% with an increase of 1Osm of osmotic agent, a slight decrease in cytoplasmic diffusion and a slight decrease in RNA content at high osmolarity. I have also proposed a coarse grained model of proteome partitioning to help integrate these results and explain growth at high osmolarity. It is still to be determined if, as a whole, the changes observed explain fully the reduction in growth.

When it comes to ethanol resistance, and contrary to my hypothesis, I found that increasing the osmolarity of the medium with sucrose or NaCl reduced the ethanol resistance. However, I found that the *proW* gene provides significant ethanol resistance, indicating glycine betaine, or another substrate for this transporter, is highly useful as a protectant. And this transporter is a potential candidate for overexpression. A reduction in growth temperature also provides significant solvent tolerance at the expense of a reduction in growth rate and hence production.

Declaration

I declare that the thesis has been composed by myself and that the work has not been submitted for any other degree or professional qualification. I confirm that the work submitted is my own, except where work which has formed part of jointly-authored publications has been included. My contribution and those of the other authors to this work have been explicitly indicated below. I confirm that appropriate credit has been given within this thesis where reference has been made to the work of others.

The work presented in Chapter 3.2 was previously published in Nature Scientific Reports as "General calibration of microbial growth in microplate readers" by Keiran Stevenson[†] (author of this thesis and declaration), Alexander F. McVey[†], Ivan B.N. Clark[‡], Peter S. Swain[‡] and Teuta Pilizota[†]. This study was conceived of by all authors. I carried out all experiments involving bacteria and beads with the exception of SI Figure 1(A).

Keiran Stevenson
November 29th, 2019

[†]Centre for Synthetic and Systems Biology, School of Biological Sciences, University of Edinburgh, Roger Land Building, Alexander Crum Brown Road, Edinburgh, EH9 3FF, United Kingdom

[‡]Centre for Synthetic and Systems Biology, School of Biological Sciences, University of Edinburgh, CH Waddington Building, Mayfield Road, Edinburgh EH9 3JD, UK

Acknowledgements

I would like to thank my supervisor, Dr Teuta Pilizota, for her unwavering guidance and belief during my time working with you. Your contagious enthusiasm and drive to expand our knowledge helped me get through what has been my greatest challenge and achievement so far.

I'd also like to thank the other members of the Pilizota lab for making it a fun place to work with a relaxed atmosphere and a mix of disciplines. In particular I'd like to thank Dr Jerko Rosko for being with me through every step since I joined and showing me how to deal with some of the unique experimental challenges.

Thanks to the rest of my supervisory team, Prof. Rosalind Allen and Dr Ian Little for their guidance and support over the years. Additional thanks to Dr Ian Little for his guidance and supervision during my internship at Ineos O&P where I developed the industrial model presented in Chapter 4.1.

Contents

1	Introduction	1
1.1	Motivation and outline	1
1.2	Industrial ethanol production	2
1.2.1	Syngas production through gasification	3
1.2.2	<i>Clostridium ljungdahlii</i> and syngas conversion to ethanol	3
1.2.3	Beer distillation is the most expensive part of production	6
1.2.4	Azeotrope dehydration is the final step of production	7
1.3	Osmoregulation in <i>E.coli</i>	9
1.3.1	<i>E.coli</i> 's response to a hyperosmotic shock	9
1.3.2	Energy consumption of osmoregulation	11
1.3.3	Known physiological changes of proteome allocation and diffusion in <i>E.coli</i>	12
1.4	Osmoregulation and ethanol resistance	15
1.4.1	Membrane based damage and protection	15
1.4.2	Protein unfolding and protection by osmolytes	16
1.4.3	Using osmoregulation for in ethanol resistance	16
2	Methods	19
2.1	Strains and media	19
2.1.1	Bacterial strains	19
2.1.2	P1 transduction for construction of BW25113-GFP- μ NS	19
2.1.3	Media	21
2.1.4	Preparation of medium osmolarities	23
2.1.5	Cell growth	23
2.1.6	Cell growth in platereader	24
2.1.7	Growth rate analysis	24
2.2	Single particle diffusion microscopy	25
2.2.1	Induction of particle expression	25
2.2.2	Microfluidic slide preparation	25
2.2.3	Cell imaging for diffusion	26
2.3	Optical Density calibration	26
2.4	Ribosome and protein content measurements	26
2.5	Ethanol tolerance measurements	27

3	Developed methods	29
3.1	Single particle diffusion measurement	29
3.1.1	Constructing of a computer simulation of ideal particles . .	29
3.1.2	Calculating diffusion constant from using mean squared displacement	30
3.1.3	Confirmation of simulation predictive capacity	31
3.1.4	Estimating the sample size required	31
3.1.5	Error in diffusion estimation due to confinement of particles	37
3.1.6	Radius of gyration minimises error	37
3.1.7	Particle localization from microscopy videos	38
3.2	Optical density calibration	40
3.2.1	Introduction to publication	40
3.2.2	Conclusions relevant to this thesis	40
3.2.3	Publication: General calibration of microbial growth in microplate readers	40
3.3	Neural network for brightfield cell counting	62
3.3.1	Introduction	62
3.3.2	Network training and verification	64
4	Industrial ethanol production	69
4.1	Model of industrial ethanol production to calculate potential cost savings	69
4.1.1	Motivation	69
4.1.2	Model components	69
4.1.3	Sensitivity analysis	74
4.1.4	Conclusions for production	76
4.2	Characterising <i>E.coli</i> ethanol tolerance	78
4.2.1	Temperature dependence of ethanol tolerance	78
4.2.2	Characterising medium supplementation on ethanol tolerance	78
4.2.3	Osmotic increase	80
4.2.4	Ethanol tolerance of osmoregulatory knockout strains . . .	80
4.2.5	Discussion	81
5	<i>E.coli</i> physiology at high osmolarity	85
5.1	Proteome allocation	85
5.1.1	Ensuring exponential growth	86
5.1.2	Verifying previously observed measurements of proteome fraction	86
5.1.3	Changes to protein/RNA ratio at high osmolarity	88
5.2	Cell yield at high osmolarity	91
5.2.1	Yield as measured by optical density	91
5.2.2	Yield as measured by cell concentration	91
5.3	Diffusion constant changes at high osmolarity	93
5.4	Coarse grained model of growth at high osmolarity	95

5.4.1	Model description	95
5.4.2	Qualitative testing of model	98
5.4.3	Model fitting	100
5.5	Discussion	102
6	Discussion and future work	103
6.1	Improving ethanol tolerance	103
6.2	<i>E.coli</i> physiology at high osmolarity	104
6.3	Future directions	104

Chapter 1

Introduction

1.1 Motivation and outline

The intended goal of this thesis and project is the enhancement of the ethanol tolerance of the *Clostridium ljungdahlii* strains used by IneosBio for the production of ethanol from the fermentation of bio-syngas as described in section 1.2. The distillation of low concentrations of ethanol produced by the bacteria has a significant energy requirement and therefore represents a part of the process that could be improved to increase the profit margin.

Some of the cell damage caused by ethanol is similar to that caused by conditions of high osmolarity, as detailed in section 1.4. Thus, I hypothesised that our research could be used to improve the industrial strains. One of the major consequences of growth at high osmolarity is a significant reduction in cell growth rate, a process which is still poorly understood, and for an industrial bacterium this would result in a lower production rate and therefore may mitigate any improvement that increased ethanol resistance may confer. As such I also chose to look into methods of understanding or even improving the growth rate while conferring enhanced ethanol resistance. Since a majority of our research and background in osmolarity is from the model organism *Escherichia coli* I chose to start with that and plan move to the proprietary strain on site in the IneosBio facility should I find a promising lead.

My thesis therefore progressed on two fronts that would help inform each other using *E.coli* for all the experiments therein. On the first front I would proceed to define the limits of the *E.coli* ethanol tolerance under different conditions including media composition and osmolarity, followed by the use of osmoregulatory mutants to help focus my study onto specific, potentially useful components of the osmoregulatory network in chapter 4.2.

Additionally, I undertook a short project while working under the guidance of Dr.Ian Little at Ineos P&O in Grangemouth, Scotland. During this project I constructed an economic model to relate any changes to the bacterial growth and ethanol tolerance to a theoretical cost saving in order to put any potential improvements in a proper context within a bio-gasification and fermentation plant. The model and its results are described in chapter 4.1.

On the second front, I attempted to improve the understanding of osmo-

regulation in *E.coli* by probing the changes to cytoplasmic diffusion, proteome allocation and cellular yield to identify reasons for reduced growth rate under hyperosmotic conditions in chapter 5. In brief my hypothesis is based on the following observations: (i) transporters and enzymes consume energy or carbon source meaning that there is less for building cells giving a reduction in cell yield (ii) transport and synthesis of molecules to reverse the osmotic gradient increases the concentration of components in the cytoplasm, which may limit the movement (diffusion) of other molecules, (iii) the allocation of ribosomes to synthesising different components of the osmoregulatory network will lower the number available to synthesis of new ribosomes and cell construction machinery. Based on my experiments attempting to measure these three factors I have made modifications to a previously developed coarse grained model, which explains growth rate variation in response to different carbon sources, in chapter 5.4, to try and determine if the effects observed can explain the reduction in growth rate.

I will first give an introduction of the various components that made up this project, as well as outlining the background upon which I based my hypothesis to explain the reduction of growth rate at high osmolarity. Following this I developed a number of methods, presented in a separate chapter Developed Methods, to address some of the challenges one faces when understanding physiology and growth of microbes. These methods are as follows: (i) a method for calibrating optical densities in chapter 3.2, (ii) a neural network for identifying cells in chapter 3.3 and determining their concentrations via microscope imaging, (iii) a simple particle diffusion simulation for correcting errors due to confinement of particles within cells in chapter 3.1.

1.2 Industrial ethanol production

Ethanol is a widely used commodity chemical, with the single largest use being that as a fuel additive for gasoline products. In some countries it has also replaced petroleum entirely as a fuel for cars, often in places where plant based material is common such as Brazil [1] where sugar cane provides the raw material for fermentation. While the conversion of plant based materials to ethanol has a long history, particularly in Europe, through the production of beer as way of sterilising water [2] it has some significant drawbacks. Specifically, the production of ethanol via fermentation of sugar takes significant resources away from food production by utilisation of cropland, irrigation water and fertiliser [3,4]. Pressure on food production and water conservation is expected to increase with the progression of climate change making the impacts even more undesirable. This is particularly well demonstrated in Brazil and the USA where large volumes of water are consumed [1] and significant volumes of corn syrup are used [5]. Elsewhere in the world ethanol for industrial use comes from chemical processes, using sources such as petroleum, natural gas or coal as a source of the carbon. The continuous flow production methods used in chemical reactors can produce huge volumes of ethanol at low costs [6].

1.2.1 Syngas production through gasification

Using natural material as carbon sources, while maintaining the high production rates of synthetic ethanol as well as avoiding compromising food production, would be an ideal direction for the industry [7]. An obvious target has been the use of waste materials as a source, including food waste, waste wood and plant material. Food waste is difficult to transport and auto-degrades into other compounds and thus is often more useful as compostable material [8]. Waste wood and plants are plentiful from the construction, farming and forestry industries, though this varies by geographical area [3]. One of the major problems with making use of plant materials is the difficulty of breaking down cellulose, hemicellulose and lignin which are major components of the plant structure. Many of the natural enzymes and microbes for doing this are slow acting and slow growing respectively. In order to scale the digestion to the kind of volumes that commodity chemical production uses, manufacturers must use some of the largest bioreactors available, around 750,000L [9–11]. While there are projects and significant research under way to make synthetic enzymes and strains for more efficient digestion [12, 13], different feedstocks would require different types of pretreatments to break down bulk material, remove poisoning microorganisms or toxic chemicals [14].

Instead, an alternative process has been developed, used originally for coal where high pressure and temperature steam turns the solid carbon into a mixture of simple gasses known as syngas. Syngas is composed of carbon monoxide (CO), carbon dioxide (CO_2) and hydrogen (H_2) but can also include small chain hydrocarbons such as methane (CH_4) and ethane (C_2H_6) [15–17]. Due to the steam breaking down input materials into simple gasses and ash the conversion is largely indifferent to the input of the raw material. This in turn enables a flexible feedstock of material for the generation of syngas; coal, natural gas, petroleum, green plant material, wood are all viable as carbon sources. This makes syngas conversion ideal as a starting point for a further processing [16–18].

1.2.2 *Clostridium ljungdahlii* and syngas conversion to ethanol

Conversion of syngas to ethanol can be performed by a catalytic process in a flow-bed reactor using $Rh/Mn/SiO_2$ catalysts [19–21]. However these catalytic processes result in non specific hydrocarbons, producing a mixture of methane, methanol and longer chain compounds along with the ethanol, which requires a significant amount of recycling and refining to purify ethanol from the solution [19]. For specificity a biological catalyst is much more efficient and can even be more tolerant to poisoning from unexpected contaminants due to its ability to repair and regenerate without requiring reactor shutdown or cleaning [22]. Multiple organisms show the capacity for the conversion of syngas to ethanol via the Wood-Ljungdahl pathway as shown in Fig1.1, however, IneosBio who sponsored this project make use of a proprietary strain of *Clostridium ljungdahlii* and thus I will introduce that bacteria specifically.

Clostridium ljungdahlii is a gram positive, spore forming, rod shaped bacte-

rium first isolated from chicken yard waste in 1993 [23]. The bacteria was originally isolated for its ability to consume syngas and does so while producing acetate and a small amount of ethanol [23]. Under further study it was discovered that under acidic conditions the bacteria can produce a greater proportion of ethanol, enabling its potential use for industrial ethanol bioproduction [24–26].

In order to produce the ethanol using microorganisms a large volume bioreactor or even multiple bioreactors is necessary to achieve the production rates that are readily achievable by chemical methods. For example a typical petrol production facility can produce 9,000,000 litres of fuel per day [27], of which 5% must be ethanol in the UK. Using a reasonable value for production rates of bacteria, 40 grams of ethanol per litre of bioreactor per day [28] or 50.7mL, the bioreactor volume to match the fuel output must be around 7,000,000L. Given the largest stirred tank bioreactors are around 750,000L at least 10 must be used [11]. The internal design details can vary depending on the expected volume and medium, however the major components are: cooling, stirring, gas feed, water and media feed and beer return. These are optimised on an as needed basis depending on the particular conditions the reactor is expected to operate under [28, 29], however they represent significantly complex pieces of equipment and thus will require an increased maintenance cost compared to a chemical reactor.

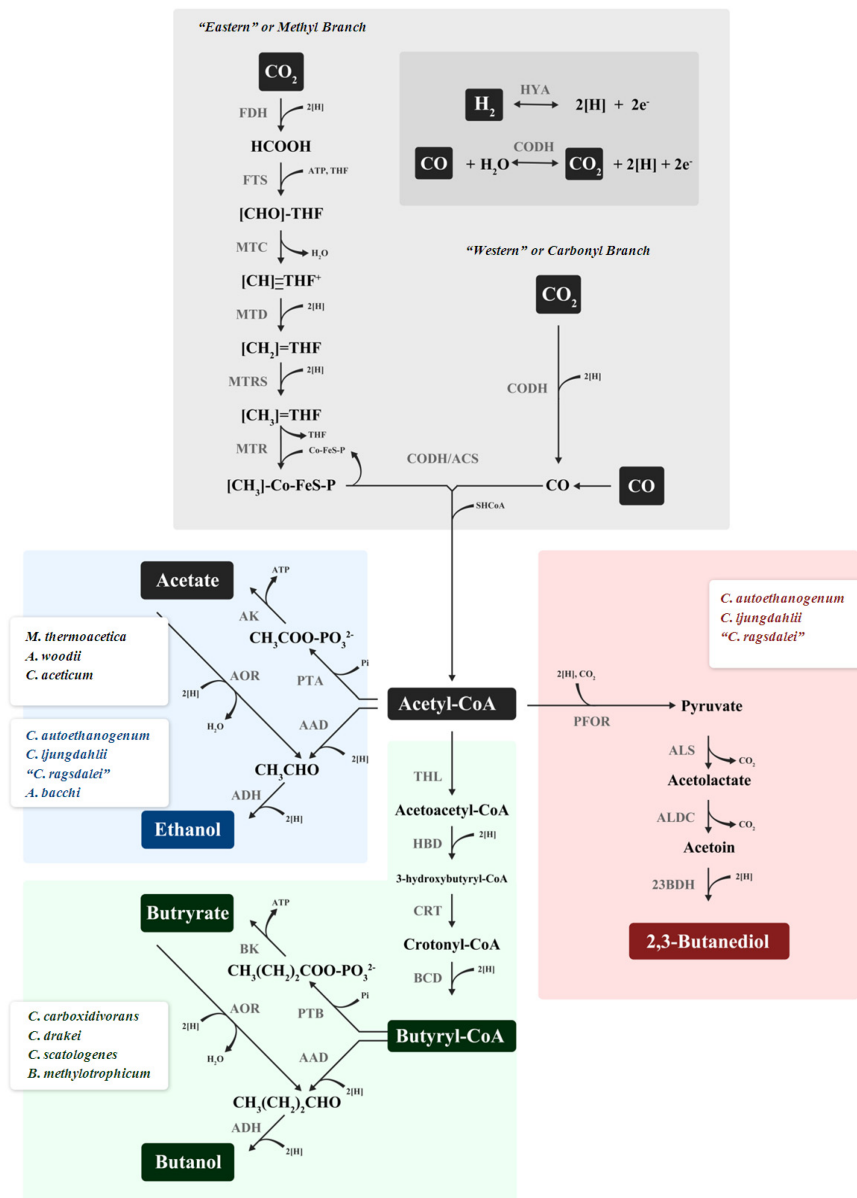


Figure 1.1: Wood-Ljungdahl pathway for the conversion of syngas to various organic solvents by different anaerobic bacteria. Note some bacterial species can perform multiple conversions and chemical pathways are not stoichiometrically balanced. Figure sourced from [22].

Abbreviations: AAD, alcohol/aldehyde dehydrogenase; ACS, acetyl-CoA synthase; ADH, alcohol dehydrogenase; AK, acetate kinase; ALDC, acetolactate decarboxylase; ALS, acetolactate synthase; AOR, aldehyde:ferredoxin oxidoreductase; BCD, butyryl-CoA dehydrogenase; BK, butyrate kinase; CODH, CO dehydrogenase; Co-FeS-P, corrinoid iron-sulphur protein; CRT, crotonase; FDH, formate dehydrogenase; FTS, formyl-THF synthetase; HBD, 3-hydroxybutyryl-CoA dehydrogenase; HYA, hydrogenase; MTC, methenyl-THF cyclohydrolase; MTD, methylene-THF dehydrogenase; MTR, methyltransferase; MTRS, methylene-THF reductase; PFOR, pyruvate:ferredoxin oxidoreductase; PTA, phosphotransacetylase; PTB, phosphotransbutyrylase; THF, tetrahydrofolate; THL, thiolase

1.2.3 Beer distillation is the most expensive part of production

The primary energy consuming component of the bioethanol production process is the distillation of the ethanol from water or cell growth medium in a large tower fermenter. An industrial distillation column is formed of a series of trays with a high temperature at the bottom of the column, normally provided by steam, and a lower temperature near the top allowing for the rising of gaseous products and descent of condensed water as outlined in Fig.1.2 [30–32].

The concentration of the beer has a significant effect on the energy requirements of the distillation column as it determines the number of stages (trays) the column must have to separate the water and ethanol as well as the energy requirements as shown in Fig.4.1 [33]. Due to the chemical properties of a water/ethanol solution, the maximum concentration a distillation column can reach is 95.5% using this process, forming a solution known as an azeotrope where the solvent and solute share boiling points, and must be further processed to produce the pure anhydrous ethanol desired for chemical processes and fuel additives [30–33].

Since changing the concentration of the beer from the bioreactor has a large impact on the energy requirements, this step in the process is the most likely to be affected by any change to the ethanol tolerance of the microorganisms. As such any consideration of the benefits of experiments within this thesis must keep Fig.4.1 in mind, where small changes in beer concentration can have significant energy savings over the physiological range of ethanol tolerances. This is further enhanced by the large volumes of ethanol produced, as even small savings are amplified by the thousands of tons of material produced.

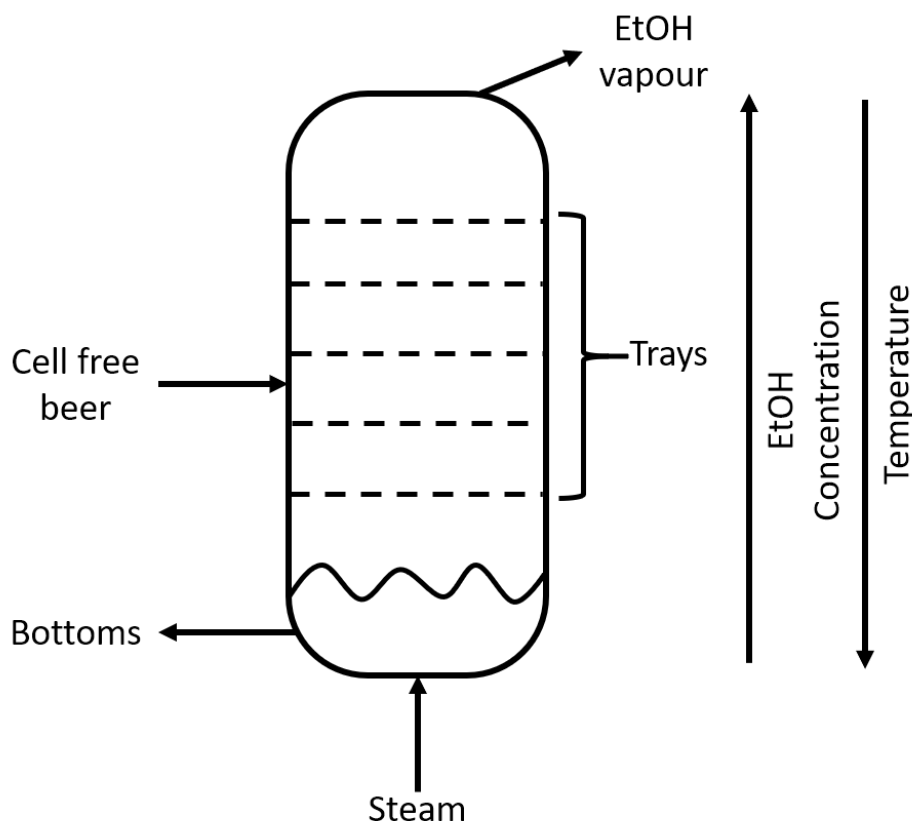


Figure 1.2: Diagram of an ideal distillation column for ethanol. Trays allow for mixing of vapour and liquids as well as increased rate of heat transfer. Bottoms are a low concentration solution of ethanol which is returned to the bioreactor for reuse as distillation at low concentrations has a net negative energy output. Arrows on the right indicate increasing values of ethanol concentration and temperature in the column. [30,31,33]

1.2.4 Azeotrope dehydration is the final step of production

The final stage in the ethanol production process is the dehydration of the azeotrope from the distillation process, which can take the form of further distillation using a third solvent or a salt. Addition of the solvent (usually benzene or cyclohexane) or salt (usually potassium acetate) causes a shift in the boiling point of ethanol relative to water, allowing the distillation to proceed up to 100%. In addition varying the pressure in the distillation column or condenser can further enhance the vapour/liquid equilibrium [33–35].

In non distillative methods, ethanol can be adsorbed by calcium oxide and filtered from solution, or filtered out directly from solution through selective membranes. While these methods do not require as much thermal energy to operate as distillation they can suffer a lower efficiency and throughput.

In either case the method chosen for dehydration of ethanol depends on the existing plant infrastructure and the requirements of the plant itself [35].

This step is independent of the prior process and therefore is unlikely to

change with any alteration to the microbial production step. While still crucial to synthesising the final product, it shall be ignored when considering modifications to the microorganisms suggested in this thesis.

1.3 Osmoregulation in *E.coli*

Osmoregulation is a key process for any type of cell in order to maintain the cell shape [36,37] and appropriate solvent concentrations to keep proteins in their native state and allow for proper intracellular reactions [38,39]. In bacteria and most other walled cells, when grown in an optimal medium, maintain their cytoplasm in a hyperosmotic state relative to the media, thereby creating pressure on the cell wall known as turgor pressure. In *E.coli* this is between 0.1 [40] and 3 atmospheres (303 kPa) [38,41,42]. The *E.coli* osmoregulation system allows adaptation to wide range of osmolarities from 0.015 Osm [43] to 3.0 Osm [44], which is in excess of a 100 fold change in concentrations. This range is achieved by alteration of the concentration of osmolytes, small, soluble and generally unreactive molecules, within the cell so as to adjust cell water content.

1.3.1 *E.coli*'s response to a hyperosmotic shock

When the external osmolarity of the medium is rapidly increased, termed a hyperosmotic shock, the cells rapidly lose water and turgor pressure due to osmosis [46]. Almost immediately cells respond by accumulating osmolytes from the medium, including K^+ ions, glycine betaine, choline and proline, which allows for water and hence volume recovery. Under conditions of low osmolarities the primary osmolytes within the *E.coli* cytoplasm are K^+ ions with a small contribution from Glutamate and with increasing osmolarity of the medium the proportion of osmolytes within the cell increase linearly as expected [39,47]. At higher osmolarities K^+ is still the major osmolyte however other anions such as glutamate and γ -glutamyl accumulate within the cell [48].

The uptake of osmolytes is mediated by a number of proteins that are demonstrated in Fig.1.3, with Kdp, Kup and Trk transporting K^+ ions [49–52]. In addition to K^+ organic osmolytes are accumulated through multiple channels: ProU transporting betaines, ProP transporting proline and BetT transporting choline [42,53,54]. These are accumulated to high concentrations within the cell when they are available in the growth medium [42,53,54]. When these are not present or at very high osmolarity, trehalose, a dimer of glucose, is instead synthesised by the cell [55–57].

Once cells have recovered their volume they resume growing, however, they do so at a reduced rate as shown in Fig. 1.4. It is currently not known why the growth rate is reduced. One previous theory is that a reduced turgor pressure was responsible as without the pressure the cell would be unable to insert new membrane or cell wall precursors [58,59]. Recent experiments have shown that turgor is not necessary for growth of the bacterial cell wall [60,61] and as such the reduced growth rate is still largely a mystery.

With increasing osmolarity, the masses of nucleic acid and protein within the cell remain constant contrasting with the growth rate which both decrease linearly [38,44,46,48]. This is also true of decreasing osmolarity, below the favourable conditions as is shown in Fig.1.4 [38]. Its important to note that although previous research has indicated that cell volume is reduced at high osmolarity, this has not been observed in more modern fluorescent microscopy

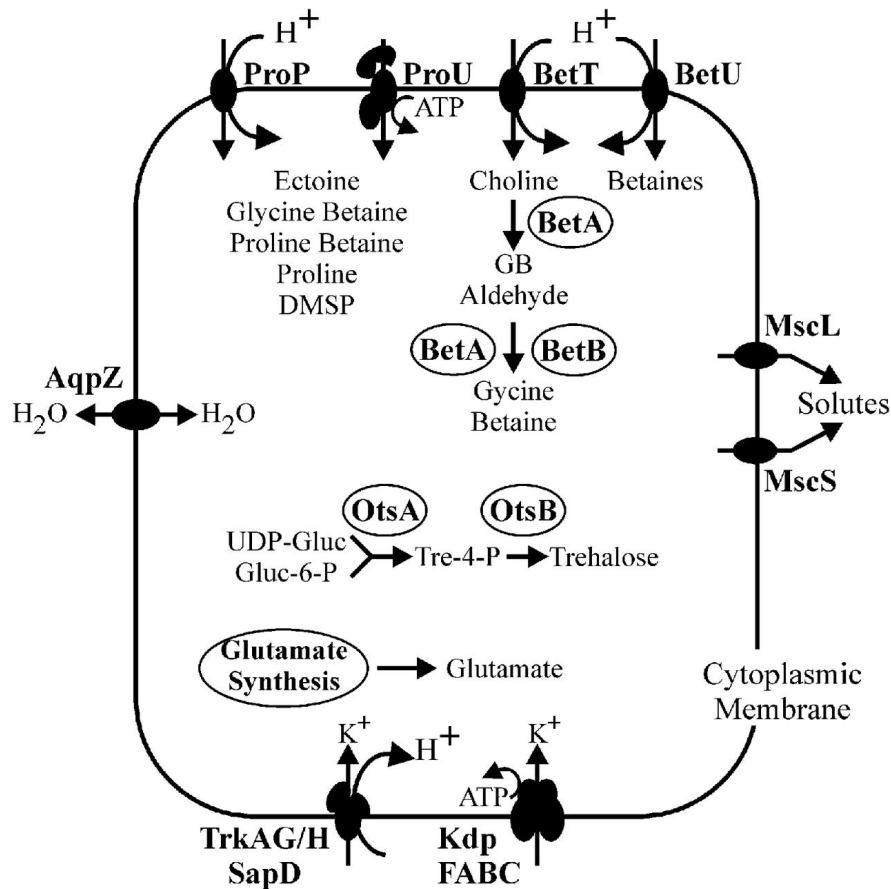


Figure 1.3: Figure and caption obtained from [45]. Osmoregulatory systems of *E. coli*. In high osmotic pressure environments, solutes accumulate in *E. coli* via synthesis (glutamate, trehalose, glycine betaine) or transport from the external medium. K^+ - H^+ symporter Trk and P-type ATPase Kdp mediate K^+ uptake. Major facilitator superfamily member ProP, ABC transporter ProU, and betaine-carnitine-choline family members BetT and BetU mediate organic osmolyte uptake. ProP and ProU are similarly broad in substrate specificity, whereas BetT is choline specific (Murdock et al., 2014) and BetU is betaine specific. Mechanosensitive channels, including MscS and MscL, release solutes from the cytoplasm of osmotically downshocked bacteria. Aquaporin AqpZ exacerbates osmotic stress by accelerating transmembrane water flux. BetT and BetU are homologues of BetP from *C. glutamicum*, whereas ProU is a homologue of OpuA from *L. lactis*

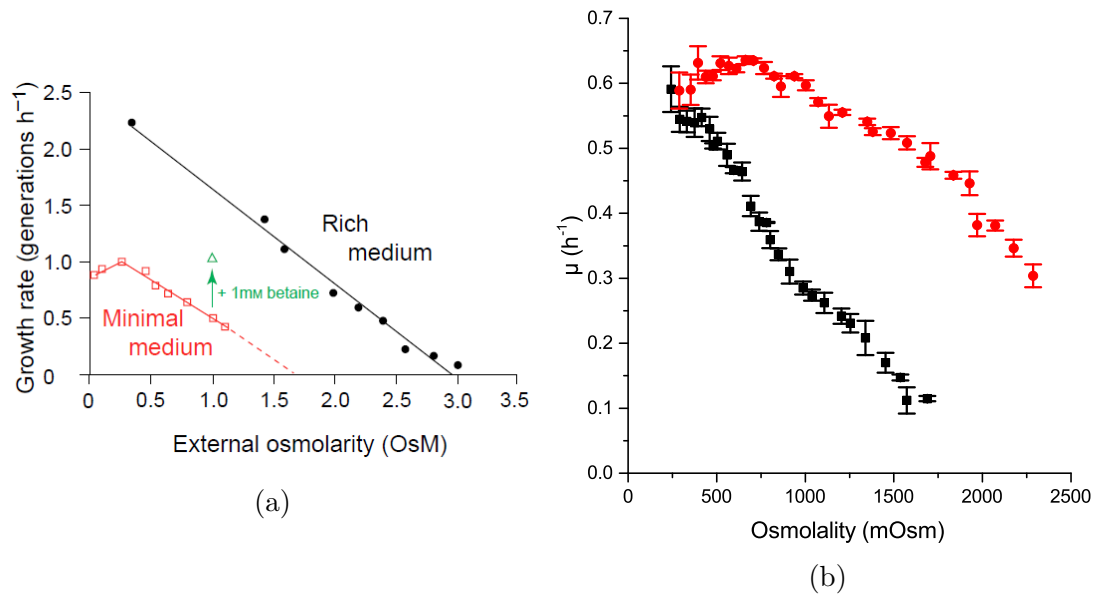


Figure 1.4: (a) Specific growth rate of *E. coli* in media of varying osmolarity (varied by addition of *NaCl*). Minimal medium contained only glucose, buffer and inorganic salts. Rich medium is Luria Bertani broth. Increase on addition of 1mM betaine to minimal medium is also shown. Figure obtained from [44] (b) Specific growth rate of *E. coli* BW25113 in M63 medium with glucose only (black) or supplemented with 20 mmol glycine betaine and choline, osmolarity was increased by the addition of sucrose. Bacteria were grown at 37 °C in a plater reader as described in section methods 2.1.6

experiments [36] where it is shown that the reduction in cell size is an artefact. Previously, complex media was used to grow bacterial cells, such as LB, where size changes occur as a result of many auxic shifts [62] and cells were obtained at a single optical density, often 0.2. As a result of changes to the growth curve cells, at higher osmolarity cells at an OD of 0.2 are in a later stage of growth and thus are smaller but not as a direct result of osmotic effects.

1.3.2 Energy consumption of osmoregulation

Many of the channels and pumps in the cell consume energy in the form of either ATP or protons (H^+ ions), for example the Kdp system consumes ATP to transport K^+ ions [52,63] and the ProP transporter uses protons to transport choline [64], as indicated in figure 1.3. Since ATP and protons drive most of the reactions of the cell, including translation and cell wall synthesis, removal of energy may be causing these contributors to growth to slow down [65]. In addition organic osmolytes have other uses in the cell such as an alternative carbon source for growth or for use in other cell reactions, such as proline being an amino acid used in synthesis of proteins. Of particular note is the osmolyte trehalose which is formed from a dimer of glucose, therefore representing a significant amount of potential energy if used as an energy source. In this case the loss of carbon or other components for use as osmolytes could reduce cell growth rate if the cell

transport systems are saturated [55, 66].

Osmoregulation therefore likely consumes a significant number of resources otherwise used for cell growth and would result in a reduction of the number of cells per unit of media (reduced yield). Therefore in batch culture at the end of growth, when the medium is depleted, we would see this as a lower concentration of cells.

1.3.3 Known physiological changes of proteome allocation and diffusion in *E.coli*

A number of proteins in the osmoregulatory network are upregulated during osmotic challenge [42, 55, 67, 68]. While the numbers of channels vary the up-regulation likely indicates that a significant fraction of the cell proteome is devoted to these proteins and therefore unable to be utilised for growth. This can be in the form of taking the place of enzymes required to metabolise nutrients or taking the place of ribosomes which are required to synthesis all proteins in the cell.

Hwa *et al.* [69] first described and modelled the complex relationship of changes to the relative proportions of ribosomes and other proteins as a function of nutrient quality as demonstrated in Fig.1.5. The linear relationship shown between the growth rate and the ribosome content of the cell (measured by the RNA/protein ratio) is obtained by growing cells on different quality media and therefore nutrient availability. They also generated a simple model to describe this relationship as a function of growth rate:

$$\phi_R = \phi_{R0} + \frac{\lambda}{k_t} \quad (1.1)$$

where ϕ_R is the fraction of protein which are ribosomes, λ is the specific growth rate of the cells, k_t is the inverse slope of the line given in Fig1.5A and ϕ_{R0} is the vertical intercept.

In addition, the model proposed to describe this phenomena defines two other categories of proteins, distributed such that:

$$\phi_P + \phi_Q + \phi_R = 1 \quad (1.2)$$

with ϕ_P representing all proteins needed for the cell to grow on the medium, ϕ_Q representing proteins that do not change concentration in any condition and ϕ_R representing the ribosome fraction. Since the fractions are fixed, any increase in osmoregulatory proteins must replace proteins belonging to the R fraction and therefore will decrease the maximum growth rate as a consequence of the relationship in Eq.1.1.

A further study by Hwa *et al.* in Fig.1.6B shows that the ribosome fraction decreases in a similar manner in both osmolarity and nutrient limitation [70]. However, there is a distinct shift in the gradients between the two types of growth rate reduction, indicating some confounding factors. Hwa *et al.* suggest that translational elongation rate is reduced (Fig.1.6A) by a reduction in diffusion of the precursors (T-RNAs) for protein synthesis but lack direct evidence of these measurements to confirm their hypothesis.

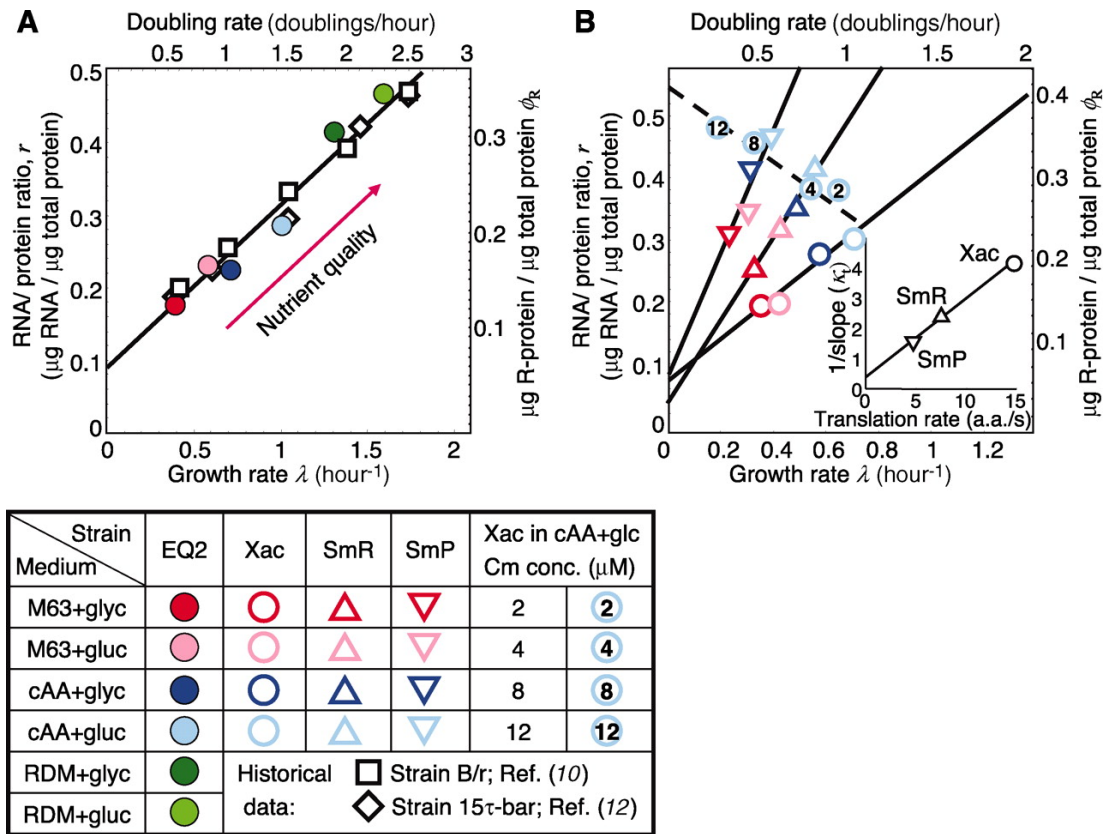


Figure 1.5: Figure and caption obtained from [71]. Correlation of the RNA/protein ratio with specific growth rate λ for various strains of *E. coli*. (A) Comparison among *E. coli* strains grown in minimal medium: Strain B/r [[72], squares], 15 τ -bar [[73], diamonds], and EQ2 ([71], solid circles). The growth rate is modulated by changing the quality of nutrients as indicated in the key at lower left. The fraction of total protein devoted to ribosome-affiliated proteins (ϕ_R) is given by the RNA/protein ratio as $\phi_R = \rho \cdot r$ where r is the measured concentration of RNA and ρ is the conversion factor for RNA to ribosome fraction (see [71] supporting information). (B) The RNA/protein ratio for a family of translational mutants SmR (triangles) and SmP (inverted triangles) and their parent strain Xac (circles) [74], grown with various nutrients (see key at lower left). Translational inhibition of the parent Xac strain via exposure to sublethal doses of chloramphenicol (circled numbers; see legend table) gave RNA/protein ratios similar to those of the mutant strains grown in medium with the same nutrient but without chloramphenicol (light blue symbols). Inset: Linear correlation of k_t values obtained for the Xac, SmR, and SmP strains with the measured translation rate of the respective strains [75] ($r^2 = 0.99$).

A decrease in diffusion constant has been suggested previously based on the fact that that accumulation of the large numbers of osmolytes in the cytoplasm may crowd molecules, particularly large ones such as ribosomes, and therefore reduce the reaction rates by limiting their diffusion [76,77]. Diffusion of particles within the cytoplasm has been measured both in varying conditions and at high osmolarities. This is often done during an osmotic shock where cell volume and

Measurement	Diffusion constant ($\mu\text{m}^2\text{s}^{-1}$)	Method	Source
Venus YFP	8(+4 – 2)	Single molecule tracking	[78]
GFP	6.1(\pm 2.4)	FRAP	[79]
GFP	7.7(\pm 2.5)	FRAP	[80]
Polysomes	0.04	Single molecule tracking	[81]
NDB glucose	50	extrapolation‡	[76]
beta-galactosidase-GFP	0.8		
50MDa ribosome+mRNA	0.02		
TorA-GFP2†	8.3	FRAP	[82]
TorA-GFP3†	6.3 \pm 2.6		
TorA-GFP4†	5.5 \pm 1.9		
TorA-GFP5†	2.8 \pm 1.5		
AmiA-GFP†	1.8 \pm 0.8		

Table 1.1: Diffusion constants for various proteins or chemicals in *E.coli* cytoplasm. YFP and GFP are fluorescent proteins, TorA:trimethylamine N-oxide reductase, AmiA:periplasmic amidase †Protein tagged with GFP multimers. Cells were grown with Cephalixin to produce elongated cells. ‡calculated based on extrapolating from measurements

water content is changed with fewer studies done after the cells have properly adapted to the growth medium.

The two methods used to measure diffusion in the cytoplasm are FRAP measurements or single particle tracking and are normally performed using fluorescently tagged proteins within the cytoplasm. Tagging proteins in this manner however, can lead to effects from binding of the protein to other complexes, itself, or even interference from the fluorescent tag (often GFP). As a result its often difficult to compare different measurements and experiments reliably and since many labs are only interested in a particular target protein do not consider a coherent model of changes to the diffusion within the cytoplasm.

Some examples of relevant diffusion constants are listed in Table.1.1 along with their methods of measurement. Its important to note that different diffusion constants have been measured for the same protein and few measurements have been made for larger complexes or proteins.

Despite these difficulties measurements have been made of changes to diffusion as a result of osmolarity, particularly by Poolman *et al.* who show decreasing cytoplasmic diffusion at increasing osmolarity by using three fluorescent probes of different sizes. These probes are a fluorescent glucose analogue, GFP and a GFP- β -galactosidase fusion [77]. A follow up study on cytoplasmic crowding [83] using a FRET based crowding reporter shows, paradoxically, that crowding actually decreases with increasing osmolarity in recovered cells. It is unclear why the diffusion would decrease while the crowding decreases, however the authors suggest that it may be due to the difference in size between the FRET sensor and other molecules in the cytoplasm, particularly the much larger ribosome complexes formed with with RNA during translation.

In order to integrate both diffusion and ribosome fractioning I intend to measure both within our strain to hopefully attain a consistent picture of changes at high osmolarity. Its also important to try to minimise the unforeseen effects from protein interactions and size differences.

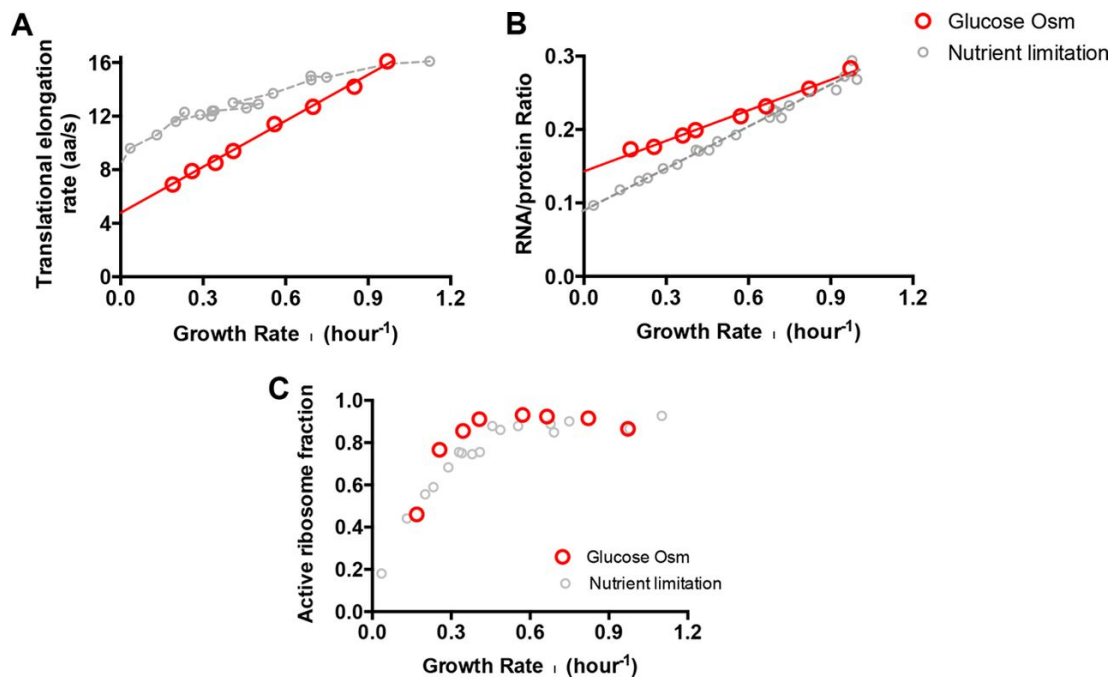


Figure 1.6: Figure and caption obtained from [70] with my notes in *italics*. Comparison of translation parameters under hyperosmotic stress *grown in MOPS minimal medium with glucose* and under nutrient limitation. (A) Translational elongation rate. (B) Ribosome content. (C) Fraction of ribosomes actively translating. The data points under nutrient limitation are replotted from data in the article by Dai et al. [84].

1.4 Osmoregulation and ethanol resistance

1.4.1 Membrane based damage and protection

As with other osmotic stressors, ethanol has a number of effects on a bacterial cell due it being freely permeable across cell membranes; it affects both the cell interior and exterior. But, unlike osmotic stressors, the ethanol acts by inserting itself into the membrane, causing increased fluidity with increasing concentrations of ethanol [85] and indicated by bending of vesicles in Fig.1.7, which ultimately leads to a decrease in the cells ability to hold onto usually non permeable molecules such as nucleotides or charged ions [86]. Cells respond to this fluidity, both in solvent tolerant and intollerant strains by increasing their membrane stiffness through the increased concentration of longer chain membrane lipids and protein content [85, 87–89].

A similar process has been shown to occur in response to an increase in osmolarity, which has been suggested as a necessary response to changes in cell turgor pressure. This response operates through the production of molecules

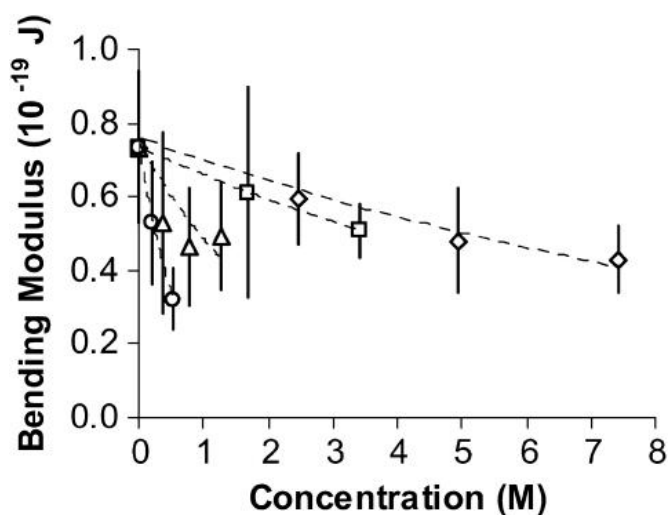


Figure 1.7: Figure and caption from [95] with my comments in italics. Average bending modulus of vesicle membranes *a value proportional to membrane stiffness*. k_c , values of SOPC vesicles in alcohol/water mixtures: methanol (diamonds), ethanol (squares), propanol (triangles), and butanol (circles). Bars indicate 1 SD. Differences between control and alcohol-exposed vesicles were statistically significant ($P < 0.05$) as evaluated by Student's t-test ($\alpha = 0.05$) except for values at 1.70 M of ethanol and 0.39 M of propanol.

such as ubiquinone [90] which insert into the membrane and act to increase its stiffness, as well as the production of large numbers of osmotransporting channels [42, 53, 91–94].

1.4.2 Protein unfolding and protection by osmolytes

Since ethanol can form strong hydrogen bonds of its own it will compete with water for protein hydration and therefore alter the stability of protein folding, binding and the formation of other complexes [96–98]. During an osmotic shock, a similar process occurs in response to changes in osmolarity, the water content of cell is significantly altered leading to instabilities in proteins due to the changes in hydration state [99, 100]. These small changes can significantly alter the effectiveness of enzymes, for example many purified enzymes used as tools in the lab require specific buffers to maintain their maximum activity. Alterations are theorised to be compensated for by the nature of the osmolytes accumulated, with molecules such as glycine betaine and trehalose being shown to have protective effects with temperature [99, 101, 102] and osmolarity [103–106].

1.4.3 Using osmoregulation for in ethanol resistance

Given the overlaps in protein unfolding, changes to the membrane fluidity and protective effects of osmolytes demonstrated with both ethanol and high osmolarity, it may be useful to try and utilise the osmoregulatory network to help improve ethanol resistance. This could take the form of adapting cells to high osmolarity before exposure to ethanol, adding osmolytes to the medium or

overexpression of osmoregulatory genes. Since the network is better studied in *E.coli* than *C. ljungdahlii* it makes sense to start my work in *E.coli* and improving its ethanol resistance before moving to the IneosBio industrial strain of *C. ljungdahlii*.

Chapter 2

Methods

2.1 Strains and media

2.1.1 Bacterial strains

All experiments were performed, except where mentioned, with *E. coli* strain BW25113 (F^- , $\Delta(\textit{araD} - \textit{araB})567$, $\Delta\textit{lacZ}4787::\textit{rrnB-3}$, λ^- , *rph-1*, $\Delta(\textit{rhaD} - \textit{rhaB})568$, *textit{thsdR}514*), a close relative of MG1655, and the parent strain of the Keio collection [107]. For the optical density calibration measurements the plasmid pWR20, which expresses and enhanced GFP for cytoplasmic volume monitoring, was introduced [108].

For ethanol tolerance testing Keio collection mutants were used [107]. The Keio collection is a library of all non essential single gene knockouts where the target gene is replaced with a kanamycin resistance cassette.

In order to perform cytoplasmic diffusion measurements a strain of BW25113 was prepared that expressed GFP- μ NS protein under control of the Lac operon. This strain was derived from CJW4617, [109] who constructed the original expression vector and integrated it into MG1655, using P1 transduction as described below.

To prepare frozen stocks of all bacterial strains were grown overnight in whatever media an experiment required, diluted 10^4 in fresh media and allowed to grow to an OD of 0.2. Cells were mixed with 50% glycerol in a 3:2 ratio before being frozen in liquid nitrogen in aliquots of 200 μ l.

2.1.2 P1 transduction for construction of BW25113-GFP- μ NS

The following protocol was used for the transduction of the GFP- μ NS cassette from the original CJW4617 (MG1655 *lacZYA::GFP- μ NS*) to BW25113. Protocol is derived with minor modifications from [110]. To move the cassette into a P1 lysate:

1. Inoculate a single colony of the donor strain in 5 ml LB medium and shake at 37°C overnight.
2. Inoculate 0.05 ml of the overnight culture in 5 ml ml of LB medium contain-

ning 0.2% glucose and 5 mM $CaCl_2$.

3. Incubate for 30 minutes at 37 °C with aeration.
4. Add 0.1 ml of a P1vir lysate (5×10^8 phage/ml).
5. Shake or rotate at 37 °C for 2-3 hours until the cell lyse.
6. Centrifuge at 4500g for 10 minutes to pellet the debris.
7. Supernatant was then passed through a 0.22 μ m syringe filter
8. Carefully transfer the supernatant to a sterile, screw-capped tube. Add 0.1 ml of chloroform and vortex to mix. Store the lysate at 4 °C.

To introduce the GFP- μ NS cassette into the recipient strain by transduction, I followed the following protocol:

1. Inoculate a single colony of the recipient strain in 5 ml LB medium and shake at 37 °C overnight.
2. Centrifuge the overnight culture at 1500g for 10 minutes and resuspend the cell pellet in 2.5 ml of 10 mM $MgSO_4$ containing 5 mM $CaCl_2$.
3. To 0.1 ml of resuspend cells in tubes, add variable amount of P1 lysate, usually from 10 μ l to 1 ml. Also prepare a tube of just the P1 lysate as a negative control.
4. Incubate the tubes for 30 minutes at 30 °C without shaking.
5. Add 1 ml of LB with 10 mM sodium citrate.
6. Incubate 30 minutes at 37 °C without shaking.
7. Centrifuge 1500g for 10 minutes to pellet. Discard the supernatant.
8. Add 1 ml of 1 M sodium citrate.
9. Plate onto selective medium. For introducing the GFP- μ NS cassette from the Keio Collection, use 50 g ml⁻¹ kanamycin.

Successful transduction was confirmed by taking colonies from the selective plate and growing them in the manner described in section 2.2 and confirming particle expression.

2.1.3 Media

LB

Ingredient	Mass for 1 litre (g)
Yeast extract	5
Tryptone	10
NaCl	10

Modified M9 (MM9) [108, 111, 112]

Ingredient	Final concentration (mM)
Na_2HPO_4	50
NaH_2PO_4	25
$NaCl$	10.7
NH_4Cl	23.4
$MgSO_4$	1mM
$CaCl_2$	0.1mM
KCl	1mM
Glucose	0.3%
EAA Sigma MEM amino acids 50x	1x

M63

Ingredient	Final concentration (mM)
KH_2PO_4	100
$FeSO_4 \cdot 7H_2O$	1.8
$(NH_4)_2SO_4$	20
Thiamine	0.0001
$MgSO_4$ (1M)	2
cAA (20%)	20
Carbon source (20%)	0.5%w/v

The carbon source is either glucose or glycerol, and the cas-amino acids(cAA) are optional, generating four variants of the medium; m63-glu, m63-gly, m63-glu-cAA, m63-gly-cAA.

RDM: Rich Defined Media

This medium is based off the recipe of Neidhardt *et al* [113] and used in Scott *et al* 2010 [71]. This is designed as an optimal growth medium for *E.coli* with as many nutrients as possible.

RDM component	Final concentration (mM)
Tricine (MW 179.2)	4.0
Iron Sulfate	0.01
Ammonium Chloride	9.5
Potassium Sulfate	0.276
Calcium Chloride	0.5×10^{-3}
Magnesium Chloride	0.525
Sodium Chloride	50
Ammonium Molybdate	2.92×10^{-7}
Boric Acid	4.00×10^{-5}
Cobalt Chloride	3.02×10^{-6}
Cupric Sulfate	3.02×10^{-6}
Manganese Chloride	8.08×10^{-6}
Zinc Sulfate	9.74×10^{-7}
Potassium Phosphate Dibasic Anhydrous	1.32
Potassium Hydroxide	1.5
Adenine	0.199
Cytosine	0.199
Uracil	0.199
Guanine	0.199
L-Alanine	0.8
L-Arginine HCl	5.2
L-Asparagine	0.4
L-Aspartic Acid, Potassium Salt	0.4
L-Glutamic Acid, Potassium Salt	0.6
L-Glutamine	0.6
L-Glycine	0.8
L-Histidine HCl H_2O	0.2
L-Isoleucine	0.4
L-Proline	0.4
L-Serine	10
L-Threonine	0.4
L-Tryptophan	0.1
L-Valine	0.6
L-Leucine	0.8
L-Lysine HCl	0.4
L-Methionine	0.2
L-Phenylalanine	0.4
L-Cysteine HCl	0.1
L-Tyrosine	0.2
Thiamine HCl	0.01
Calcium Pantothenate	0.01
para-Amino Benzoic Acid	0.01
para-Hydroxy Benzoic Acid	0.01
2,3-diHydroxy Benzoic Acid	0.01
Glucose	0.20%

All media is filter sterilised through a 0.22 μm syringe filter (Millipore, United States) to ensure no bacterial or fungal contamination.

2.1.4 Preparation of medium osmolarities

To prepare media of increased osmolality, 4x concentrated stocks of the above media were prepared. To compensate for the non linear osmolality of sucrose high osmolality solutions were prepared as follows. A high osmolality stock of 1.85 M solution of sucrose was prepared, and mixed with 4x medium and water in the following ratios:

Desired osmolality (added mOsm/kg)	4x medium	1.85M sucrose	H2O
0	2.5	0	7.5
400	2.5	1.6	5.9
600	2.5	2.4	5.1
800	2.5	3.2	4.3
1000	2.5	4	3.5

For *NaCl* a 3 M solution was prepared and mixed in the following ratios:

Desired osmolality (added mOsm/kg)	4x medium	3M <i>NaCl</i>	H2O
0	2.5	0	7.5
400	2.5	0.07	7.43
600	2.5	0.10	7.40
800	2.5	0.13	7.37
1000	2.5	0.17	7.33

Note molarity is half for these solutions due to the dissociation of *NaCl* allowing it to contribute twice as much as sucrose to osmotic increase.

Obtained osmolalities were measured using a freezing point depression osmometer (Camlab, United Kingdom).

2.1.5 Cell growth

Cells were inoculated from frozen stocks at a 10^4 dilution into 20 ml of fresh medium dependent on the experiment being performed. Cultures were shaken in a 100 ml flask at 37 °C while being shaken at 200rpm in an orbital shaker. Optical densities were measured using 1 ml plastic cuvettes in a Shimadzu UV-1280 spectrophotometer (Shimadzu, Japan). When optical densities were above 0.6 cultures were diluted 1 in 10 to ensure that they were within the linear range of the spectrometer.

2.1.6 Cell growth in platereader

OD measurements of bacterial cultures were performed in a Spectrostar Omega microplate reader (BMG, Germany) with a Costar Flat Bottom 96-well plate with lid (Corning, United States) 300 μ l per well. Absorbance was measured at wavelength 600 nm and temperature 37°C and the mean of 5 readings taken. All measurements were reported using the BMG with correction values, which is given as the measured OD multiplied by 1.0560 for 300 μ l well volume.

2.1.7 Growth rate analysis

All growth rates quoted in this thesis are given as specific growth rate (μ) analysed using the software developed by Swain *et al* [114]. Hyperparameters were manually tuned to the individual experiment however all data in a given graph or section were analysed using the same parameters to ensure a consistent report of growth rate and error.

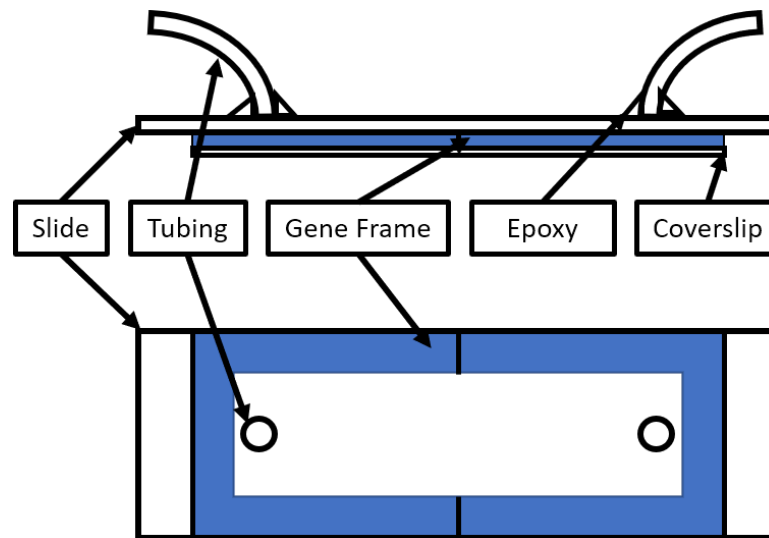


Figure 2.1: Diagram of microfluidic slide constructed by drilling through a glass slide, inserting microtubing which is sealed with epoxy resin and then creating a channel using two geneframes and a large cover slip.

2.2 Single particle diffusion microscopy

2.2.1 Induction of particle expression

E.coli BW25113-GFP- μ NS was grown in M63-Glu-cAA or with the addition of 1000mOsm of NaCl or Sucrose to an OD of 0.1 at 37°C. This was then induced with 10, 50 or 200 ng ml⁻¹ IPTG for 20 minutes to induce expression of the GFP- μ NS protein.

2.2.2 Microfluidic slide preparation

For experiments requiring long imaging of a single slide and, thus, constant supply of nutrients and oxygen, flow-cells were manufactured by drilling two 1.8 mm holes on opposite ends of the microscope slide and attaching Tygon R Microbore tubing (SaintGobain Performance Plastics, France). The flow-cell was then created by attaching the geneframe (Fisher Scientific Ltd, USA) to the slide and covering it with a cover glass as shown in Fig2.1. Slides were coated with 1% poly-L-lysine (PLL) by flushing PLL through the flow-cell/tunnel-slide for ~10s followed by washing it out with the excessive volume of growth medium. Cells were then loaded into the flow-cell and incubated for 10 min at 37°C to allow attachment. Unbound cells were washed out with the growth medium. Attachment via PLL has been shown to not affect cell growth [115]. Fresh medium was passed through the flow cell at 50 μ l/ min using a Fusion 400 syringe pump (Chemyx, United States) and 10mL syringe (BD plastics, USA) for up to 40 minutes, the maximum length of experiment.

2.2.3 Cell imaging for diffusion

Cells were observed in epifluorescence using a Nikon Eclipse Ti microscope with perfect focus at 37 °C. At the beginning of each recording cells that expressed GFP- μ NS and were flat with respect to the focal plane were identified in the field of view by taking a single frame in brightfield and then in fluorescence using methodology described in [46, 116]. Exposure time of both frames was 0.01 ms, with maximum camera gain and images were captured using a 512 x 512 pixel back-thinned electron-multiplying charge-coupled device camera (Andor Technologies, Northern Ireland). Once a cell containing a particle has been identified the camera field of view is narrowed to surround only the cell and data acquisition performed using streaming mode at 0.01 ms exposure. Illumination was provided using a 488nm laser (33mW power at the back focal plane of the objective) using low angle illumination mode using a Plan Apo lambda 100x TIRF objective (Nikon, Japan).

2.3 Optical Density calibration

Brightfield Microscopy for optical density calibration

Samples for microscopy were prepared by placing a sample of medium and cells in a microscope tunnel slide [108]. Imaging of samples was performed using a custom-built brightfield microscope consisting of a CFI Plan Apochromat Lambda 100x objective (Nikon, Japan) with the sample mounted on a Nano-Z piezoelectric stage (Mad City Labs, United States). Illumination of the sample was provided by a white LED (Luxeon Star, Canada) and images recorded on an iXon Ultra 888 EMCCD camera (Andor, Northern Ireland). Stacks of images through each sample were acquired every 0.05 s and separations of 0.5 μ m, ensuring all scatterers in the volume were identified without introducing overcounting. True values of C were experimentally determined by counting N present in the known stack volume determined by the field of view of the microscope ($55.6 \times 55.6 \times 100 \mu$ m). For each osmolarity, C was determined by counting N using brightfield microscopy as above.

2.4 Ribosome and protein content measurements

Bacterial culture protein concentration measurements

Protein measurements were performed using a Lowry assay with Petersons modification [117] using a Total Protein Quantification Kit (Sigma-Aldrich). Cells were grown as described above, section 2.1.5, to an OD between 0.2 and 0.4 and a 500 μ l taken, 500 μ l water added and then the cells were fixed with the application of 100 μ l DOC. Each tube had 100 μ l of 72% trichloroacetic acid solution added, was thoroughly vortexed and then centrifuged at 8000g for 10 minutes to pellet the protein precipitate. The supernatant was decanted and discarded, leaving a dry pellet. This precipitation step, the Peterson modification, allows for removal of lipids or metabolites that may alter the reading of the assay.

For the protein measurement, the pellet was resuspended in 400 μ l Lowry reagent and 400 μ l of water then allowed to stand at room temperature for 20

minutes. Finally 200 μl of Folin solution was added, allowed to stand for 10 minutes before being centrifuged for 10 minutes at 8000g. The supernatant was measured at 750 nm.

To convert the absorbance reading to protein concentration a standard curve was prepared using bovine serum albumin provided as part of the Sigma-kit and analysed using the same protocol as above.

Bacterial culture ribosome concentration measurements

Technique was adapted from [118] was modified for small volumes by Matt Scott (University of Waterloo, Canada) who supplied the completed protocol to us. Cells were grown as described above to an OD between 0.2 and 0.4 and a 1.5 ml taken and centrifuged for 1 minute at 8000g to precipitate the cells. Cells were then washed twice using 600 μl of 0.7M perchloric acid $HClO_4$ (PCA), centrifuged at 8000g for 3 minutes and the supernatant discarded. Once washed the cells have been lysed, then the RNA is hydrolysed by suspending the cells in 300 μl of 0.3M potassium hydroxide (KOH) for 60 minutes at 37°C. 100 μl of 3M PCA was added to the extracts, vortexed and centrifuged at 8000g for 3 minutes before the RNA containing supernatant is transferred to a collection tube. The remaining pellet is washed twice with 550 μl which is also collected in the collection tube, ensuring the extraction of all RNA from the sample. Finally, the collection tubes are centrifuged at 8000g for 10 minutes to remove any remaining cell debris from the supernatant before it is measured at 260 nm in a UV transparent cuvette.

The final RNA concentration is determined by equation 2.1, where the RNA is normalised against the optical density of the original culture at sampling time.

$$RNA\left(\frac{\mu\text{g}}{\text{mL} \cdot OD_{600}}\right) = \frac{31 \cdot OD_{260}}{OD_{600}} \quad (2.1)$$

2.5 Ethanol tolerance measurements

1.5 μl frozen stocks of BW25113 and Keio collection mutants was added to 15ml of the test medium and thoroughly vortexed to ensure even mixing. 200 μl of this master solution was added to each well of a with a Costar Flat Bottom 96-well plate with lid (Corning). Sample tray was moved to a 4°C room where 50 μl of a water/ethanol solution was added to each well to produce the final concentration of ethanol. The low temperature prevents evaporation of the ethanol becoming a factor in changing the concentrations. Plates were finally sealed using an optically clear PCR plate seal (BIORAD Microseal 'C' Film) before being placed in a platereader. OD measurements of the bacterial cultures were performed in a Spectrostar Omega microplate reader (BMG, Germany). Absorbance was measured at a wavelength of 600 nm and temperature 37°C and the mean of 5 readings taken. Once growth curves had been completed, the plate was moved into a 37°C for a further two days without a lid covering the seal. Plate wells were checked by eye for a reduction in volume indicating a failure of the seal and evaporation of the ethanol and growth medium, as such these wells were removed from analysis.

Growth of cells was determined as an increase in optical density over an OD of 0.2 during the two day growth period.

Chapter 3

Developed methods

3.1 Single particle diffusion measurement

Useful definitions

Term	Definition
MSD	mean squared displacement
r_g	radius of gyration
Recording	a video of a single cell with a single particle
Frame	a single frame of a recording
Track	a table of x, y coordinates of a particle motion through sequential frames
t	time from start of a video section
D	real diffusion constant
τ	time step for simulation
D_{obs}	diffusion constant observed from MSD

Motivation

Before I would start measuring diffusion within living cells it was important to understand the necessary parameters for the experiments. Specifically, I wanted to know how many cells I would need for each particle size in a condition to properly determine the diffusion constant as well as the influence of imaging parameters upon the experiment. As well it would be preferable to have an independent verification of the analysis techniques used. As such I set out to design a simple computer simulation of single particle diffusion in order to explore the limits without the difficulties of a practical experiment.

3.1.1 Constructing of a computer simulation of ideal particles

Each particle starts with coordinates at $[0, 0]$ at frame 0 and time 0. Every time step the increment (k) is calculated as follows.

$$k = a\sqrt{\tau \cdot d \cdot D_{in}} \quad (3.1)$$

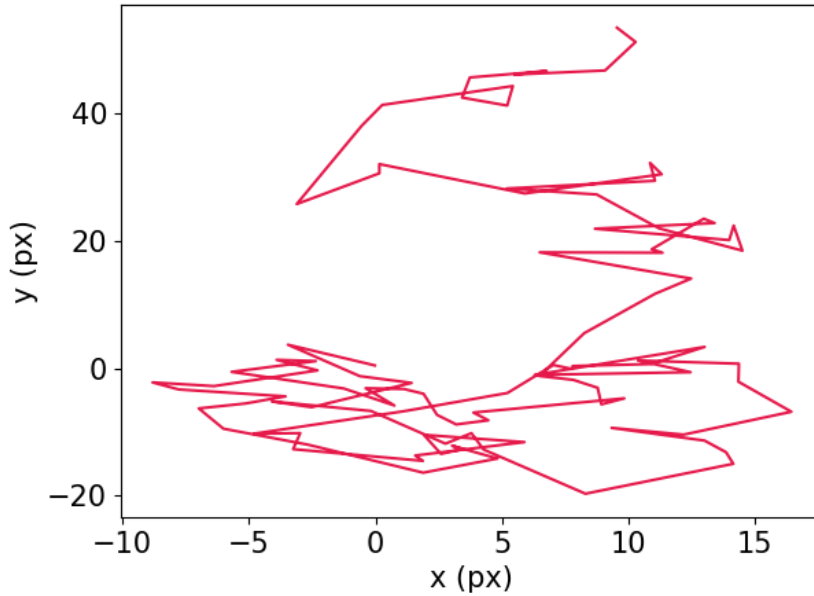


Figure 3.1: Track of a single simulated particle with $D_{in} = 500$

Where a is a number generated from a normal distribution of mean 0 and variance 1, τ is the time step, d is the number of dimensions and D is the diffusion constant [119]. K is generated once for each dimension at every time point and added to the coordinates as in eq:3.2 to 3.4.

$$t_0 = [0, 0] \quad (3.2)$$

$$t_1 = [0 + k_1, 0 + k_2] \quad (3.3)$$

$$t_2 = [0 + k_1 + k_3, 0 + k_2 + k_4] \quad (3.4)$$

Tracks can be generated for any length or diffusion constant an example trace is shown in Fig.3.1.

When the particles are free to diffuse to infinity the MSD of particles tends to increase linearly with time as in Fig.3.2a. However in a bacterial cell any particle will be confined to its interior and therefore cannot diffuse to infinity and as such will limit the maximum displacement. In order to include this in the simulation we created a simple bounded cell represented by a rectangle with length 3 and width 1 with centre of mass at $[0,0]$. The bounds are flat, such that when $x_t > x_{lim}$, $x_t = x_{lim}$, and the simulation parameters are such that an x length of 1 is equal to $1 \mu\text{m}$.

3.1.2 Calculating diffusion constant from using mean squared displacement

For every track the MSD for each lag time t_l is calculated as in eq5.

$$MSD(t_l) = \frac{1}{N} \sum_{t=0}^{lim} (x(t_l + t) - x(t))^2 + (y(t_l + t) - y(t))^2 \quad (3.5)$$

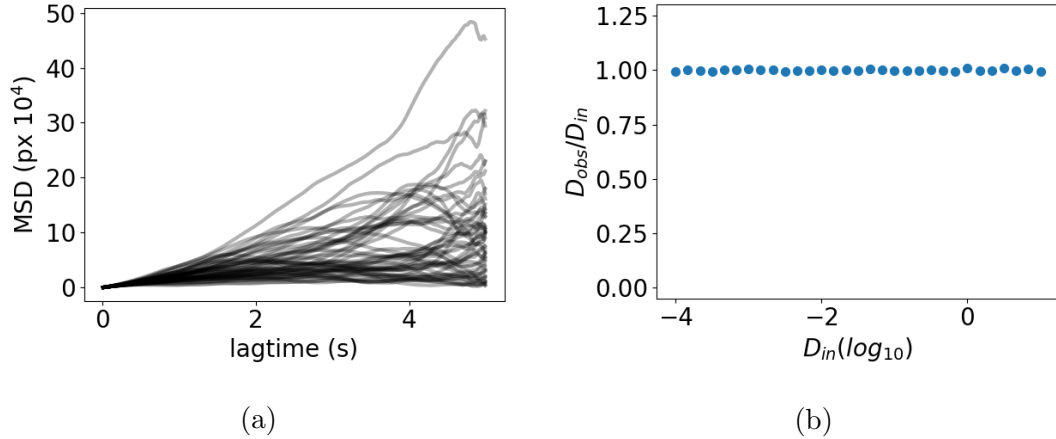


Figure 3.2: a) Mean squared displacement for 100 simulated particles of $D_{in} = 500$ and total simulation time of 500 steps. b) Input/observed diffusions for various input D s given no bounds on particle motion. Sample size used was 1000 particles per input diffusion constant, simulated for 500 timesteps at 0.01s resolution, with max lagtime of 50 timesteps. Observed diffusion constant shows very close value to input diffusion, small deviations are a result of statistical noise.

where x is the x coordinate of a single particle at a given time. The graph of MSD vs t_l is plotted and a straight line fitted $y = mx + c$ where the diffusion constant $D_{obs} = m/4$

3.1.3 Confirmation of simulation predictive capacity

In order to confirm that the simulation produced a real diffusive model, I simulated a large number of particles with a fixed diffusion constant D_{in} . I then used the MSD calculation as described above to produce a D_{obs} which could be compared with the input to see if the simulation was accurate. The results of one of the experiments is show in Fig. 3.2b. As expected I see close association of the D_{obs} and D_{in} with some variance which is likely a result of statistical noise. This is normally corrected in practical experiments by processing all tracks of a given sample as a single dataset and fitting against that, however such methodology is not possible in the practical experiments due to the variations in particle size and thus noise must be dealt with in another manner.

3.1.4 Estimating the sample size required

Since noise is expected due to the random nature of diffusion, I must determine a reasonable sample size for our experiments under ideal conditions. To do this I simulated varying numbers of theoretical particles using a single diffusion value in the mid range of quoted values for the bacterial cytoplasm such that $D_{in} = 0.1$. In Fig.3.3 we see that the noise between replicates decreases as the particle number increases, however the noise is maintained up to 500 particles. Since this represents the noise of each bin for a given particle size selecting a large number would require significant data collection. As a compromise I chose to obtain bin

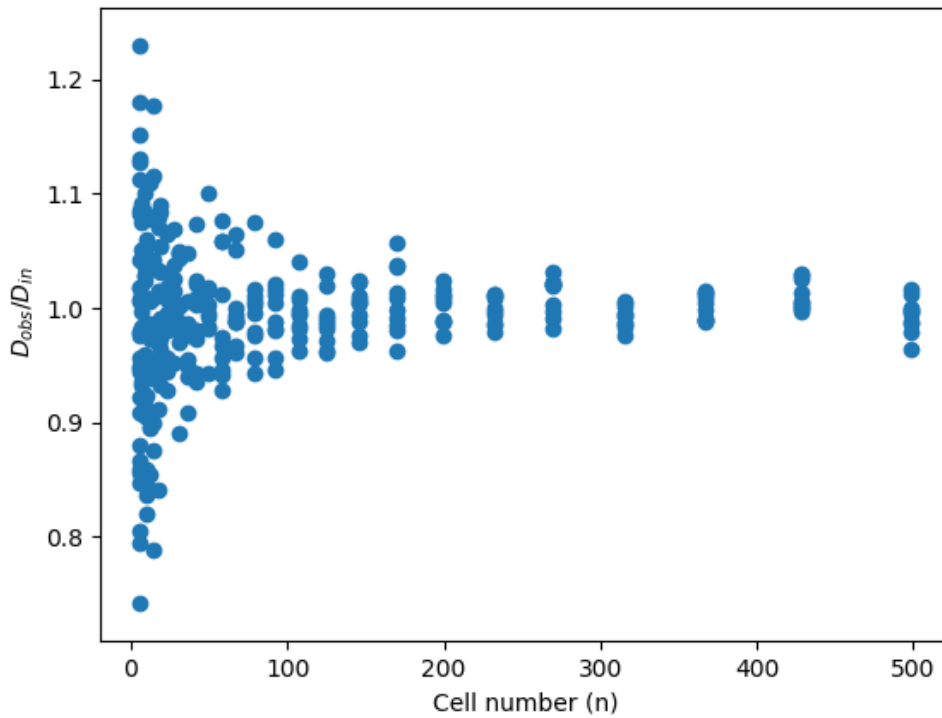


Figure 3.3: D_{obs}/D_{in} diffusions for various particle numbers. Each point represents the average D_{obs} for the number of particles on the x axis. For each particle number, 10 independent experimental replicates were performed to obtain an idea of noise generated by the sampling. For every simulation $D_{in} = 0.1$ with no bounds, simulated for 500 timesteps at 0.01s resolution, with max lagtime of 50 timesteps.

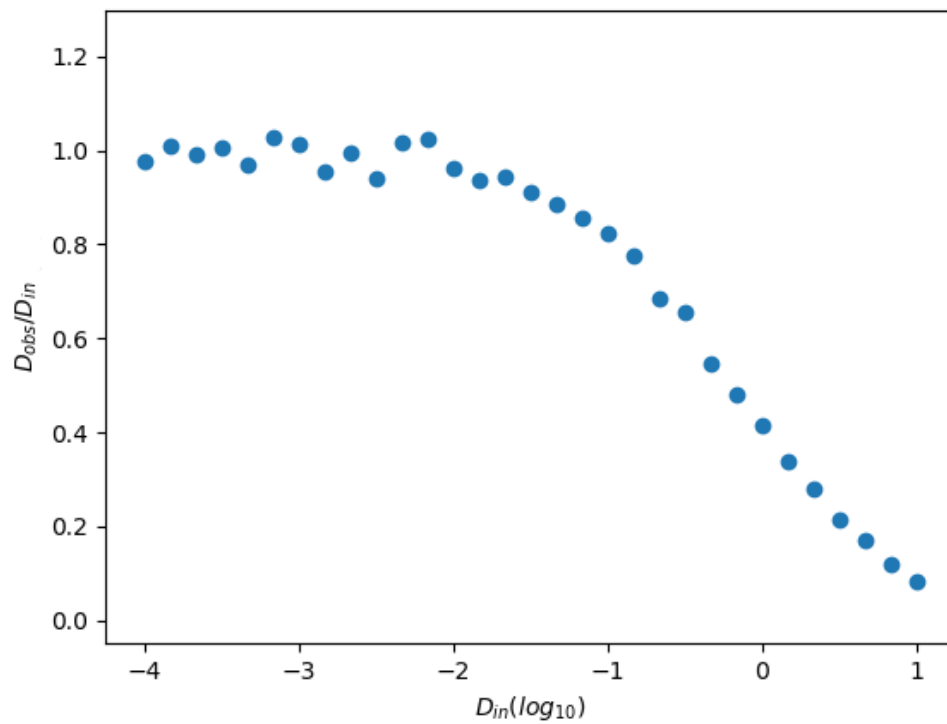


Figure 3.4: D_{obs}/D_{in} of diffusions for particles confined to cells of dimensions given above. Each point represents the average D_{obs} for 100 simulated particles. Each particle is simulated for 500 timesteps at 0.01s resolution, with max lagtime of 50 timesteps.

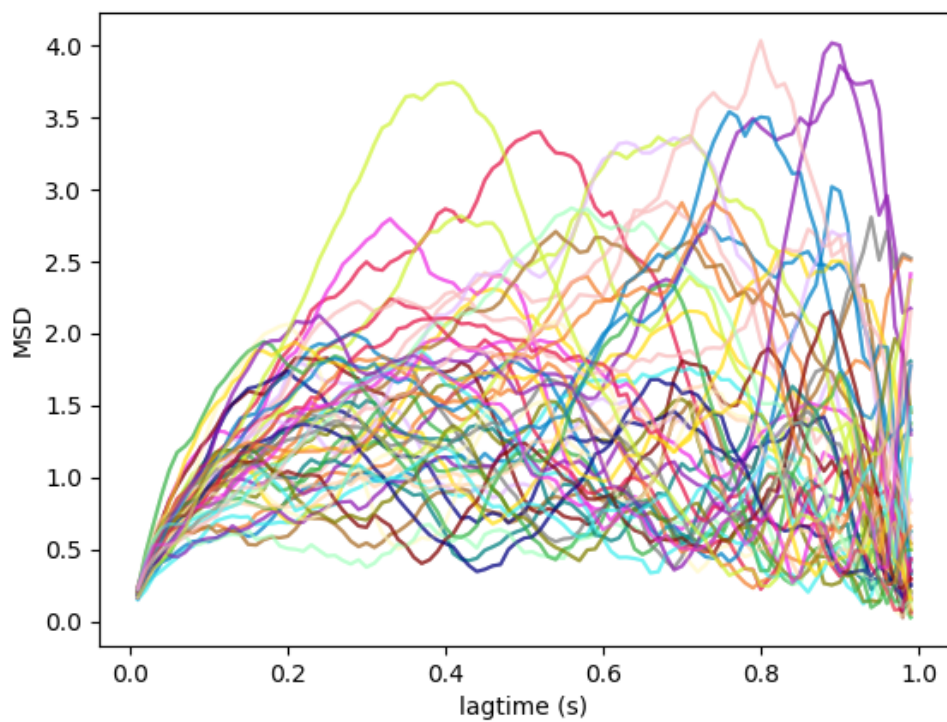


Figure 3.5: Mean squared displacements for 50 particles using the same conditions as in figure 3.4 and $D_{in} = 0.1$.

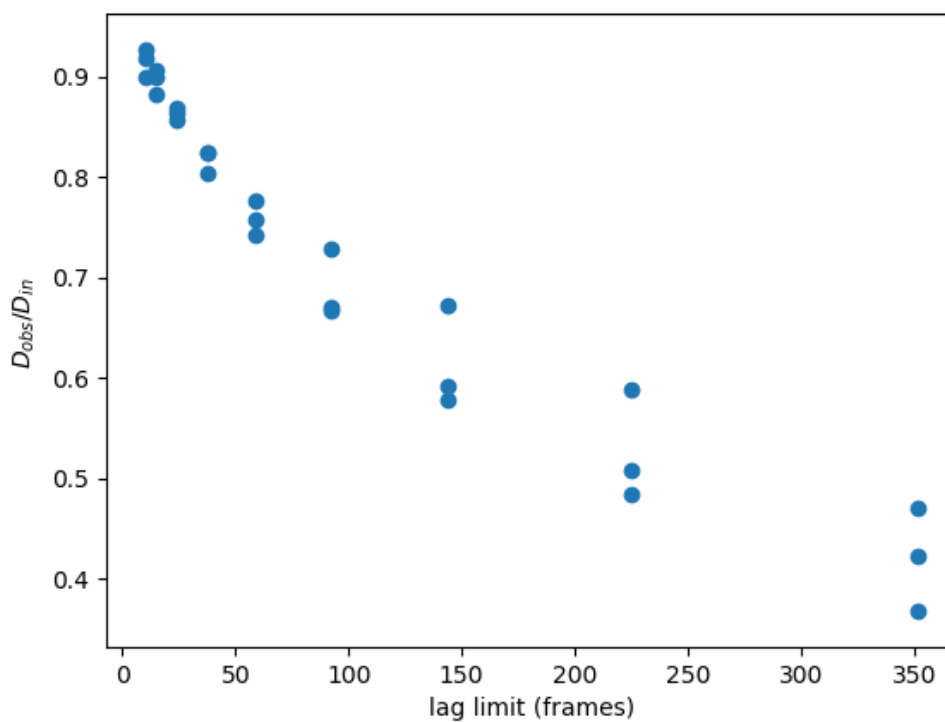


Figure 3.6: D_{obs}/D_{in} of diffusions for particles confined to cells of dimensions 3 by $1\ \mu\text{m}$, where $D_{in} = 0.1$. Each lag limit was repeated 3 times in order to demonstrate that the underestimation is not a function of statistical sampling.

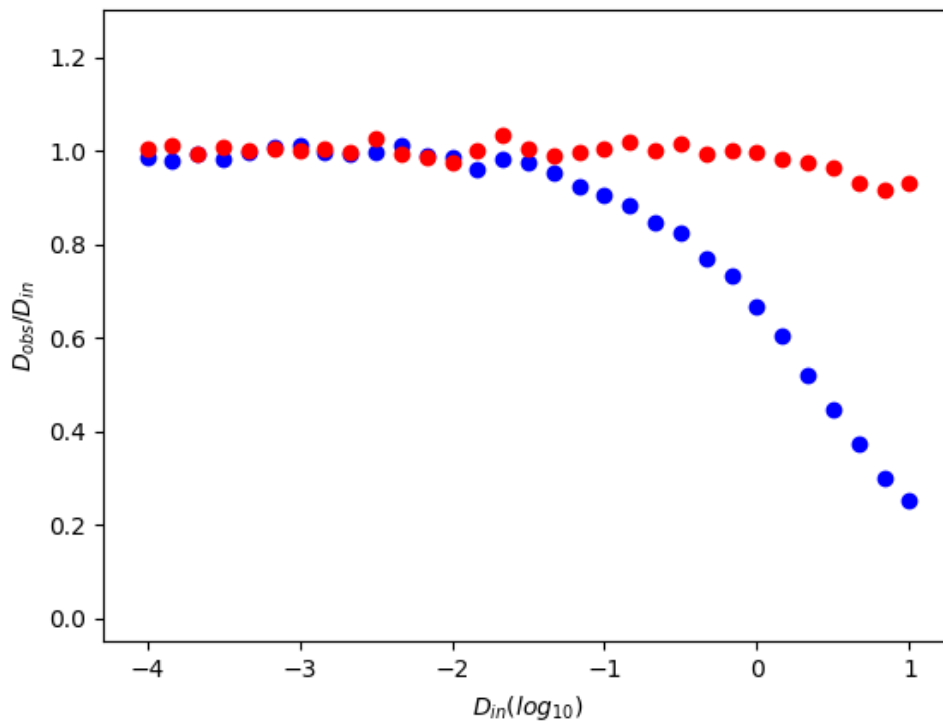


Figure 3.7: D_{obs}/D_{in} of diffusions for particles confined to cells of dimensions 3 by 1 μm , where $D_{in} = 0.1$ and where the simulation timestep is blue) 10ms (as in previous figures) and red) 0.1ms

sizes of around 100 particles, where expected variation is below 5% but particle numbers should be obtainable.

3.1.5 Error in diffusion estimation due to confinement of particles

Since the cell volume is on the same order as the diffusion constants for particles, detailed in section 1.3.3, with that of GFP being $7.7 \mu\text{m}^2 \text{s}^{-1}$, we can expect that confinement of the particles may have some influence on the measurement of particle diffusion. As such we take the simulations in Fig.3.2b and repeat the simulations with the particles confined within a model cell of 1 by $3 \mu\text{m}$.

When particles are confined within the cell in Fig.3.4 we see significant deviation of the D_{obs}/D_{in} ratio at higher diffusion constants with an order of magnitude deviation around $1 \mu\text{m}^2 \text{s}^{-1}$. When we observe the mean squared displacements, Fig.3.5 we see that they saturate at relatively short lag times for high diffusions. Since the simulation assumes the particles start at the centre of the cell this is also the best possible case and therefore in real data the saturation time could be even shorter. A saturation of the MSD is expected as maximum displacement of the particle between any two time points is a function of the length of the cell and not the diffusion of the particle. As such it would be preferable to keep lag times short for analysis of these particles. When this is done as in Fig.3.6 we see that even at very low lagtimes an underestimation of the particle diffusion is still significant and present.

Since confinement must be responsible for the change in behaviour of the observed diffusion constant it is possible that any encounter with the boundary causes problems with observations. As such it would be necessary to obtain sufficient data of particle motion before this point by increasing the rate of measurements. When we decrease the time intervals between measurements as in Fig.3.7 we see that the underestimation decreases as the intervals become arbitrarily small. In practice however, the rate of the measurements is limited by the maximum frame rate of the camera on our microscope setup at 10 ms. So instead, if we use mean square displacement, we must use the simulation data to provide a correction factor for measurements in order to correct for the bias generated by the low frame rate.

3.1.6 Radius of gyration minimises error

Since the mean squared displacement shows significant biases due to the confinement of particles it is reasonable to look for another way to measure diffusion from the data. One method that has been used to infer diffusion constant in the literature is the radius of gyration [109, 120, 121]. This method is normally used in polymer physics to describe the range of motion of a particle chain around a centre of mass. Since the maximum any particle can move is the edge of the cell this measurement would intuitively seem appropriate to use. Since there is no way to directly convert radius of gyration to a diffusion constant or vice versa I decided to test the method on the model to see if it gives a reliable interpretation

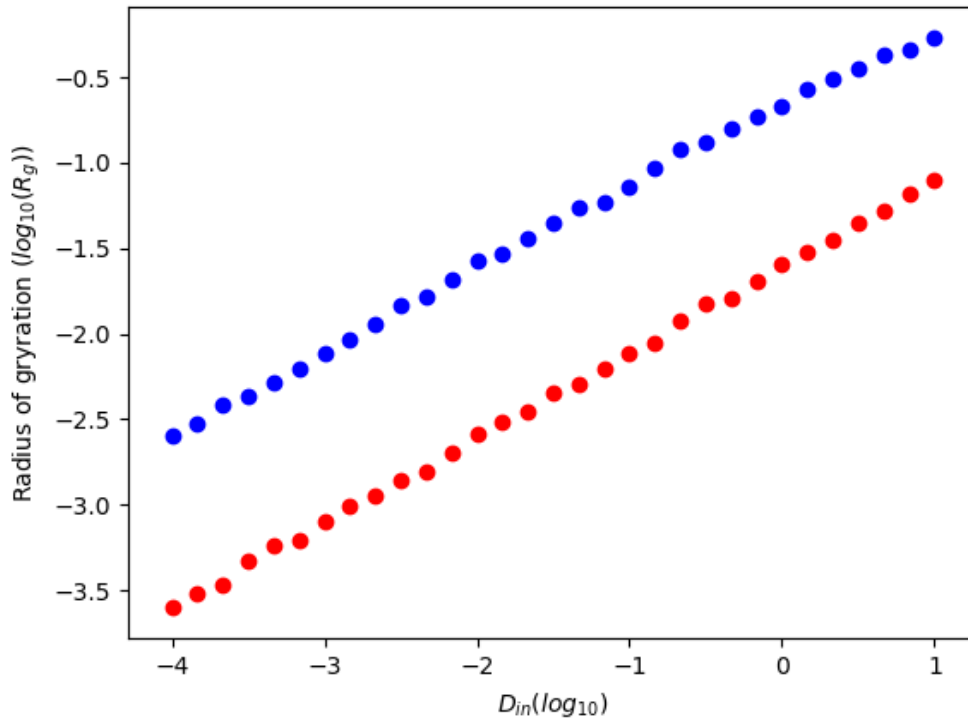


Figure 3.8: Radius of gyration vs input diffusion constant for two different sampling rates; blue:10ms, red:0.1ms. Each data point represents the mean values of 10 simulations with 500 data points and maximum lagtime of 10 time intervals.

of diffusion constant. The equation was modified as follows: For the centroid x_c

$$x_c = \frac{1}{N} \sum_{t=0}^{t=\infty} x_t \quad (3.6)$$

To calculate the radius of gyration r_g

$$r_g = \sqrt{\frac{1}{N} \sum_{t=0}^{lim} (x_t - x_c)^2 + (y_t - y_c)^2} \quad (3.7)$$

Repeating the simulations run in Fig.3.6 with the radius of gyration gives the data in Fig.3.8. The radius of gyration increases linearly with the input diffusion constant without the decrease at high diffusion values seen with the mean square displacement. This is still sensitive to the frame rate if it defines the length of time the radius is calculated for, when this is consistent the radius of gyration produces a reliable result for a given diffusion constant.

3.1.7 Particle localization from microscopy videos

After gathering videos using the method described in Methods 2.2 we must extract tracks for diffusion analysis. In order to create the tracks for analysis

we must first localise each particle inside a given frame. To do this we use a Crocker-Grier centroid-finding algorithm which looks for Gaussian like blobs in the image [122]. For every frame of video, candidate spots of radius 11 pixels and that are above a minimum intensity value greater than 99.8% of the image are chosen. From this an x and y coordinate in pixels is obtained from the frame.

Once an entire video is processed the software links particles in consecutive frames together, producing a complete track of the particle motion. As each cells can only have one particle at a time, the linking can occur with minimal false connections. Since this requires a particle to be detected in every single frame, when a particle leaves the image plane in z or the noise gets too great due to bleaching a single video of a single particle can create multiple tracks of varying length. In order to remove spurious tracks I set the lower limit on the length to 5 frames, this removes any noise related traces that occur when the particle is out of focus or the intensity is below the threshold of the camera. Pixel values are then converted into micrometers (μm) using a previously measured value for the microscope (125nm/px). In addition, for videos with multiple tracks that occur when the particle is out of focus or is bleached, the values of the diffusion constant is averaged under the assumption that each represent the variable distribution of a single particle.

Since each particle is a result of expression of protein attached to GFP, the intensity of the spot formed is directly correlated with the number of proteins, and thus the size of the particle. To obtain an accurate measurement of particle intensity, we perform a z-stack, where multiple images are taken at different z positions on the stage. Since the particle will have the greatest total intensity when perfectly in focus with the z-axis of the scope we identify spots in all slices of the z-stack, and then take the one with the greatest total intensity. This intensity is associated with the entire recording and is used as a proxy for particle size when analysing the data.

3.2 Optical density calibration

3.2.1 Introduction to publication

One of the key measurements used in the later experiments are optical density measurements for identifying the stages of growth and determination of growth rate. As such, early on in the project I attempted to create a simple calibration of optical density to cell number or mass but found significant deviations at high density and in different osmotic conditions. An understanding of calibrations is essential when trying to create a quantitative model of cell growth in varying conditions such as antibiotic tolerance or osmolarity.

Through collaboration with another lab we helped define the conditions which affect the calibration and put their relevance in context with work in bacteria and yeast. We proceeded with the view that knowledge of calibrations and scattering theory are crucial when many groups are using microplate readers to perform high throughput experiments without necessarily considering the effects their testing conditions may have on their data.

For the content of this thesis it is important to understand the relationship between optical density measurements and cell concentration during growth as demonstrated in Fig.4. This is particularly important when dealing with growth in sucrose which changes the refractive index of the medium as shown in paper Fig.S7 and S8.

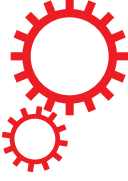
The following chapter is presented as a publication written with the collaboration of Dr Alexander McVey and Dr Teuta Pilizota (Pilizota lab, Edinburgh University), Dr Ivan Clark and Dr Peter Swain (Swain lab, Edinburgh University) [123]. Dr McVey contributed the introduction and much of the derivation of scattering theory, Drs Pilizota and Swain contributed to the experimental design and writing and Dr Clark provided the calibration data for yeast.

3.2.2 Conclusions relevant to this thesis

From the data presented within the paper we can conclude that it is important to calibrate optical densities where they are used as a quantitative measurement of cell growth. Different spectrometers, growth conditions, growth phases and osmolarities will cause changes in calibration curves as a result of cell size or media refractive index changes. As such for data in the rest of this I will endeavour to perform calibration curves as described within the paper to convert to cell concentration. Since this will require a significant amount of cell counting I developed a neural network described in chapter 3.3 to help streamline and automate the process.

3.2.3 Publication: General calibration of microbial growth in microplate readers

SCIENTIFIC REPORTS



OPEN

General calibration of microbial growth in microplate readers

Keiran Stevenson¹, Alexander F. McVey¹, Ivan B. N. Clark², Peter S. Swain² & Teuta Pilizota¹

Received: 04 July 2016

Accepted: 15 November 2016

Published: 13 December 2016

Optical density (OD) measurements of microbial growth are one of the most common techniques used in microbiology, with applications ranging from studies of antibiotic efficacy to investigations of growth under different nutritional or stress environments, to characterization of different mutant strains, including those harbouring synthetic circuits. OD measurements are performed under the assumption that the OD value obtained is proportional to the cell number, i.e. the concentration of the sample. However, the assumption holds true in a limited range of conditions, and calibration techniques that determine that range are currently missing. Here we present a set of calibration procedures and considerations that are necessary to successfully estimate the cell concentration from OD measurements.

Bacteria and yeast are widely studied microorganisms of great economic, medical and societal interest. Much of our understanding of bacterial and yeast life cycles stems from monitoring their proliferation in time and the most routine way of doing so is using optical density (OD) measurements. The applications of such measurements range from routine checks during different cloning techniques¹; through studying cellular physiology and metabolism^{2,3}; to determining the growth rate for antibiotic dosage^{4,5}; and monitoring of biomass accumulation during bio-industrial fermentation⁶. Here we introduce a set of calibration techniques that take into account the relevant parameters affecting OD measurements, including at high culture densities, in a range of conditions commonly used by researchers.

OD measurements have become synonymous with measurements of bacterial number (N) or concentration (C), in accordance with the Beer-Lambert law. However, OD measurements are turbidity measurements^{7,8}, thus the Beer-Lambert law can be applied, with some considerations, only for microbial cultures of low densities. OD measurements in plate readers, increasingly used for high-throughput estimates of microbial growth, operate predominantly at higher culture densities where OD is expected to have a parabolic dependency on N ⁸. Additionally, the proportionality constants (either in low or high density regimes) strongly depend on several parameters, for example cell size, which need to be included in robust calibration techniques. Yet, these techniques, essential when using OD measurements for quantitative studies of microbial growth, including growth rates, lag times and cell yields, have thus far not been established.

The Beer-Lambert law (Supplementary Note 1) assumes that light is only absorbed to derive $OD \sim C$, which is true if the light received by the detector of a typical spectrophotometer is the light that did not interact with the sample in any way^{7,9}. In general, when microbial cells are well dispersed in the solution (for the cases where N is small, i.e. single scattering regime) and the geometry of the spectrophotometer is suitable, the Beer-Lambert law is a good approximation for turbidity measurements, and N (or C) is $\sim OD^{7,8}$. By the suitable geometry of the spectrophotometer, we mean the likelihood of the scattered light reaching the detector in the spectrophotometer even in the single scattering regime (Fig. 1A,B).

Most bacteria and yeast scatter light at small angles (a few degrees)¹⁰, and, thus, the distance from the scatterer to the detector (d) and the radius (R) of the aperture (Fig. 1A) will determine how close a particular spectrophotometer is to the ideal case, even in the single scattering regime. Supplementary Figure 1A shows measurements taken of the same sample in five different spectrophotometers, indicating that different spectrophotometers need to be cross-calibrated even when used in the single scattering regime^{9,11}. As N increases the probability of incident light being scattered by particles multiple times also increases (Fig. 1B), the so-called multiple scattering regime. In this regime the Beer-Lambert law is no longer a suitable approximation, and OD is expected to have a parabolic dependency on N ⁸. Similarly, as the probability of multiple scattering events increases even further (i.e. for very high N), light is increasingly deflected away from the detector, and can be described with diffusive

¹Centre for Synthetic and Systems Biology, School of Biological Sciences, University of Edinburgh, Roger Land Building, Alexander Crum Brown Road, Edinburgh, EH9 3FF, United Kingdom. ²Centre for Synthetic and Systems Biology, School of Biological Sciences, University of Edinburgh, CH Waddington Building, Mayfield Road, Edinburgh EH9 3JD, UK. Correspondence and requests for materials should be addressed to T.P. (email: teuta.pilizota@ed.ac.uk)

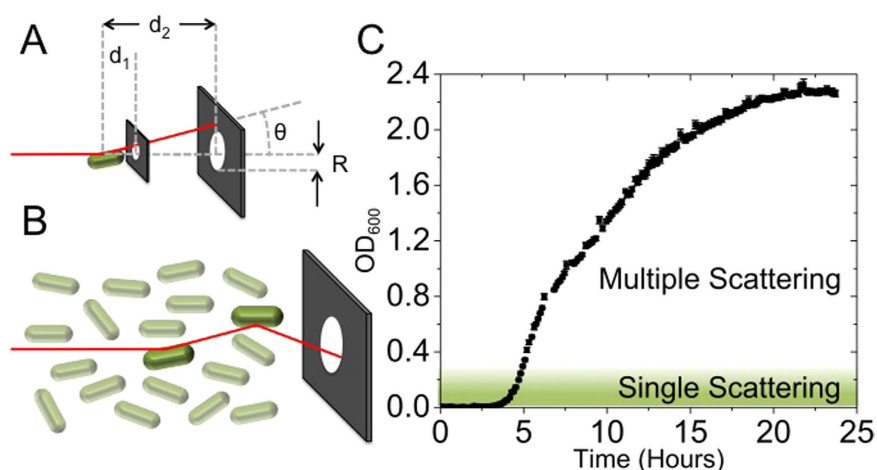


Figure 1. Schematic showing that light incident on a sample is scattered by an angle θ from the optical axis (z), either once as in (A) or multiple times (B). Single scattering events are more likely to deflect light away from the aperture (radius R), but the effect of this scattering is highly dependent upon the size of the detector and the distance between detector and sample (d_1 or d_2). As the concentration of cells increases, the probability of light being scattered back into the detector is increased. (C) A typical OD curve for *E. coli* measured at $\lambda = 600$ nm (for measurements at different λ see Supplementary Fig. 2). The depicted curve is the mean value of ten replicate measurements (performed in separate wells of the same plate in the microplate reader and on independent days and separate plates). Error bars are the standard error of the mean. Where the error bars are not visible, they are smaller than the data symbols. Single and multiple scattering regimes have been indicated with different colour shading. The OD saturates when N is large enough to deplete the nutrient sources in the media.

approximations (the so-called photon diffusion limit)^{12,13}. Figure 1C shows a typical OD curve for *Escherichia coli* grown in rich media, with the single and multiple scattering regimes indicated.

In the single scattering regime (small N and $OD_{600} \lesssim 0.2$)^{8,13,14}, where the Beer-Lambert law ($OD \sim N$) approximately holds, exact solutions to the scattering problem exist⁹. Depending on the size and shape of the scatterer (bacteria or yeast), as well as difference in the index of refraction between the scatterer and the media, various approximations have been used (Supplementary Table 1). For example, the Jöbst approximation, used for spherical bacteria with dimensions comparable to the wavelength of light ($r \sim \lambda$, where r is radius of the bacteria and λ the wavelength of incident light), gives the OD to be proportional to N and r^4 (i.e. bacterial volume to the power of four thirds)¹⁵.

Multiple scattering effects can be incorporated into scattering theory with the inclusion of a correction factor $CF(\sigma, z)$ (Supplementary Note 2), but, unfortunately, to calculate the correction factor, N must be known. Therefore, when using microplate readers in the multiple scattering regime the most practical way of determining the relationship between OD and N is to calibrate. Correct calibration is of particular relevance to high-throughput measurements of quantitative growth rate and cell yield in plate readers and bio-reactors, but it is rarely reported. Additionally, it is often assumed that a single calibration curve for a given instrument is sufficient¹⁶, or calibration is performed by counting colony forming units (CFUs)¹⁷, which only includes live bacteria and is not necessarily suitable for growth under different antibiotics (where cells can be dead, but not lysed). For correct calibration, the shape and size changes of scatterers (bacteria and yeast) as well as index of refraction changes of the media (n_m) and/or of scatterers (n_p) need to be taken into account.

Results

Smaller scatters have higher concentrations for a given OD. To demonstrate the effect of differences in the size of scatterers on OD in the single and multiple scattering regimes, we measured monodisperse solutions of beads with different diameters (D), known index of refraction and known concentrations (C) determined by direct counting in a microscope. Calibration curves for each sample of beads are given in Fig. 2A. For a fixed OD, C increases as the diameter of the scatter decreases (Fig. 2B). The relative effect of C on OD is more pronounced for $D \sim \lambda$, in both the single and multiple scattering regimes, indicating that any changes in size for yeast cultures (with typical cell size $\sim 5 \mu\text{m}$) should affect the calibration curve less than those for bacterial cultures (with typical cell size $\sim 1 \mu\text{m}$). Similar conclusions also hold true for samples heterogeneous in size. Upon introduction of a polydisperse sample of $0.5 \mu\text{m}$ and $1.0 \mu\text{m}$ diameter beads (a 1:1 mixture by volume), C is seen to deviate greatly from both monodisperse solutions (Fig. 2C). Consequently, while the OD versus C calibration curves follow similar trends (a second order polynomial)⁸, the exact calibration curve is highly dependent upon D , particularly for $D \sim \lambda$.

Calibration of OD typically changes with growth conditions and cell size. The effects of changing the size of the scatterer seen in bead suspensions are also visible in cultures of *E. coli* and yeast measured in a plate reader (Fig. 3A and Methods). The representative images (Fig. 3B–H) show the change in cell geometry. We obtained different cell sizes for *E. coli* by sampling either at different stages of growth in rich undefined media (Supplementary Fig. S4) or by growing the culture in the presence of a sublethal concentration of ampicillin, a

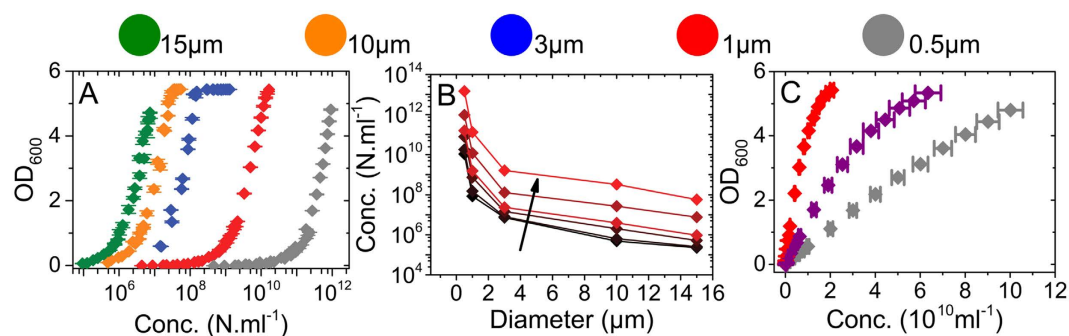


Figure 2. OD measurements of spherical polystyrene bead suspensions. Each set of data (for a given bead size) consists of dilutions of two independently prepared stock solutions whose actual concentration was determined by counting in a microfluidic slide (Methods). For each independently prepared dilution series at least five experimental replicates were performed and plotted as averages with standard errors. Where independent dilution series were prepared for the same bead size these are plotted with the same colour. The differences between independently prepared and counted dilution series for the same bead size are so small that the data overlap. Any error bars that are not visible are smaller than the data symbols. Bead size corresponds to the diagram above the graphs ($0.51 \pm 0.01 \mu\text{m}$, $0.96 \pm 0.07 \mu\text{m}$, $3.00 \pm 0.07 \mu\text{m}$, $10.0 \pm 0.6 \mu\text{m}$ and $15.7 \pm 1.4 \mu\text{m}$) and bead index of refraction is $n_p = 1.59$. Representative images of beads used for C measurements are shown in Supplementary Figure 3. (A) Comparison of concentrations (Methods) and measured OD in a microplate reader for a given bead diameter. (B) The bead concentration as a function of D obtained from (A) for the following ODs: 0.05, 0.1, 0.5, 1 and 10. Increasing OD is represented as increasing brightness of red and by the arrow. (C) Measurements of $0.5 \mu\text{m}$; $1.0 \mu\text{m}$ bead suspensions and the resultant (1:1 by volume) mixture in purple.

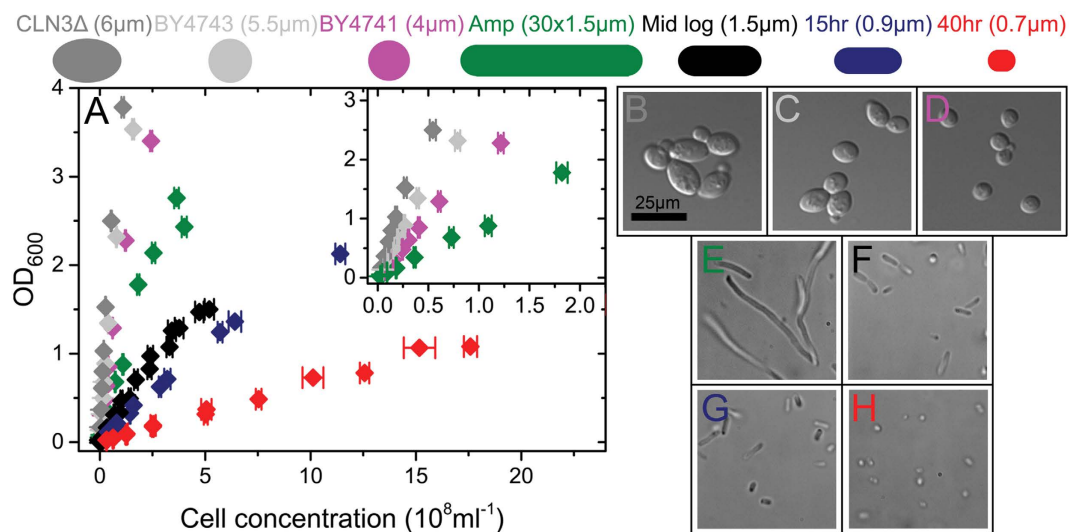


Figure 3. (A) OD vs. C is shown for yeast diploids (grey); yeast haploid (purple); filamentous (green) and mid-log (black) *E. coli*; and early (blue) and late (red) stationary phase *E. coli* using dilutions of at least two cell stock solutions prepared from cells grown on different days. Actual cell concentrations were determined by counting in a microscope. For each independently prepared dilution series at least five experimental replicates were performed and are plotted as averages with standard errors. Independent dilution series that were prepared for the same cell size are plotted with the same colour. For cells of the same size, the differences between independently prepared and counted dilution series are so small that the data overlap. Error bars that are not visible are smaller than the data symbols. (B–H) Representative images of each culture obtained during microscopy. The scale bar is shown in B and applies to all panels. (B) Yeast CLN3 Δ homozygous diploid mutant (C) Yeast diploid, (D) Yeast haploid. (E) *E. coli* cells grown in the presence of sub lethal concentration of ampicillin to induce filamentation. (F) *E. coli* cells grown to mid log phase in LB (OD = 0.2). (G) *E. coli* cells at early stationary phase (OD = 2.3), (H) *E. coli* cells at late stationary phase (after 40 hr).

β -lactam antibiotic that inhibits the formation of the cell wall. Ampicillin induces filamentation^{18,19} (Fig. 3E), a property shared by many other stresses (including the antibiotic groups cephalosporins and quinolones²⁰ and UV

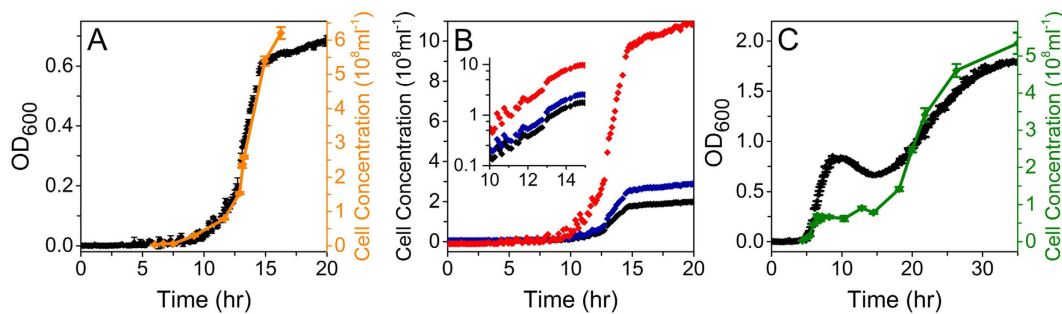


Figure 4. Growth curves and cell counts. (A) OD (black) and cell concentration (orange) during growth of *E. coli* in MM9 with glucose. OD and C are correlated until starvation when cell size is no longer constant. (B) The OD curve from (A) converted to cell concentration using the the mid-log (black), 15 hr (blue) and 40 hr (red) curves in Fig. 3A. Calibration performed on cells of different sizes produces substantial differences in cell concentration. (C) OD (black) and cell concentration (green) in LB with 9 Ampicillin. The lack of correlation between OD and C is caused by antibiotic induced filamentation and filaments of fluctuating length during growth. For (B) and (C), the OD curve shown is an average with standard errors of 10 independent experimental replicates. Each cell concentration point is an average count with the standard error obtained from counting 20–50 independent fields of view in a microscope (Methods).

irradiation and oxidative damage²¹). We obtained different sizes of yeast cells by using three different strains (wild type haploid and diploid and a diploid mutant exhibiting increased cell size)²².

Each chosen scatterer in Fig. 3 exhibits a different relationship between OD and C. In particular, the calibration curve obtained using filamentous cells is considerably altered compared to the rest of the *E. coli* samples. The differences in the calibration of the yeast samples (as D increases from 4 μm to 6 μm) are smaller compared to those of the bacterial cultures.

The effects of changes in the calibration curve during a single growth curve are demonstrated in Fig. 4 and Supplementary Figure 5 by counting the cell concentration in parallel with measuring the OD. We first show that if the cell size does not change during the growth of the culture, the calibration curve maintains a parabolic dependency on N (Fig. 4A). To maintain a constant cell size, we grew *E. coli* in MM9 with glucose as the sole carbon source (Methods). Under these conditions OD and C are correlated throughout the exponential growth, only diverging at 15 hr when the carbon source is depleted and the cells enter stationary phase and reduce in volume. Nevertheless, if cells change size during growth, for example when growing on rich undefined media (Supplementary Fig. 5), the calibration curve will change in time as well. To demonstrate the effect of using calibration curves obtained for cells of different sizes, in Fig. 4B we show the OD curve from Fig. 4A converted to C using three different calibration curves. C is substantially altered depending on the calibration curve selected, with the effect on the lag time and final cell yield being particularly pronounced.

To further demonstrate the effect on changes in cell size throughout the growth curve we grew *E. coli* under sublethal concentrations of ampicillin (Fig. 4C). A substantial deviation between OD and C is visible. During the initial part of the log phase OD and C show the same time dependency. At OD ~ 0.2 , however, N remains roughly constant while the OD increases. This increase in OD for constant N is the result of an increase in cell mass (as cells filament and increase in size), rather than increasing N (Fig. 3E). The decrease in OD at constant N (10 hr) is most likely the result of division of filaments into smaller cells. 15 hr after culture inoculation, both N and OD increase again as filamentous bacteria both divide and grow as smaller cells.

There can be a substantial difference between the expected OD and C relationship for scatterers of a fixed size and those whose size changes during growth. For example, in Supplementary Figure 5 we show comparison of OD and C from Fig. 4A and 4C. For a constant cell size (Supplementary Fig. 5A), the calibration curve follows the same second degree polynomial expected from Figs 2A and 2C and 3A, whereas for growth in LB+ampicillin, where cell size changes, the calibration curve is more complex (Supplementary Fig. 5B). Supplementary Figure 6 shows the difference between growth rates obtained from non-calibrated OD and C measurements for the same cell culture. The value and time point at which maximum growth rate is reached in Supplementary Figure 6A (corresponding to Fig. 4A) are similar, whereas Supplementary Figure 6B shows that maximum growth rate obtained from Fig. 4C is reached several hours before the maximum growth rate obtained from OD measurements. Additionally, Supplementary Figure 6B shows that the two values differ significantly, by a factor of two.

Calibration changes with the refractive index of the growth media. Apart from the size of the scatterer, changes in the difference between refractive index of the growth media (n_m) and the refractive index of the scatterer (n_p) can have a significant effect on the OD calibration curve. For example, we changed n_m by the addition of sucrose, while keeping the refractive index of the scatterer (1 μm bead) the same (Supplementary Fig. 7). As the relationship $n = \frac{n_p}{n_m}$ decreases, the OD of a fixed N is similarly reduced. The effect is small for beads as the relative difference between n_p and n_m is large, but will be more pronounced for biological samples like bacteria, which have a smaller n (Supplementary Table 2).

Finally, we investigated the effect of bacterial lysis and intracellular matter leaking into the media on n_m , which can occur during growth under antibiotics. We measured the refractive index of LB media with different

concentrations of lysed *E. coli* cells. The intracellular material (Supplementary Table 3 and Supplementary Fig. 8), released into the media from high concentrations of cells (as high as $2 \cdot 10^9 \text{ ml}^{-1}$ cells) results in only a small increase in n_m . The increase is substantially lower than n_m variations caused by the introduction of even low concentrations of sucrose to ddH₂O (Supplementary Fig. 8). Thus, cell lysis as a result of growth under different antibiotics will unlikely change n_m sufficiently to alter the OD versus C calibration curve. Nevertheless, growth at high sugar concentrations, such as in the food industry, will.

Discussion

We have presented potential issues and the calibration protocols needed for quantitative measurements of microbial growth rates based on OD measurements. We show that different spectrophotometers and microplate readers need to be cross-calibrated to compare the OD readings as an absolute number. Furthermore, variations in diameter D and refractive index of the cell or of the media need to be considered and calibrated to avoid substantially over- or underestimating the number of cells present in the sample. Therefore, we recommend first determining if considerable changes in cell size are expected during growth of the culture. If not, and size is expected to remain constant, calibration of OD against N needs to be performed once for each D and index of refraction, and ideally reported in publications. The closer the D of the scatterer to λ , the more important it is to perform calibration of OD against N for each different cell size. Changes in refractive index can be particularly relevant during growth in media with high sugar concentrations (such as those in food sciences^{23–26} and drinks with high osmolarity like beer). We have shown that changes in n_m due to lysis induced leakage of cell material, for example when grown in the presence of antibiotics, are small. However, we note that the effect of changing media index of refraction is likely to be more pronounced in bioreactor experiments where C is far larger. If cell size is expected to change substantially during the course of growth of the microbial culture (for example: growth under antibiotics or various other stresses, growth of shape-inducing mutants, growth of over-expression strains, and growth of strains that induce chains or clumps), OD measurements are no longer suitable and direct counting of N should be performed, using, for example, microscopy.

Methods

Bacteria cultures. All bacterial cell culture studies were conducted using *E. coli* BW25113 (F⁻, DE(araD-araB)567, lacZ4787(del)::rrnB-3, LAM⁻, rph-1, DE(rhaD-rhaB)568, hsdR514), a close relative of MG1655, with plasmid pWR20 which expresses and enhanced GFP for cytoplasmic volume monitoring²⁷. All experiments were conducted in LB media except where explicitly stated. MM9 medium contained 0.1% Glucose, no amino acids and 20 mmol KCl. MM9 (Modified M9) is of the same composition as M9²⁸ except sodium phosphate buffer only was used. Where cells were grown with antibiotics, 9 $\mu\text{g ml}^{-1}$ Ampicillin was added to the culture medium before the addition of cells.

Yeast cultures. Yeast studies used three S288c-derived strains: BY4741, BY4743²⁹ and the *cln3* homozygous deletion derived from the *Saccharomyces* genome deletion project³⁰. Cells were cultured at 30 °C in YPD media, containing 2% glucose.

Colloidal bead cultures. Colloidal bead cultures were created using dilutions of polystyrene beads of known diameter (D) $0.51 \pm 0.01 \mu\text{m}$ (Polysciences), $0.96 \pm 0.07 \mu\text{m}$ (Bangs Laboratory), $3.00 \pm 0.07 \mu\text{m}$, $10.0 \pm 0.6 \mu\text{m}$ and 15.7 ± 1.4 (all Polysciences) and known index of refraction ($n_p = 1.59$) in ddH₂O. At each D , a dilution series was performed, to produce samples of known concentrations (C) between 10^5 and $10^{12} \text{ N ml}^{-1}$. For all samples C was experimentally determined by counting the number of beads in 10 of the dilution in a microscope tunnel slide²⁷.

Optical density measurements. OD measurements of bacterial and colloidal bead cultures were performed in a Spectrostar Omega microplate reader (BMG, Germany) with a Costar Flat Bottom 96-well plate with lid and 200 μl per well (300 μl for data in Fig. 4). Absorbance was measured at wavelength 600 and temperature 37 °C and the mean of 5 readings taken. For bacterial cultures, 30 wells were grown to OD = 0.15 in MM9 medium. The wells were pooled and 125 $\mu\text{g ml}^{-1}$ chloramphenicol was added to inhibit further cell division or growth. The cells were then diluted in increments to provide a range of OD readings. A single dilution of cells for each series was then imaged in the brightfield microscope as above for the polystyrene beads. All measurements in the main text were reported using the BMG with correction values, which is given as the measured OD multiplied by 1.0560 for 300 μl , 1.5848 for 200 μl and 6.3694 for 100 μl .

OD measurements for yeast cultures were performed in a Tecan M200 fluorescent spectrophotometer, using a Costar Flat Bottom 96-well plate with lid and 200 μl per well for all measurements. Cells were cultured for 16 hr in YPD media and dilutions for measurement made in the same media. Duplicate OD measurements were taken at 600 nm (bandwidth 9) with 15 flashes at 30 °C. Yeast cell counts were performed using a Neubauer improved bright-line haemocytometer (Marienfeld).

Calibration between the two spectrophotometers was performed using *E. coli* grown in LB to mid log as in Fig. 3A black and the OD measured in both platereaders. The relative difference in measurements was then calculated and used to correct the data gathered for yeast. The calibration is shown in Supplementary Figure 1B.

Brightfield Microscopy. Imaging of samples was performed using a custom-built brightfield microscope consisting of a 100 \times oil immersion objective lens (Nikon) with the sample mounted on a Nano-LP200 piezoelectric stage (Mad City Labs). Illumination of the sample was provided by a white LED (Luxeon Star) and images recorded on an iXon Ultra 897 EMCCD camera (Andor). Stacks of images through each sample were acquired every 0.05 s and separations of 1 μm , ensuring all scatterers in the volume were identified without introducing overcounting. True values of C were experimentally determined by counting N present in the known stack

volume determined by the field of view of the microscope ($55.6 \times 55.6 \times 100 \mu\text{m}$). For each each bead preparation in Fig. 2 between 20–50 independent fields of view were counted. Similarly, for each cell preparation in Fig. 3 we counted 20–50 independent fields of view. For each bead or cell size given in Figs 2 and 3, we used at least two independent stock solutions/cultures (from which dilution series were prepared). In Fig. 4A and C each concentration of cells was counted independently, again using 20–50 independent fields of view.

Osmolarity measurements. For osmolarity measurements, beads ($D = 1 \mu\text{m}$) were diluted from manufacturer stock solution into ddH₂O and then further diluted into solutions of 0 mOsm, 116 mOsm, 231 mOsm, 463 mOsm and 925 mOsm (achieved by diluting sucrose (Sigma) in ddH₂O) to produce concentrations in media of refractive index $n_m = 1.333; 1.339; 1.344; 1.353$ and 1.368 respectively. For each osmolarity, C was determined by counting N using brightfield microscopy as above. Osmolalities were measured using a freezing point depression osmometer (Camlab).

Fitting of bead optical density measurements. Fitting of the data presented in Fig. 2A was performed in the Matlab³¹ environment utilising the built in curve fitting tools. Data was first trimmed to remove points where the spectrophotometer had saturated then fitted as a 2nd degree polynomial with robust fitting using the bisquare method. The polynomials found are presented in Supplementary Table 4. These polynomials were then solved for $\text{OD} = 0.05, 0.1, 0.5, 1$ and 10 to give the traces presented in Fig. 2C.

***E. coli* cell concentration monitoring during growth curves.** In order to determine C during batch culture growth, cells were added to 10 ml of the experimental media, which was then divided among 30–60 wells of a 96-well plate. The cells were grown at 37°C and OD measured every 7.5 min. When an increase in OD above the baseline was observed sampling for C began, with each new sample taken from a separate well. For all growth curves at least 8 wells were left untouched to provide a complete growth curve for comparison. In the rare cases where the growth curve deviated significantly from the average, those traces were excluded from all measurements. $125 \mu\text{g ml}^{-1}$ chloramphenicol was added to samples taken from the plate to arrest all cell division and growth. Samples were then imaged under brightfield illumination and N counted manually to determine C for each time point. At $\text{OD} > 0.2$ samples were diluted in the culture medium to reduce cell overlap in the slide. For Fig. 4 the two data sets were aligned by using a least squares method to determine the scales of both axes, minimising the sum of: $(\frac{Y_{chase}}{c} - Y_{OD})^2$ where c is the scaling factor. For Supplementary Figure 5 solid and dashed fits were produced using 1st and 2nd degree polynomials respectively. The fitted region for each was selected by expanding sequentially from zero until the fit quality started to drop.

Refractive index measurements. *E. coli* cells (strain MG1655) were grown in LB to $\text{OD} = 0.3$, spun down and concentrated $33.3 \times$ before being subjected to sonication to lyse the cells. This cell lysate was diluted to $0.0625 \times, 0.125 \times, 0.25 \times, 0.5 \times$ and $1 \times$ concentrations and the refractive index measured. The original cell extract was counted as above to determine the concentration of cells before lysing. DNA was obtained as 23-mer primers (Sigma-Aldrich) suspended in ddH₂O, with concentration measured using a NanoDrop (ThermoScientific). Refractive indices of solutions were measured in a manual refractometer (Bellingham and Stanley, London). Sucrose data was obtained from a standard brix index³².

Raw data. Raw data generated as part of this work is available at <http://datashare.is.ed.ac.uk/handle/10283/2063> (Figs 1, 2 and 3) and <http://datashare.is.ed.ac.uk/handle/10283/2064> (Fig. 4).

References

- Neidhardt, F. C. *Escherichia coli and Salmonella: Cellular and Molecular Biology* (ASM, 1996).
- Klumpp, S., Zhang, Z. & Hwa, T. Growth Rate-Dependent Global Effects on Gene Expression in Bacteria. *Cell* **139**, 1366–1375 (2009).
- Scott, M., Gunderson, C. W., Mateescu, E. M., Zhang, Z. & Hwa, T. Interdependence of Cell Growth and Gene Expression: Origins and Consequences. *Science* **330**, 1099–1102 (2010).
- Andrews, J. M. Determination of minimum inhibitory concentrations. *J Antimicrob Chemoth* **48**, 5–16 (2001).
- Bollenbach, T., Quan, S., Chait, R. & Kishony, R. Nonoptimal Microbial Response to Antibiotics Underlies Suppressive Drug Interactions. *Cell* **139**, 707–718 (2009).
- Mahalik, S., Sharma, A. K. & Mukherjee, K. J. Genome engineering for improved recombinant protein expression in *Escherichia coli*. *Microb Cell Fact* **13**, 177 (2014).
- Koch, A. L. Some Calculations on the Turbidity of Mitochondria and Bacteria. *Biochim Biophys Acta* **51**, 429–441 (1961).
- Koch, A. L. Turbidity measurements of bacterial cultures in some available commercial instruments. *Anal Biochem* **38**, 252–259 (1970).
- Koch, A. L. Theory of the angular dependence of light scattered by bacteria and similar-sized biological objects. *J Theor Biol* **18**, 133–156 (1968).
- Koch, A. L. & Ehrenfeld, E. The size and shape of bacteria by light scattering measurements. *Biochim Biophys Acta* **165**(2), 262–273 (1968).
- Koch, A. L. Distribution of Cell Size in Growing Cultures of Bacteria and the Applicability of the Collins-Richmond Principle. *J. Gen. Microbiol.* **45**(3), 409–417 (1966).
- Zaccanti, G., Del Bianco, S. & Martelli, F. Measurements of optical properties of high-density media. *Appl Opt* **42**(19), 4023–4030 (2003).
- Ishimaru, A. Approximate solutions for tenuous media in *Wave Propagation and Scattering in Random Media*. (Wiley-IEEE Press, 1997).
- Giusto, A. *et al.* Optical properties of high-density dispersions of particles: application to intralipid solutions. *Appl Opt* **42**(21), 4375–4380 (2003).
- Baranyi, J. Comparison of Stochastic and Deterministic Concepts of Bacterial Lag. *J Theor Biol.* **192**, 403–408 (1998).

16. Warringer, J. & Blomberg, A. Automated screening in environmental arrays allows analysis of quantitative phenotypic profiles in *Saccharomyces cerevisiae*. *Yeast* **20**(1), 53–67 (2003).
17. Jung, J. H. & Lee, J. E. Real-time bacterial microcolony counting using on-chip microscopy. *Sci Rep* **6**, 21473 (2016).
18. Buijs, J., Dofferhoff, A. S. M., Moutona, J. W., Wagenvoorta, J. H. T. & van der Meer, J. W. M. Concentration-dependency of β -lactam-induced filament formation in Gram-negative bacteria. *Clin Microbiol Infect* **14**(4), 344–349 (2008).
19. Miller, C. SOS response induction by beta-lactams and bacterial defense against antibiotic lethality. *Science* **305**(5690), 1629–1631 (2004).
20. Diver, J. M. & Wise, R. Morphological and biochemical changes in *Escherichia coli* after exposure to ciprofloxacin. *J. Antimicrob. Chemother.* **18**, 31–41, Supplement D (1986).
21. Yao, Z., Kahne, D. & Kishony, R. Distinct single-cell morphological dynamics under beta-lactam antibiotics. *Mol. Cell* **48**(5), 705–12 (2012).
22. Jorgensen, P., Nishikawa, J. L., Breikreutz, B. J. & Tyers, M. Systematic identification of pathways that couple cell growth and division in yeast. *Science* **297**, 395–400 (2002).
23. Offersgaard, J. F. & Öjelund, H. Correction of Nonlinear Effects in Absorbance Measurements. *Appl Spectrosc* **56**, 469–476 (2002).
24. Prüß, B. M., Nelms, J. M., Park, C. & Wolfe, A. J. Mutations in NADH:Ubiquinone Oxidoreductase. *J Bacteriol* **176**(8), 2143–2150 (1994).
25. Sezonov, G., Joseleau-Petit, D. & D'Ari, R. *Escherichia coli* physiology in Luria-Bertani broth. *ASM* **189**(23), 8746–8749 (2007).
26. Zhao, L., Zhang, H., Hao, T. & Li, S. *In vitro* antibacterial activities and mechanism of sugar fatty acid esters against five food-related bacteria. *Food Chemistry* **187**, 370–377 (2015).
27. Pilizota, T. & Shaevitz, J. W. Plasmolysis and cell shape depend on solute outer-membrane permeability during hyperosmotic shock in *E. coli*. *Biophys J* **104**(12), 2733–2742 (2013).
28. Cold Spring Harbour Laboratory. M9 minimal medium (standard). *Cold Spring Harb Protoc*, doi: 10.1101/pdb.rec12295 (2010).
29. Brachmann, C. B. *et al.* Designer deletion strains derived from *Saccharomyces cerevisiae* S288C: a useful set of strains and plasmids for PCR-mediated gene disruption and other applications. *Yeast* **14**(2), 115–32 (1998).
30. Winzeler, E. A. *et al.* Functional characterization of the *S. cerevisiae* genome by gene deletion and parallel analysis. *Science*. **285**(5429), 901–906 (1999).
31. The MathWorks Inc. *MATLAB and Statistics Toolbox Release 2015b* (The MathWorks Inc, Natick, Massachusetts, United States). (2015).
32. Snyder, C. F. & Hattenburg, A. T. *Refractive indices and densities of aqueous solutions of invert sugar*. Washington D.C. USDoC, National Bureau of Standards. <http://digital.library.unt.edu/ark:/67531/metadc70449/> Accessed: 20 June 2016.

Acknowledgements

KS is supported by the BBSRC iCASE grant to TP. AFM, IBNC, PSS and TP acknowledge the support of UK Research Councils Synthetic Biology for Growth programme and KS, AFM, IBNC, PSS and TP are members of a BBSRC/EPSC/MRC funded Synthetic Biology Research Centre. TP acknowledges the support of BBSRC CBMNet grant. We thank Jerko Rosko, Dejan Kunovac and all other members of the Pilizota and Swain lab for their comments and support, Andrew Schofield for granting us access to the refractometer and Meriem El Karoui and Rosalind Allen for helpful comments and discussions.

Author Contributions

T.P. and K.S. designed the study. T.P., K.S. and P.S.S. conceived the experiments. T.P., K.S. and I.B.N.C. performed the experiments and analysed the data. K.S., A.F.M. and T.P. interpreted the data and wrote the paper. All authors reviewed the manuscript.

Additional Information

Supplementary information accompanies this paper at <http://www.nature.com/srep>

Competing financial interests: The authors declare no competing financial interests.

How to cite this article: Stevenson, K. *et al.* General calibration of microbial growth in microplate readers. *Sci. Rep.* **6**, 38828; doi: 10.1038/srep38828 (2016).

Publisher's note: Springer Nature remains neutral with regard to jurisdictional claims in published maps and institutional affiliations.

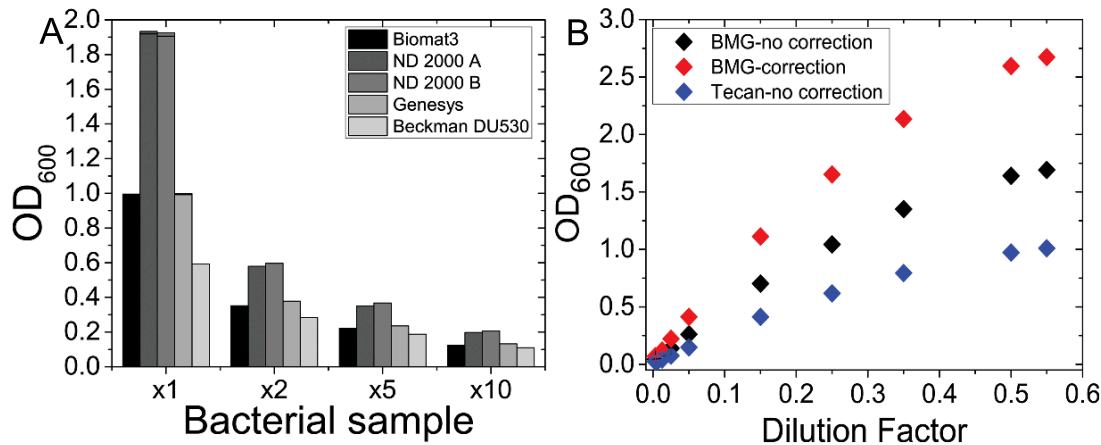


This work is licensed under a Creative Commons Attribution 4.0 International License. The images or other third party material in this article are included in the article's Creative Commons license, unless indicated otherwise in the credit line; if the material is not included under the Creative Commons license, users will need to obtain permission from the license holder to reproduce the material. To view a copy of this license, visit <http://creativecommons.org/licenses/by/4.0/>

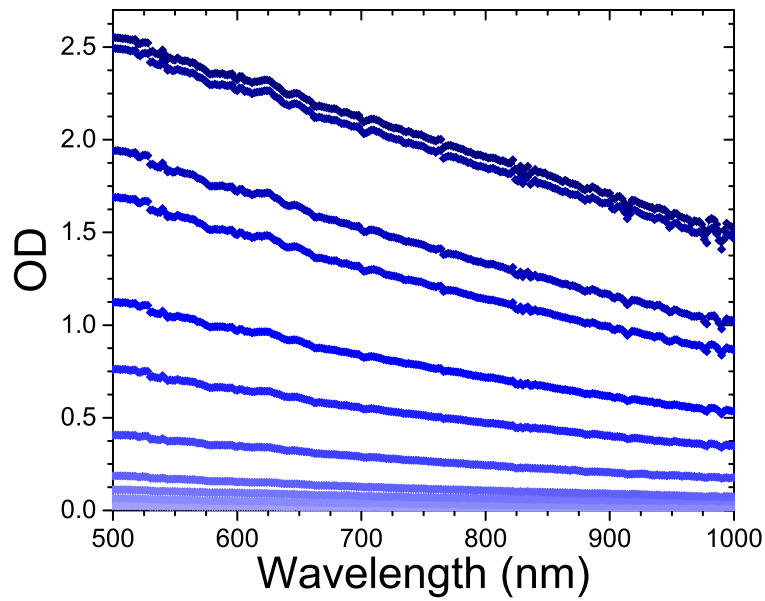
© The Author(s) 2016

Supplementary Information for “General calibration of microbial growth in microplate readers”

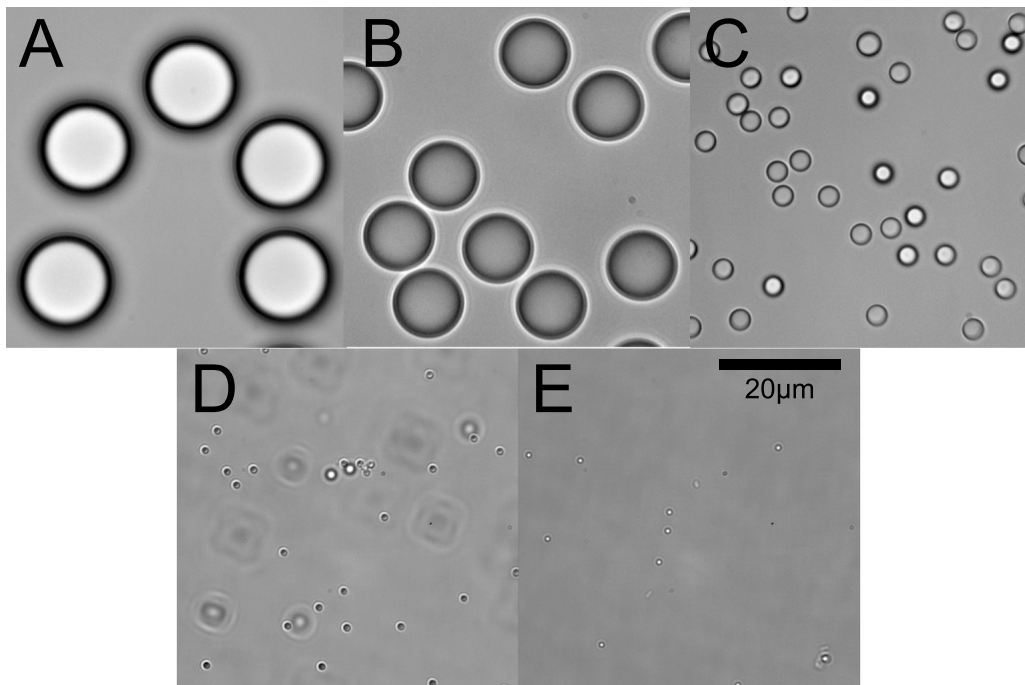
Keiran Stevenson, Alexander F. McVey, Ivan B. N. Clark, Peter S. Swain and Teuta Pilizota



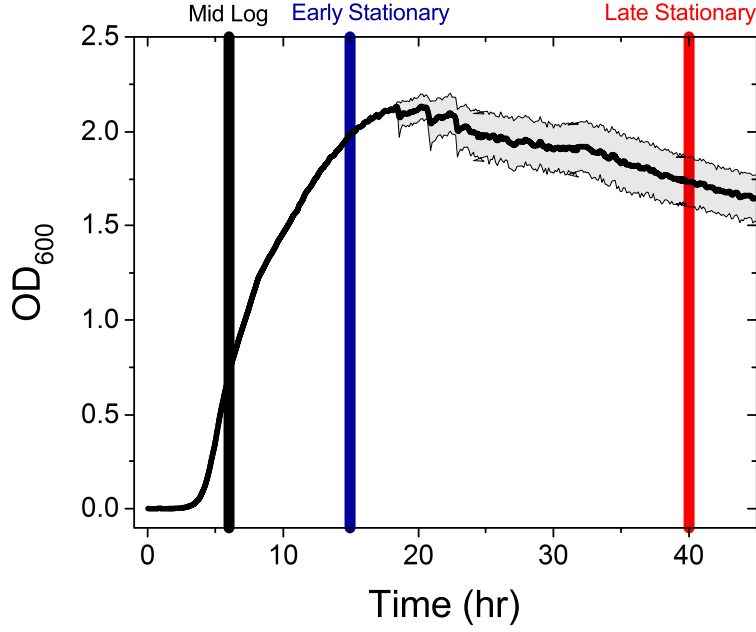
Supplementary Figure 1: (A) Measurements taken of the same sample in five different spectrophotometers. Different spectrophotometers of the same make give the same OD reading, while those produced by different companies measure OD that varies significantly. (B) Calibration performed for spectrophotometers used to obtain growth curves in this work. Calibration was performed using the same plate prepared with a culture of *E. coli* grown to mid-log phase in LB with dilutions as in main text. We report dilution on the x axis to remove uncertainty in determining real concentration. The BMG spectrophotometer provides a path length correction for the Beer-Lambert law (BLL) by default, correcting the OD to that which would be observed by a 1 cm deep well assuming pure absorbance measurements. All *E. coli* measurements were performed in the BMG Spectrostar Omega with path length correction on (red) and yeast measurements were performed in a Tecan Fluorescent spectrophotometer (blue). Conversion factors between the Tecan and BMG were calculated from the data as 1.74 ± 0.02 and 2.75 ± 0.03 for non corrected and corrected readings respectively (*Methods: OD measurements*).



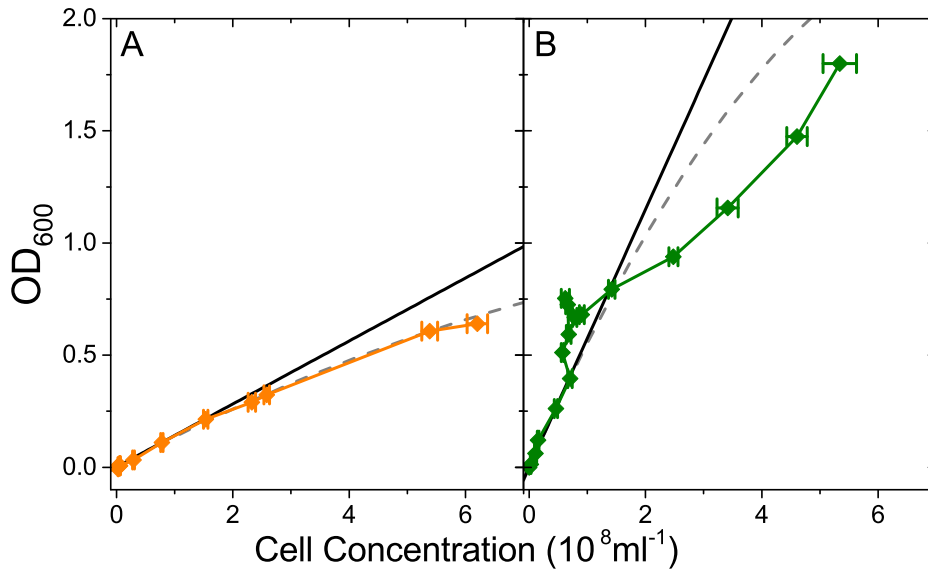
Supplementary Figure 2: OD measurements of *E. coli* samples of different concentrations using different wavelengths. BW25113 Keio collection parent strain was used for this purpose. High concentrations (dark) to low concentrations (light) are indicated with the gradient scale. High concentrations are seen to increase in OD as λ decreases showing the nonlinear dependence of λ on OD. OD measurements on cell expressing fluorescent proteins should include careful choice of wavelength, as absorption caused by the presence of fluorescent proteins can lead to overestimate of cell concentration [1].



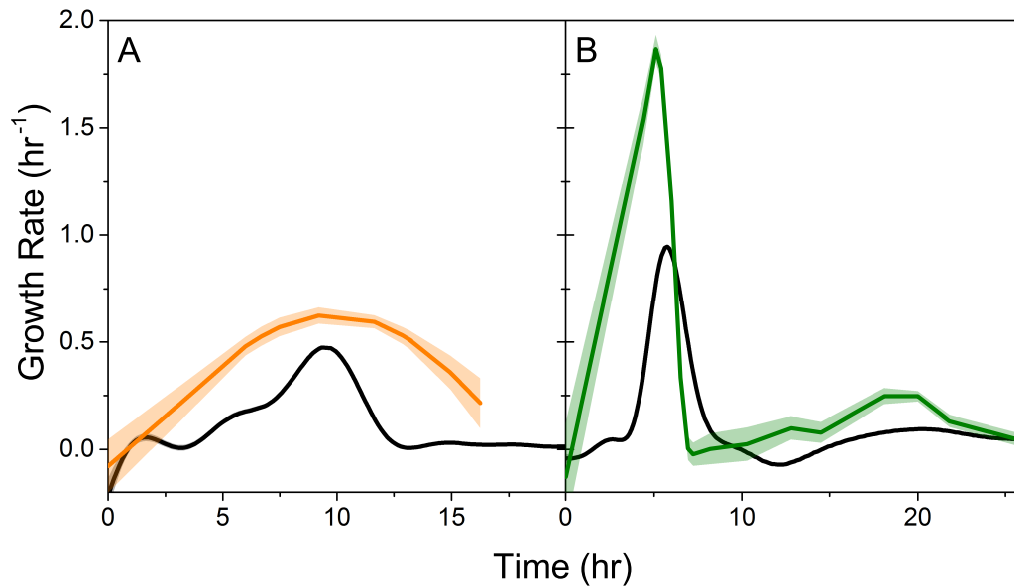
Supplementary Figure 3: Selected brightfield images of beads used in Figure 2. A: $15.7 \pm 1.4 \mu\text{m}$ B: $10.0 \pm 0.6 \mu\text{m}$ C: $3.00 \pm 0.07 \mu\text{m}$ D: $0.96 \pm 0.07 \mu\text{m}$ and E: $0.51 \pm 0.01 \mu\text{m}$. Scale bar given in E applies to A-E.



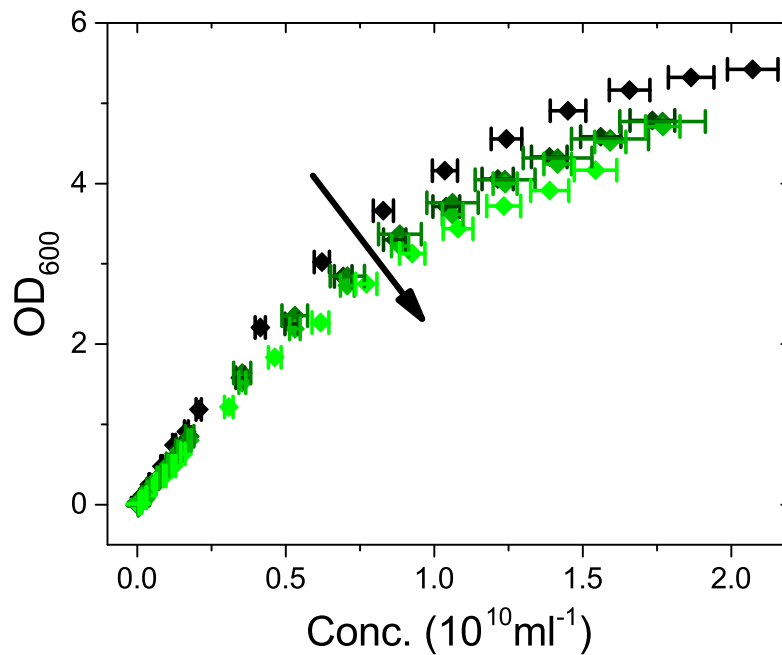
Supplementary Figure 4: Growth curve of *E. coli* sample grown in LB from which the calibration curves for Figure 3 were taken. Mean (black) growth and standard error (grey) was calculated from 10 wells of 300 μl . Cultures of mid log (black), early stationary (blue) and late stationary (red) bacteria were removed at times indicated by the respective vertical lines.



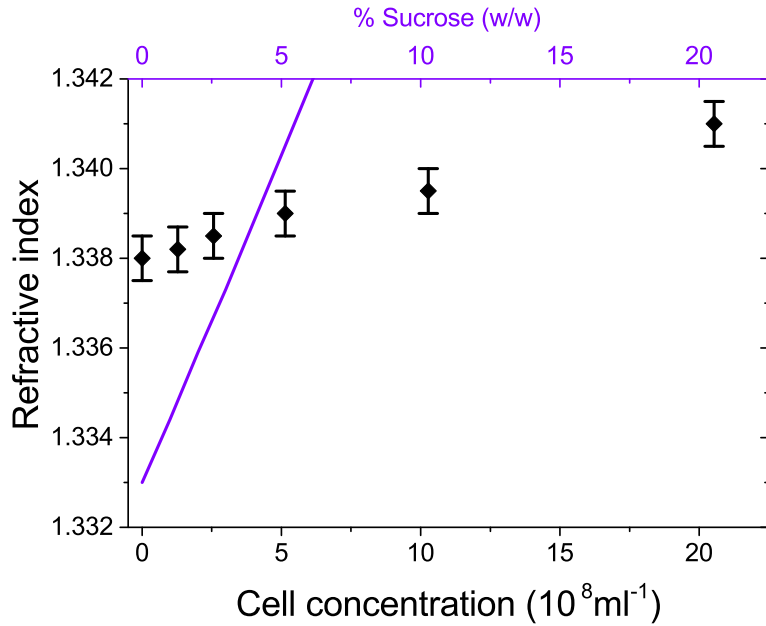
Supplementary Figure 5: C vs OD for growth conditions in Figure 4A and C. Solid and dashed lines represent linear and second degree polynomials fitted to the data (see *Methods* according to the Beer-Lambert Law and scattering theory prediction by Koch [2] respectively). The MM9 (orange) calibration is a parabola as expected [2] (with the exception of the last point obtained when cells started to change size to smaller), however LB+amp (green) calibration shows significant and nontrivial deviation.



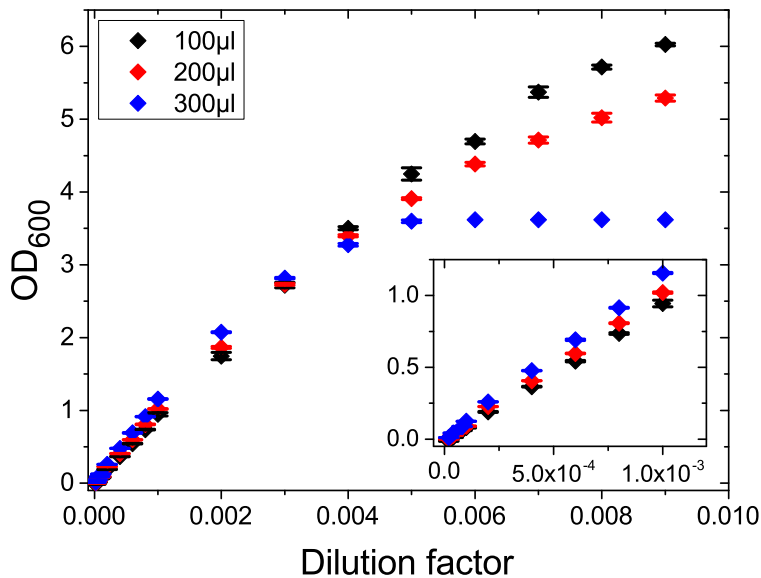
Supplementary Figure 6: Growth rates of *E. coli* were calculated from time derivatives [3] for (A) glucose only media and (B) LB supplemented with $9 \mu\text{g ml}^{-1}$ Ampicillin. Growth rates are calculated from both the OD_{600} growth curve (black) and the cell concentrations (Orange and Green) presented in Figure 4A and C in the main text. The small difference between maximum growth rate obtained from OD and C seen in (A) results from smaller number of time points obtained for C .



Supplementary Figure 7: Bead concentrations plotted against the resultant OD for $1.0 \mu\text{m}$ beads in the presence of sucrose. The index of each trace is $n_m = 1.333; 1.339; 1.344; 1.353$ and 1.368 respectively, with increasing brightness of green representing a higher refractive index of media (n_m). Arrow indicates increasing refractive index of media.



Supplementary Figure 8: Variation in refractive index of LB media as a function of the concentration of lysed *E. coli* cells present. Cell concentrations are measured as outlined in *Methods* before being lysed and added to LB. n_m varies only slightly, even at the highest fractions of intracellular material. In contrast, adding sucrose to ddH₂O (purple) produces a far larger variation in n_m .



Supplementary Figure 9: OD measurements of 1 μm beads of known concentrations and volumes of 100 μl , 200 μl and 300 μl performed in the BMG Spectrostar spectrophotometer used in this paper. The volume of solution occupies $\frac{1}{3}\times$, $\frac{2}{3}\times$ and $1\times$ the total volume of a single well respectively. The BMG Spectrostar corrects the measured OD using a built in path length correction based on the Beer-Lambert law. However, the measurements for the three volumes do not overlay one another as would be predicted by Beer-Lambert law. The difference between volumes of solution is large for high values of OD, but is also present at $\text{OD} < 1$ as shown in the inset, with the OD of the fully occupied well being higher than those partially filled [4].

Supplementary Table 1: Scattering approximations and their dependency on the radius of the scatterer (r), wavelength of incident light (λ) and refractive indices of the scatterer and the media (n_p and n_m) respectively. n is the relative refractive index between the scatterer and the medium ($\frac{n_p}{n_m}$). Abbreviations: Scatt.: scatterer, sph.: spheres, arb.: arbitrary geometry.

Approx.	Scatt.	Regime	Dependence on N , λ , n and r	
Rayleigh	sph.	$r \ll \lambda$; $\frac{n_p}{n_m} r \ll \lambda$	$\left(\frac{n_p}{n_m}\right)^4 \frac{Nr^6}{\lambda^2}$	[5]
Rayleigh-Gans-Debye	rods	$ \frac{n_p}{n_m} - 1 \ll 1$; $r \frac{n_p}{n_s} - 1 \ll \lambda$	$\left(\frac{n_p}{n_m}\right)^4 \frac{Nr^2}{\lambda^2}$	[5]
Jöbst	sph.	$\frac{2\pi r}{\lambda} \gg 1$; $r \gg \frac{\lambda}{\lambda^2}$	$\left(\frac{n_p}{n_m}\right)^4 \frac{Nr^4}{\lambda^2}$	[6]
van de Hulst (Anomalous Diffraction)	arb.	$ \left(\frac{n_p}{n_m}\right)^2 - 1 \ll 1$; $2\pi r \gg \lambda$	$\frac{N\lambda}{r\left(\frac{n_p}{n_m}\right)^2} \sin\left(\frac{r}{\lambda}\left(\frac{n_p}{n_m}\right)^2\right) + \frac{N\lambda^2}{r} \frac{[1 - \cos(\frac{r}{\lambda}\left(\frac{n_p}{n_m}\right)^2)]}{\left(\frac{n_p}{n_m}\right)^2}$	[7]
Mie	sph.	$r \gg \lambda$	$N\left[\frac{\lambda}{r^2} + \frac{\lambda}{r^2}\left(\frac{n_p}{n_m}\right)^4\right]$	[6]
Hart-Montroll	sph.	$1 < \left(\frac{n_p}{n_m}\right)^2 < 1.5$ $0.25\lambda < \pi r < 3\lambda$	$\frac{Nr^2}{\lambda^2} \frac{[\left(\frac{n_p}{n_m}\right)^2 - 1]^2}{\left(\frac{n_p}{n_m}\right)^2} \left[\left(\frac{n_p}{n_m}\right)^8 + \left(\frac{n_p}{n_m}\right)^4 \left(\frac{\lambda}{r}\right)^2 + \left(\frac{\lambda}{r}\right)^4\right]$	[6, 8]
Perelman	arb.	$ \left(\frac{n_p}{n_m}\right)^2 - 1 \ll 1$ $2\pi r \gg \lambda$	$N \frac{n_p}{n_m} \left(\frac{r}{\lambda}\right)^5 \left(\left(\frac{n_p}{n_m}\right)^4 - 1\right)^2$	[6]
Evans-Fournier	arb.	$ \frac{n_p}{n_m} < 1$ any r, λ	$N\left(\frac{r}{\lambda} + \frac{r^3}{\lambda^3} + \frac{r^5}{\lambda^5}\right) \left[\left(\frac{\frac{r}{\lambda} + \frac{r^3}{\lambda^3} + \frac{r^5}{\lambda^5}}{\left(\frac{r}{\lambda}\left(\frac{n_p}{n_m}\right)^2 \sin\left(\frac{r}{\lambda}\left(\frac{n_p}{n_m}\right)^2\right) + \left(\frac{r}{\lambda}\right)^2 \frac{\cos\left(\frac{r}{\lambda}\left(\frac{n_p}{n_m}\right)^2\right)}{\left(\frac{n_p}{n_m}\right)^2}\right)}\right)^{\frac{\lambda}{r}}\right]^{-\frac{r}{\lambda}}$	[6, 9]
Eikonal	arb.	$ \left(\frac{n_p}{n_m}\right)^2 - 1 \ll 1$ $2\pi r \gg \lambda$	$N\left(\frac{\lambda}{r}\right)^2 \left(\frac{\cos(\arctan(\left(\frac{n_m}{n_p}\right)^2))}{\left(\frac{n_p}{n_m}\right)^2}\right)^2 \left[\cos\left(\left(\frac{n_m}{n_p}\right)^2\right) - \cos\left\{\frac{r}{\lambda}\left(\frac{n_p}{n_m}\right)^4\right\} - \arctan\left[\left(\frac{n_m}{n_p}\right)^2\right] \exp\left\{-\frac{\left(\frac{n_p}{n_m}\right)^2 r}{\lambda}\right\}\right] - \frac{N\lambda}{r\left(\frac{n_p}{n_m}\right)^4} \cos\left[\arctan\left(\frac{n_m}{n_p}\right)^2 \sin\left(\frac{r}{\lambda}\left(\frac{n_p}{n_m}\right)^4\right)\right] - N \arctan\left(\left(\frac{n_m}{n_p}\right)^2\right) \exp\left\{-\frac{\left(\frac{n_p}{n_m}\right)^4 r}{\lambda}\right\}$	[6, 10]

Supplementary Table 2: Selection of refractive indexes collated from different literature sources. Mostly bacteria and yeast are given, but we also include some other biological samples for completeness.

Bacteria	Refractive index	Conditions	
<i>E. coli</i>	1.3324	$\lambda = 600$ nm	[11]
	1.382	minimal absorbance method	[12]
	1.387	immersive refractometry	[12]
	1.388	index matching	[13]
	1.395	$\lambda = 589$ nm	[14]
	1.397	$\lambda = 589$ nm	[15]
	1.406 ± 0.003	$\lambda = 589$ nm	[16]
<i>E. coli</i> DH1	1.382	$\lambda = 350$ nm	[17]
<i>E. coli</i> cytoplasm	1.390	immersive refractometry	[12]
<i>E. coli</i> cytoplasm and nucleoid	1.382	immersive refractometry	[12]
<i>E. coli</i> nucleoid	1.371	immersive refractometry	[12]
<i>E. coli</i> cell wall	1.4	$\lambda = 520$ nm	[18]
<i>E. coli</i> protoplast	1.35	$\lambda = 520$ nm	[18]
<i>Bacillus cereus</i>	1.386	$\lambda = 520$ nm	[18]
	1.3865	$\lambda = 542$ nm	[19]

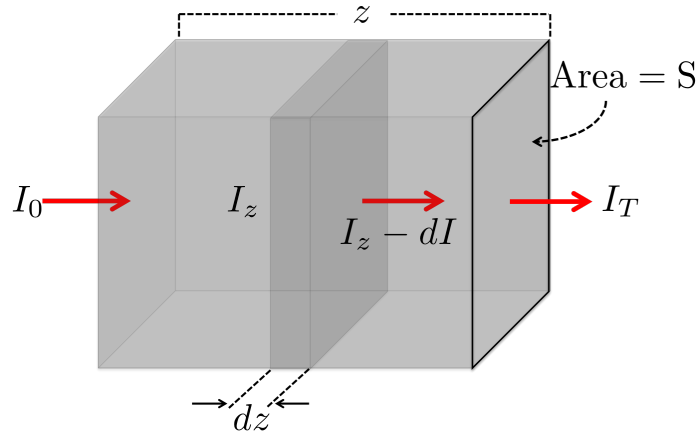
<i>B. cereus</i> var. <i>mycoides</i>	1.4000	$\lambda = 542$ nm	[19]
<i>B. cereus</i> spores	1.521	$\lambda = 542$ nm	[19]
<i>B. cereus</i> var. <i>mycoides</i> spores	1.528	$\lambda = 542$ nm	[19]
<i>B. megaterium</i>	1.3880	$\lambda = 542$ nm	[19]
<i>B. megaterium</i> spores	1.537	$\lambda = 542$ nm	[19]
<i>B. subtilis</i>	1.446	index matching	[13]
<i>C. oligotrophus</i>	1.365	$\lambda = 350$ nm	[17]
	1.371	minimal absorbance method	[17]
<i>Lactobacillus bulgaricus</i>	1.404	$\lambda = 589$ nm	[20]
<i>Marinobacter articus</i>	1.371	$\lambda = 350$ nm	[17]
<i>Micrococcus lysodeikticus</i>	1.399	$\lambda = 589$ nm	[16]
<i>Proteus vulgaris</i>	1.385	immersive refractometry	[21]
<i>Sarcina lutea</i>	1.396	immersive refractometry	[21]
<i>Serratia marcescens</i>	1.387 ± 0.001	$\lambda = 589$ nm	[16]
<i>Staphylococcus aureus</i>	1.413 ± 0.002	$\lambda = 546$ nm	[16]
<i>Streptococcus haemolyticus</i>	1.392	immersive refractometry	[21]
<i>Streptococcus faecalis</i>	1.37	immersive refractometry	[22]
Other			
Yeast - nucleus	1.36-1.39	$\lambda = 633$ nm	[23]
Yeast - cell wall	1.53	Theoretical calculation	[24]
Lipid	1.50	approximate as oil	[25]
Mitochondria	1.40	$\lambda = 632.8$ nm	[26]
Mitochondrion - resting	1.43	theoretical calculation	[27]
Mitochondrion - respiring	1.50	membrane and matrix	[27]
	1.35	intramembrane	[27]
Microtubules	1.512	index matching	[28]
HeLa Cells	1.33-1.39	$\lambda = 633$ nm	[23]
	1.385 ± 0.001	$\lambda = 632.8$ nm	[29]
	1.3716 ± 0.0035	$\lambda = 632.8$ nm	[30]
HeLa - nuclei	1.3554 ± 0.0031	$\lambda = 632.8$ nm	[30]
	1.3528 ± 0.0035	mechanically isolated	[30]
HL60 (Human myelocytic Leukemia Cells)	1.3776 ± 0.0046	$\lambda = 632.8$ nm	[30]
HL60 - nuclei	1.3582 ± 0.0030	$\lambda = 632.8$ nm	[30]
Jurkat (leukemic T-cells)	1.3671 ± 0.0052	$\lambda = 632.8$ nm	[30]
Jurkat - nuclei	1.3610 ± 0.0037	$\lambda = 632.8$ nm	[30]
MCF7 (Human breast cancer cells)	1.3713 ± 0.0048	$\lambda = 632.8$ nm	[30]
MCF7 - nuclei	1.3554 ± 0.0031	$\lambda = 632.8$ nm	[30]
Human plasma proteins	1.60	$\lambda = 589.3$ nm	[31]
Plasma β -lipoprotein	1.514	$\lambda = 589.3$ nm	[31]
Human ribonuclease	1.630	index matching	[32]
Human β -lactoglobulin	1.594	index matching	[32]
Human Pepsin	1.603	index matching	[32]

Supplementary Table 3: Refractive index of solutions containing components that may be released during growth (particularly when grown under sublethal antibiotic or any other stress concentrations) as measured by a refractometer. The maximum concentration of extracellular DNA that could be released during normal growth is estimated to be $7.45 \mu\text{g ml}^{-1}$ given by: concentration of cells \times size of chromosome \times mass of base pair / Avogadro's constant. Assuming lysis of all cells from the maximum cell concentration observed during our experiments the concentration can be calculated as: $1.5 \times 10^9 \text{ml}^{-1} \times 4.6 \text{M bases} \times 650 / 6.02 \times 10^{23}$. The small difference between the refractive index of H_2O and extracellular bacterial DNA is negligible meaning bacterial cell lysis will not noticeably effect the calibration curve.

Solution	Refractive index
H_2O	1.335
$802.8 \mu\text{g ml}^{-1}$ 23-mer primer DNA	1.335
$1099.4 \mu\text{g ml}^{-1}$ 23-mer primer DNA	1.336
LB medium	1.338
Cell Lysate (grown in LB then sonicated)	1.341

Supplementary Table 4: 2nd degree polynomial fit parameters obtained using the curve fitting tools available in the Matlab environment [33]. For each sample, the equation was solved for OD = 0.05, 0.1, 0.5, 1 and 10 and plotted in Figure 2C.

Sample	Equation	R-squared
15 μm beads	$4.21 \times 10^9 \text{OD}^2 + 1.63 \times 10^{11} \text{OD} + 7.64 \times 10^9$	0.995105
10 μm beads	$4.17 \times 10^8 \text{OD}^2 + 4.17 \times 10^8 \text{OD} + 2.62 \times 10^8$	0.988257
3.0 μm beads	$1.80 \times 10^6 \text{OD}^2 + 1.52 \times 10^7 \text{OD} + 6.60 \times 10^6$	0.972179
1.0 μm beads	$8.82 \times 10^5 \text{OD}^2 + 1.19 \times 10^6 \text{OD} + 1.28 \times 10^6$	0.981168
0.5 μm beads	$2.05 \times 10^5 \text{OD}^2 + 4.70 \times 10^5 \text{OD} + 2.35 \times 10^5$	0.991838



Supplementary Figure 10: Schematic outlining parameters used in the derivation of the Beer-Lambert Law (BLL). A beam of intensity I_0 enters the sample perpendicular to area, S . As the sample passes through a thin slice of the sample (dz) the intensity has reduced from I_z to $I_z - dz$ and having passed through the length of the sample (z) the intensity has reduced to the transmitted intensity (I_T).

Supplementary Note 1: Beer-Lambert law derivation

Consider a beam of parallel, monochromatic light with intensity I_0 striking a sample of area, S perpendicular to the surface (Supplementary Fig. 10). The light travels through the sample to a depth of z , after which the intensity is reduced to I_T . An infinitesimally thin slice of the sample, dz contains M molecules, such that

$$M = CSdz \quad (1)$$

where C is the number of molecules per unit volume. Each molecule has a cross-section σ meaning that the fraction of light absorbed due to a single molecule of area s is $\frac{\sigma}{s}$. Therefore, the total cross-sectional area from all the molecules in the block is given by

$$CSdz \frac{\sigma}{s} = C\sigma dz \quad (2)$$

If we compare the intensity of light entering this thin slice (I_z) with the intensity of light that exits ($I_z - dI_z$) we find the fraction of absorbed light I_a is

$$I_a = \frac{dI_z}{I_z} \quad (3)$$

The sum of I_a through all the slices of the sample is proportional to the sum of all cross-sectional areas for all molecules in all the thin slices (Eq. 2). Integrating Eq. 3 we have:

$$\int_{I_0}^{I_T} \frac{dI_z}{I_z} = - \int_0^Z C\sigma dz \quad (4)$$

which can be rewritten in its common form as the Beer-Lambert law (BLL)

$$\ln \left(\frac{I_0}{I_T} \right) = C\sigma Z \quad (5)$$

When BLL is applied to OD measurements σ is the cross-section of the bacterium; z the distance the light travels through the sample, I_0 , the intensity of light incident on the sample and I_T is the intensity of light transmitted through the sample and related to the OD through the expression:

$$\text{OD} = C\sigma Z - \log(I_0) \quad (6)$$

Supplementary Note 2: Multiple Scattering considerations

As the concentration of bacteria increases, the possibility of multiple scattering, where light is scattered off more than one bacterium, increases due to the closer packing of the bacteria within the sample (Figure 1B, main text). Subsequently, these multiple scattering events start to contribute significantly to the measured intensity of light at the detector.

For particles larger or comparable to the wavelength of radiation a correction factor for multiple scattering events can be added to the BLL using the small-angle approximation. This takes the form of correction factor CF [34–41]

$$CF(z, \sigma) = \sum_{m=1}^{\infty} \frac{(\frac{\sqrt{2}}{w_0}z)^m}{m!} \frac{1 - S(m)}{1 - \exp \left[-\frac{w_0 r}{\sqrt{2}} r_d^2 \right]} \quad (7)$$

where m is the number of scattering events the light has undergone and $m_{max} = \infty$, r the radius of the scatterer, w_0 the beam width of incident light, z the distance between the light source and detector, r_d is the distance between the two scattering events and $S(m)$ is the integral over all particles and scattering events that occur before the light enters the detector and is defined as

$$S(m) = \int_0^1 \dots \int_0^1 ds_1 \dots ds_m \exp \left[\frac{-\frac{\sqrt{2}}{w_0} r_d^2}{1 + \frac{\sqrt{2}}{\alpha} z^2 \sum_{i=1}^m s_i^2} \right] \quad (8)$$

where α is the polarisation of the scattered light and s_m is the number of scatterers the light interacts with [34–41]. CF increases the power measured at the detector when multiple scattering occurs.

The inclusion of the above corrections allows calculation of the effect multiple scattering events have on the intensity of light on the detector (I_D), but with limitations and at a cost.

$CF(z, \sigma)$ is nonlinear with N , since CF is obtained by integrating over the area of each individual scatterer (s_m), an increase in N will lead to a reduction in r_d and increased probability of m increasing. Initially, as N increases $CF(z, \sigma)$ also increases. But, for multiple scattering events where a single light beam is scattered many times, $CF(z, \sigma) \rightarrow 0$. In this regime N is so large that all light entering the sample is constrained by photon diffusion and no light is directly transmitted to the detector. Consequently, $I_D \rightarrow 0$ meaning that OD becomes very large. In the case of low density samples, CF reduces to single scattering theory and the BLL holds. In the multiple scattering regime CF is significant and has been shown to increase I_D by 50% for particulates in fog at the small value of $m = 2$. [41]

However, in order to apply the correction factor to OD measurements it is necessary for the user to know both m and N . Thus, in order to measure N accurately using a spectrophotometer, N needs to be accurately determined by another method. Furthermore, since the forward scattering contribution to the power incident on the detector is highly dependent upon the geometry of the scatterer as well as the density and absorption; the degrees of freedom within the system require calibration of the OD vs cell number measurements independently.

Other considerations

In the above calculations we have made two assumptions that should be noted, the sample is static over the time period of a measurement and the sample is not heterogenous in geometry.

Static vs Dynamic

Unlike dust particles, crystal structures, water droplets or colloidal solutions, for which many of these approximations were originally derived, bacteria are motile. Dynamic samples can add additional complexity to solutions of scattering (see [42] for a recent discussion or [43] for a more rigorous review). Often, OD measurements are conducted in rich growth media (LB or defined rich media like EZ Rich [44]) where samples are not nutrient limited leading to reduced production of flagella and therefore limited motility. In this case it is safe to assume that samples undergo only diffusion during measurement of I_D . However, if the growth conditions deviate from optimal, the bacteria become motile [45]. To estimate the effect on motility we take the case of *E. coli* and previously reported swimming speed of 20 $\mu\text{m}/\text{sec}$ [46]. At this speed *E. coli* will only have traveled 0.2 μm (or less than half the body length) in the time it takes a 50 Hz platerreader to acquire a single OD measurement, and we can still assume a static sample. However, the effect of swimming should be re-evaluated for cases where it might play a more significant role, for example smaller and faster bacteria.

Heterogeneity of the geometry

The effect of heterogeneity of a sample can be discounted for samples with dimensions $D \gg \lambda$ (e.g. yeast), however we have shown that it is more important in bacterial cultures where $D \approx \lambda$. In conditions where heterogeneity in bacterial geometry does not change throughout the growth cycle of the culture it is sufficient to perform one calibration curve (Fig. 3). But, in cases where the heterogeneity of the sample does change, even if the bacteria sizes do not (for example bigger and smaller bacteria are present where the ratio of the two changes through the growth cycle), OD is no longer suitable for estimated of bacterial number density and direct counting should be performed.

Volume of sample in the well

There is a positive correlation between the volume of sample through which light travels and the probability of multiple scattering events occurring that is not necessarily in accordance with the BLL. In order to determine the effect of differences in the volume size on the calibration, we measured OD

for solutions of 1 μm diameter beads at known dilutions from manufacturer concentration 1.8×10^{11} ml^{-1} for 100 μl , 200 μl and 300 μl volumes of solution in a plate reader well (Supplementary Fig. 9).

The maximum volume of solution (300 μl) corresponds to the maximum volume the plate reader well can hold ($l = z$), meaning the smaller volumes correspond to $z/3$ and $2z/3$ respectively. The BMG Spectrostar spectrophotometer performs path-length correction to the measurements by applying the BLL approximation. For cases where the BLL is satisfied, the measured calibration curves for varying l would collapse to a single line. Supplementary Figure 9 shows that, unlike for absorbance measurements, for turbidity measurements this is not the case. Instead, variation in l leads to significant deviation between the three lines as the concentration of the solution increases. Deviation at high concentrations is as expected, with OD saturating quickest for $l = z$. At low fractions of manufacturer concentration, the three curves still do not fully collapse to a single line (inset) with OD being higher for $l = z$ compared to $l = \frac{z}{3}$ and $l = \frac{2z}{3}$. While this effect is pronounced, for most plate reader experiments, it can be neglected provided the volume of the sample in each well is kept the same and that the volume does not change significantly throughout the duration of the experiment (e.g. evaporation of the solution is prevented or minimized).

OD at transitions between different scattering regimes

To best determine the limits of the single, multiple and photon diffusion scattering regimes, it is useful to consider the fraction of the total volume of the culture occupied by scatterers (ρ) rather than C , and several previous studies have evaluated the applicability of different scattering theories with respect to ρ [47–50]. From these, single scattering theory is applicable for volume fractions of $\rho \leq 0.001$ [49,50], the multiple scattering regime is satisfied for $0.001 \leq \rho \leq 0.2$ [47,49] and for higher values ($\rho > 0.2$), photon diffusion limit is reached where statistical approaches are best suited [47–50].

References

- [1] A. Hecht, D. Endy, M. Salit, and M. S Munson. When wavelengths collide: Bias in cell abundance measurements due to expressed fluorescent proteins. *ACS Synth Biol*, 5:1024–1027.
- [2] Albert L Koch. Some Calculations on the Turbidity of Mitochondria and Bacteria. *Biochimica et biophysica acta*, 51:429–441, 1961.
- [3] P. S. Swain, K. Stevenson, A. Leary, L. F. Montano-Gutierrez, I. B. N. Clark, J. Vogel, and T Pilizota. Inferring time-derivatives, including cell growth rates, using gaussian processes. *BioRxiv*, 2016.
- [4] Akira Ishimaru and Yasuo Kuga. Attenuation constant of a coherent field in a dense distribution of particles. *Journal of the Optical Society of America*, 72(10):1317, 1982.
- [5] Lord Rayleigh. On the scattering of light by small particles. *Philosophical Magazine*, 41(4):447–454, 1871.
- [6] Subodh K. Sharma and David J. Sommerford. *Light scattering by optically soft particles*, volume 1 of *Springer Praxis Books*. Springer Berlin Heidelberg, Cambridge, 2006.
- [7] H C Van De Hulst. *Light scattering by small particles*, volume 1. Dover Publications, New York, 1981.
- [8] S. K. Sharma and D. J. Somerford. Relationship between the S approximation and the Hart-Montroll approximation. *Journal of the Optical Society of America A*, 13(6):1285, 1996.
- [9] B T Evans and G R Fournier. Simple approximation to extinction efficiency valid over all size parameters. *Applied optics*, 29(31):4666–4670, 1990.
- [10] S.K. Sharma and D.J. Somerford. *Scattering of Light in the Eikonal Approximation*, volume 39 of *Progress in Optics*. Elsevier, London, 1999.

- [11] Aleksei E. Balaev, K. N. Dvoretzki, and Valeri A. Doubrovski. Refractive index of *Escherichia coli* cells. In *SPIE 4707, Saratov Fall Meeting 2001: Optical Technologies in Biophysics and Medicine III*, pages 253–260, 2002.
- [12] J. A C Valkenburg and C. L. Woldringh. Phase separation between nucleoid and cytoplasm in *Escherichia coli* as defined by immersive refractometry. *Journal of Bacteriology*, 160(3):1151–1157, 1984.
- [13] P. Y. Liu, L. K. Chin, W. Ser, T. C. Ayi, P. H. Yap, T. Bourouina, and Y. Leprince-Wang. Real-Time measurement of single bacterium’s refractive index using optofluidic immersion refractometry. *Procedia Engineering*, 87:356–359, 2014.
- [14] F D Bryant, B a Seiber, and P Latimer. Absolute optical cross sections of cells and chloroplasts. *Archives of biochemistry and biophysics*, 135(1):97–108, 1969.
- [15] Aleksei E. Balaev, Konstanten N. Dvoretzki, and Valeri A. Doubrovski. Determination of refractive index of rod-shaped bacteria from spectral extinction measurements. In Valery V. Tuchin, editor, *Saratov Fall Meeting 2002: Optical Technologies in Biophysics and Medicine IV*, pages 375–380, 2003.
- [16] J. B. Bateman, Jack Wagman, and E. L. Carstensen. Refraction and absorption of light in bacterial suspensions. *Kolloid-Zeitschrift & Zeitschrift für Polymere*, 208(1):44–58, 1966.
- [17] B. R. Robertson, D. K. Button, and A. L. Koch. Determination of the biomasses of small bacteria at low concentrations in a mixture of species with forward light scatter measurements by flow cytometry. *Applied and Environmental Microbiology*, 64(10):3900–3909, 1998.
- [18] P J Wyatt. Differential light scattering: A physical method for identifying living bacterial cells. *Applied Optics*, 7(10):1879–1896, 1968.
- [19] K F Ross and E Billing. The water and solid content of living bacterial spores and vegetative cells as indicated by refractive index measurements. *Journal of General Microbiology*, 16(2):418–25, 1957.
- [20] K F A Ross. The size of living bacteria. *Quarterly Journal of Microscopical Science*, s3-98:435–454, 1957.
- [21] R. Barer, K. F. A. Ross, and S. Tkaczyk. Refractometry of living cells. *Nature*, 171(4356):720–724, 1953.
- [22] L. Daneo-Moore, D. Dicker, and M. L. Higgins. Structure of the nucleoid in cells of *Streptococcus faecalis*. *Journal of Bacteriology*, 141(2):928–937, 1980.
- [23] Wonshik Choi, Christopher Fang-Yen, Seungeun Oh, Niyom Lue, Ramachandra R Dasari, Michael S. Feld, and Kamran Badizadegan. Tomographic phase microscopy. Quantitative imaging of living cells. *BIOforum Europe*, 10(c):2–3, 2007.
- [24] R.D. Chaudhari, J.D. Stenson, T.W. Overton, and C.R. Thomas. Effect of bud scars on the mechanical properties of *Saccharomyces cerevisiae* cell walls. *Chemical Engineering Science*, 84:188–196, 2012.
- [25] L Sacconi, I M Tolic-Nørrelykke, M D’Amico, F Vanzi, M Olivotto, R Antolini, and F S Pavone. Cell imaging and manipulation by nonlinear optical microscopy. *Cell biochemistry and biophysics*, 45(3):289–302, 2006.
- [26] Michael Taylor. *Quantum microscopy of biological systems*. Springer Theses. Springer International Publishing, Cham, 2015.
- [27] Roland Thar and Michael Köhl. Propagation of electromagnetic radiation in mitochondria? *Journal of Theoretical Biology*, 230(2):261–270, 2004.

- [28] Hidemi Sato, Gordon W Ellis, and Shinya Inoui. Microtubular origin of mitotic spindle form birefringence. Demonstration of the Applicability of Wiener ' s Equation. *The Journal of Cell Biology*, 67:501–517, 1975.
- [29] J Beuthan, O Minet, J Helfmann, M Herrig, and G Müller. The spatial variation of the refractive index in biological cells. *Physics in Medicine and Biology*, 41(3):369–382, 1996.
- [30] Mirjam Schürmann, Jana Scholze, Paul Müller, Jochen Guck, and Chii J. Chan. Cell nuclei have lower refractive index and mass density than cytoplasm. *Journal of Biophotonics*, 9:1–9, 2016.
- [31] S. H. Armstrong, M. J. E. Budka, K. C. Morrison, and M Hasson. Preparation and properties of serum and plasma proteins. XII. The refractive properties of the proteins of human plasma and certain purified fractions 1,2. *Journal of the American Chemical Society*, 69(7):1747–1753, 1947.
- [32] Thomas L. McMeekin, Mildred Wilensky, and Merton L. Groves. Refractive indices of proteins in relation to amino acid composition and specific volume. *Biochemical and Biophysical Research Communications*, 7(2):151–156, 1962.
- [33] The MathWorks Inc. Matlab and statistics toolbox release, MATLAB version 7.10.0 (R2010a). 2010.
- [34] Andrew Zardecki. Multiple scattering corrections to the Beer-Lambert law. In John C. Leader, editor, *SPIE 0410, Laser Beam Propagation in the Atmosphere*, pages 103–110, Arlington, 1983.
- [35] A. Zardecki and W G Tam. Multiple scattering corrections to the Beer-Lambert law. 2: Detector with a variable field of view. *Applied Optics*, 21(13):2413–20, 1982.
- [36] A. Zardecki and W G Tam. Iterative method for treating multiple scattering in fogs. *Canadian Journal of Physics*, 57(9):1301–1308, 1979.
- [37] Andrew Zardecki and Siegfried A W Gerstl. Multi-Gaussian phase function model for off-axis laser beam scattering. *Applied Optics*, 26(15):3000, 1987.
- [38] W G Tam and A Zardecki. Multiple scattering of a laser beam by radiational and advective fogs. *Opt. Acta*, 26(5):659–670, 1979.
- [39] W. G. Tam and A. Zardecki. Laser beam propagation in particulate media. *Journal of the Optical Society of America*, 69(1):68, 1979.
- [40] W. G. Tam. Multiple scattering corrections for atmospheric aerosol extinction measurements. *Applied Optics*, 19(13):2090, 1980.
- [41] W. G. Tam and Andrew Zardecki. Multiple scattering corrections to the Beer-Lambert law 1: Open detector. *Applied Optics*, 21(13):2405, 1982.
- [42] Achim M. Loske, Elba M. Tello, Susana Vargas, and Rogelio Rodriguez. *Escherichia coli* viability determination using dynamic light scattering: A comparison with standard methods. *Archives of Microbiology*, 196(8):557–563, 2014.
- [43] S E Harding. Applications of light scattering in microbiology. *Biotechnology and Applied Biochemistry*, 8(6):489–509, 1986.
- [44] Frederick C Neidhardt, Philip L Bloch, and David F Smith. Culture medium for enterobacteria. *J Bacteriol*, 119(3):736–747, 1974.
- [45] J Adler and Bonnie Templeton. The effect of environmental conditions on the motility of *Escherichia coli*. *Journal of General Microbiology*, 46(2):175–184, 1967.
- [46] Jana Schwarz-Linek, Jochen Arlt, Alys Jepson, Angela Dawson, Teun Vissers, Dario Miroli, Teuta Pilizota, Vincent A. Martinez, and Wilson C K Poon. *Escherichia coli* as a model active colloid: A practical introduction. *Colloids and Surfaces B: Biointerfaces*, 137:2–16, 2016.

- [47] Giovanni Zaccanti, Samuele Del Bianco, and Fabrizio Martelli. Measurements of optical properties of high-density media. *Applied Optics*, 42(19):4023–4030, 2003.
- [48] G Göbel, J Kuhn, and J Fricke. Dependent scattering effects in latex-sphere suspensions and scattering powders. *Waves in Random Media*, 5(4):413–426, 1995.
- [49] Akira Ishimaru. *Wave Propagation and Scattering in Random Media*. IEEE, 1999.
- [50] Arianna Giusto, Rosalba Saija, Maria Antonia Iatì, Paolo Denti, Ferdinando Borghese, and Orazio I Sindoni. Optical properties of high-density dispersions of particles: application to intralipid solutions. *Applied Optics*, 42(21):4375–4380, 2003.

3.3 Neural network for brightfield cell counting

3.3.1 Introduction

Motivation

Given the difficulties in using optical density measurements in the previous chapter, it became evident that we would need to perform calibrations for every condition I test and for each new spectrometer used. In order to help facilitate this process I looked to develop a method to streamline the calibration protocol from the previous chapter. Since the cell counting takes the longest time to perform manually I set out to automate the process.

While I initially attempted to use a simple image analysis program, a number of difficulties emerged as the bacteria would change from bright on dark, to dark on bright as the z-stack progressed. Sometimes both conditions were in the same image and therefore cells would fail to be detected as demonstrated in Fig. 3.9. Any dirt or debris on the microscope or distortion from uneven illumination would cause false identification as well. So I made the decision to construct a more robust image analysis system, that could also be more easily applied across my conditions and potentially even other microscopes.

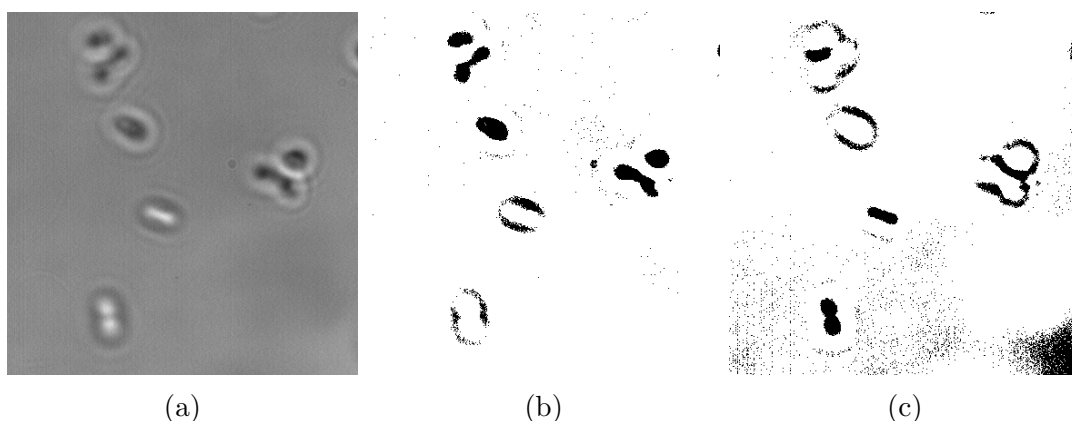


Figure 3.9: a) Example brightfield image under the best conditions: image is cropped to a small area with relatively even illumination and high contrast cells present in field. b) image from (a) using a black threshold. c) image from (a) using a white threshold. Both thresholds were chosen to highlight the largest area of cells with minimal background. Note the false halos present around cells that are not detected due to the diffraction rings from out of focus bacteria and the black region present in the lower right of (c) due to slight imperfections in field illumination. Halos are often the same area as cells, particularly those with their poles presented to the field of focus, and interfere with further processing using tools such as edge or blob finding.

To do so I chose to construct a neural network for the image analysis as they are generally more fault tolerant than deterministic algorithms and can be easily scaled using multi-core computer systems or graphics cards to accelerate the computation time without requiring heavy knowledge of programming.

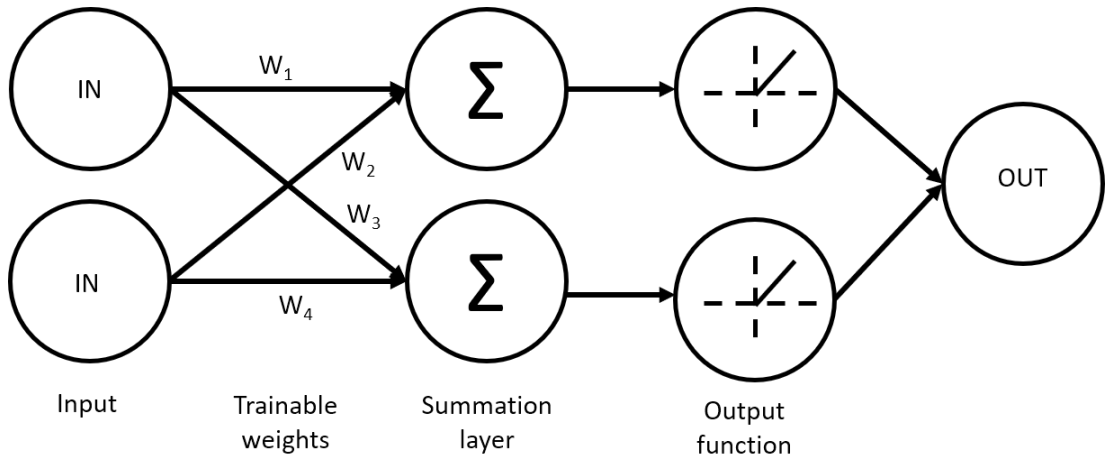


Figure 3.10: A simplified neural network that takes two inputs and produces an output. A single neural node consists of a trainable weight, a sum or multiplication node and an output function. In this case two neural nodes combine the inputs to produce a single output. The weight layers are trained, while the other layers are fixed when defining the structure of the network

Neural networks

A simple neural network is shown in Fig.3.10, which would take two input values and produce a single output. The most common output function for computational neural networks is the ReLU (REctified Linear Unit) output function, where the output is zero for inputs that sum less than zero, and equal to the inputs when greater, allowing for a reduced computational load when running large numbers of nodes at once. Training the network involves inputting data and comparing the output to a known good value before adjusting the weights (W_n) and testing the network again. The network is considered trained and useful when the weights are adjusted so that the input values are converted to the desired output value. Once trained a network can be stored and executed without further modification of the weights, allowing consistent analysis or processing.

For a network architecture I chose to implement the u-net architecture developed by Brox *et al.* [124] in Keras with Tensorflow as a backend [125]. This network allows for a significantly reduced memory consumption and faster computation than the traditional convolutional neural network. Memory consumption is a significant limitation with our data, as the images being processed are 1024 by 1024 pixels wide and composed of 16-bit integers and therefore will consume around 30 MB of memory alone. This is then compounded as the network convolves the image with multiple filters simultaneously and increases the volume of information in memory exponentially.

The final network consists of 70,345 trainable parameters (W values) and 672 fixed parameters.

The learning function, Adam, was chosen based on reports of its well defined behaviour for simple networks and low memory requirements which is a useful attribute given the high memory usage of convolutional networks. While another algorithm may be more optimal, training the model for longer is not a constraint

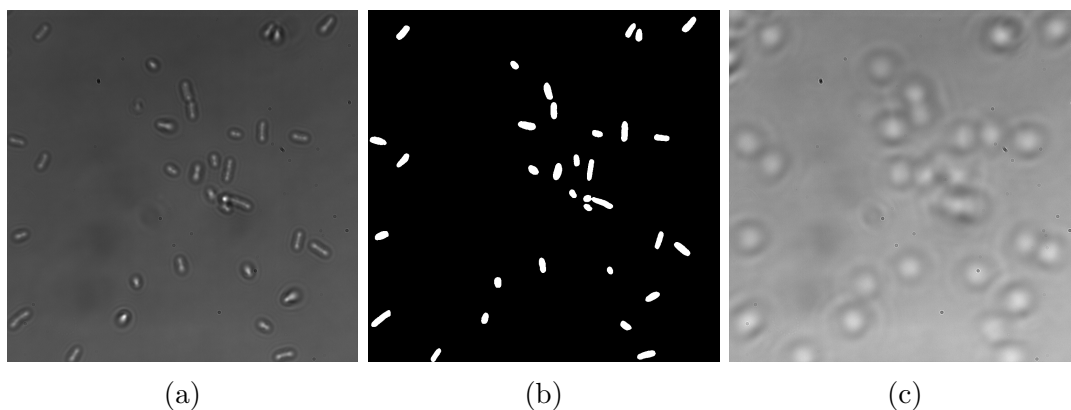


Figure 3.11: Selected training images from training set. a) Brightfield image close to focus on cells with high contrast. b) Training answer image for image in (a) with cells coloured in white. c) image from far end of z-stack where (a) came from, where focus is approximately $7\ \mu\text{m}$ above (a).

for our application since I intended to train it once and then use a fixed version for all data analysis. The function is a first-order gradient based optimisation algorithm designed for stochastic objective functions [126] and requires a few parameters, most importantly a learning rate (which I chose as 0.001) which defines the size of the steps the algorithm makes in attempting to reduce the error function of the neural network. The networks error function is defined in equation 3.8 where it compares the networks predicted binary image with the answer binary submitted. The Adam algorithm then attempts to optimise this error function by manipulating the weights of the neural network over many iterations.

$$error = \sum_0^{npix} (prediction - answer)^2 \quad (3.8)$$

3.3.2 Network training and verification

Production of training images

In order to train the network a set of training data must be constructed consisting of a set of sample images and the corresponding answer key. For an image segmentation algorithm with two possible categories, cell or not cell, a binary image is used as the answer key. To produce training images, I prepared a tunnel slide and imaged cells as described in methods 2.3. From the video I identified a frame where the cells were most in focus on the surface of the slide (Fig 3.11a) and processed the image by hand, to create a single binary image with cells located in white as in Fig.3.11b. Since the z-stack occurs in a short timescale, the cells do not move between each slice taken and therefore the answer key created from the in plane cells can be used for slices that are less in focus. I chose a set of 15 slices representing a $\pm 7\ \mu\text{m}$ depth around the focal plane. I chose to include images from multiple conditions, both low osmolarity, high osmolarity

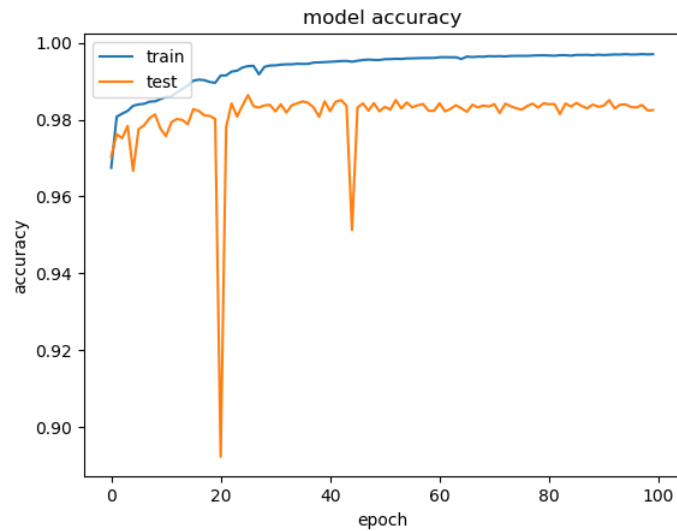


Figure 3.12: Training history for the first 100 epochs of network training. Blue line represents the accuracy when presented with training images and the orange line is the accuracy when presented with unseen data. The accuracy is calculated as the normalised fraction of correctly categorised pixels.

in sucrose and NaCl and finally a series of images with no cells present. This was to ensure that any changes in cell appearance due to medium changes, and the background of the microscope would be accounted for by the neural network.

Once a selection of images had been selected from the real world data they were converted from .TIFF to .PNG files in order to save computer memory while loaded.

Network training

The network training is primarily handled by the Keras package as described here <https://keras.io/> [127]. In brief: the package loads all the training images and their respective answers, a subset of images is set aside for verification and the rest of the images are shown to the network one by one for training. Between each image the output of the network is compared to answer image and the weights of the network adjusted based on the training algorithm.

Each complete run through of the training set is known as an epoch, and between each epoch the network is tested against the verification dataset so that images it has never seen are checked to determine if the network has actually improved instead of learning the answers to the training set only. If the verification accuracy is lower than a previous epoch, all training for that epoch is discarded.

The network can be trained for a specific number of epochs or until a particular accuracy is met, in the case of my network it was run for 300 epochs. The accuracy values for the first 100 epochs is present in Fig. 3.12, demonstrating improvement with each epoch with diminishing returns over many iterations. Test accuracy is always lower than train accuracy as the network has never seen the test data and is limited both by its own complexity (a network with more

parameters can fit a wider range of inputs) and the amount of training data it has observed. The significant drops in accuracy with the test data indicate poor training or overtraining on the data, where the network produces the correct answer image without actually learning to interpret them correctly. In these cases the modifications to the network are discarded and another round of training begins from the previous good set.

Once trained, the network produces binary images where the cells are identified. From these images the centres of mass of each blob are determined by a determinant of Hessian blob finding algorithm [128], using the following parameters: max sigma=200, min sigma=25 and overlap=0. This generates the centres of masses of every blob, in each frame in the z-stack. A clustering algorithm, in this case a DBSCAN algorithm [129], must then be used to identify clusters as an individual cell will be identified in multiple consecutive frames with only small amounts of x-y drift. The DBSCAN was performed with an distance function equal to 30 and minimal cluster size of 3, which were chosen after several manual iterations based on known good data, an example output is provided in Fig. 3.13. Finally, the number of unique clusters is used as the total cell count for the sample.

When operating on a GTX1080 GPU (nVidia) and with Tensorflow v1.13 the network can process a single image in approximately 0.09 sec which would allow its use in real time on microscope images if desired. Such application could be useful for segmenting fluorescent cells for determining volume or other parameters while an experiment is taking place instead of in post processing.

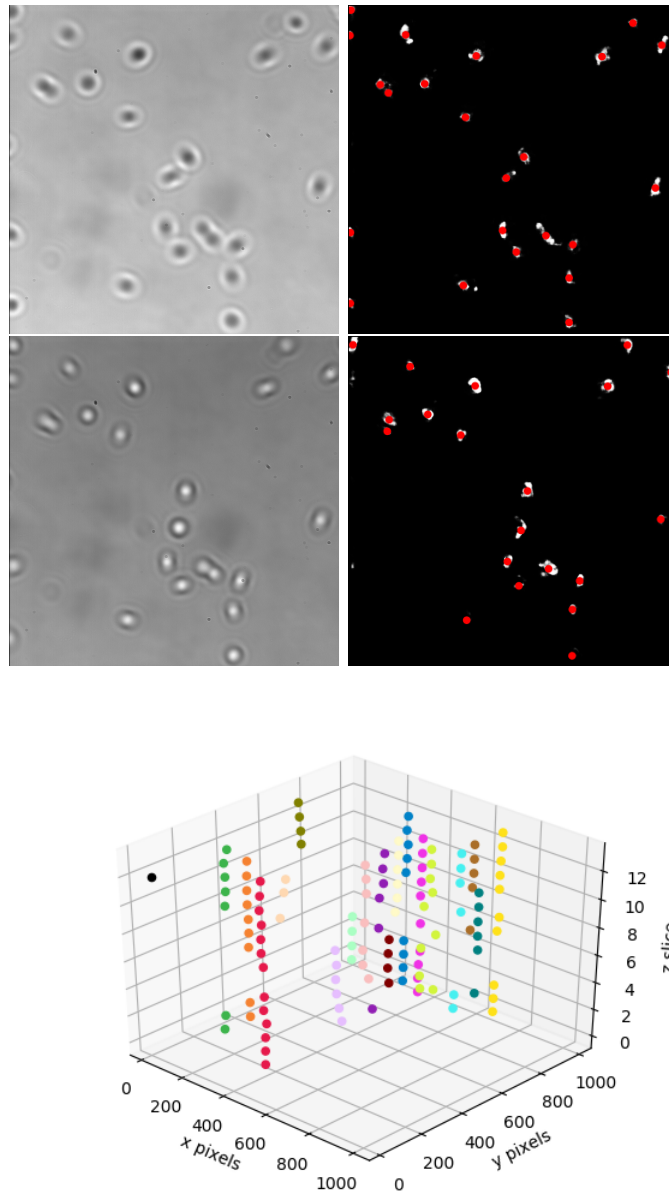


Figure 3.13: Sample input data to the counting algorithm, restricted to a $6\ \mu\text{m}$ z distance around the focal plane for clarity. Top images, left: microscope images input for analysis, right: neural network binary output with determined cell centres of mass as red spots. Lower image: final output of the network and cell counting algorithm; a 3D map of cell centres of mass. Each colour represents a different identified cluster and therefore cell ($n=18$) with the single black marker on the left indicating a false positive excluded by the clustering algorithm and therefore the count. Gaps around the 4th z slice are a result of cells being in focus and losing contrast below the networks detection threshold.

Chapter 4

Industrial ethanol production

4.1 Model of industrial ethanol production to calculate potential cost savings

4.1.1 Motivation

Since the goal of this project is to determine if the osmoregulatory network can be used to improve the ethanol production from syngas used in an industrial plant, I constructed this simple mass balance model with the goal of understanding how changing the parameters of growth and ethanol resistance would affect the production costs of ethanol. The mass balance model is based on a simplified view of an industrial ethanol production facility designed around the IneosBio process which uses syngas to provide the carbon source [28] and microbial fermentation to convert it to ethanol [130]. The overall process is more completely described in section 1.2.

4.1.2 Model components

Syngas

For the sake of cost calculation, we will take the IneosBio method of syngas production as the default; gassification of plant material using steam in an anaerobic environment [18, 28]. Combined with further processing to remove excess CO_2 , this will produce syngas with a carbon monoxide concentration of about 80% by mass [16]. In addition the I estimated cost of producing this syngas at around 0.05\$ per m^3 [131] however more exact values are difficult to obtain due to the close guarding of industrial patents and values. However, this value will not be altered during this modelling exercise and therefore an approximate value can be reasonably used.

Biological growth

The bacteria in the fermenter convert the dissolved syngas, which is primarily CO at this stage, into biomass and ethanol. The conversion efficiency of the microorganism is quoted as the percentage of a mole of CO converted to ethanol instead of biomass or other byproducts. From the patent literature, we find that the conversion efficiency for the IneosBio industrial strain of *C.ljungdahlii* is

86% [28] by mole, therefore, the moles of CO required to produce 1L of ethanol is:

$$N_{CO} = \frac{(\rho_E/M_E) * K_E}{(k_{CO})} \quad (4.1)$$

Where k_{CO} is the molar conversion efficiency, ρ_E is the density of EtOH, K_E is the stoichiometric conversion ratio of EtOH to CO, and M_E is the molar mass of EtOH. Substituting in:

$$119.485 \text{ mol l}^{-1}_{\text{EtOH}} = \frac{(0.789 \text{ kg l}^{-1}/0.04607 \text{ kg mol}^{-1}) * 6}{(0.86)} \quad (4.2)$$

Since the generation of ethanol is a direct result of the bacterial metabolism we can assume that the majority of the heat produced in the bioreactor is as a result of this process. From the stoichiometry we know that this releases -224 kJ mol^{-1} as heat, either directly or as a result of subsequent reactions, we can calculate the minimum heat production of the bioreactor as:

$$E_r = \frac{\rho_E}{M_E} * \Delta H \quad (4.3)$$

Substituting in:

$$3836.2 \text{ kJ l}^{-1}_{\text{EtOH}} = \frac{0.789 \text{ kg l}^{-1}}{0.04607 \text{ kg mol}^{-1}} * 224 \text{ kJ mol}^{-1} \quad (4.4)$$

This does not take into account additional heat from the input of of syngas, the mechanical stirring devices or the conversion of other compounds from the medium and as such it is purely a minimal requirement.

Fermenter cooling

To cool the reactor, most plants will use locally available water sources and a heat transfer system to allow for cheap and efficient cooling. This water however is not free due to the costs incurred in filtering and pumping the water through the plant and as such the volume required needs to be calculated. Assuming that the maximum heat transfer occurs, where the coolant reaches the temperature of the reactor, the required volume can be determined by:

$$V_c = \frac{E_r}{c_{water} * (T_r - T_c)} \quad (4.5)$$

Where V_c is the volume of coolant water, T_r is the temperature of the reactor, c_{water} is the specific heat capacity of water and T_c is the temperature of the coolant water intake.

Substituting in for a reactor of 38°C and cooling water of 10°C :

$$32.77 \text{ l l}^{-1}_{\text{EtOH}} = \frac{3836.2 \text{ kJ l}^{-1}_{\text{EtOH}}}{4.181 \text{ kJ l}^{-1} \text{ K}^{-1} * (28 \text{ K})} \quad (4.6)$$

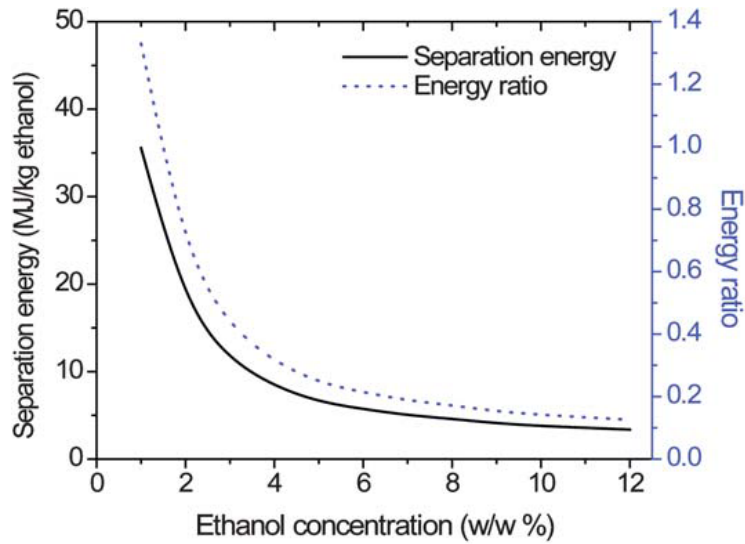


Figure 4.1: Separation energy of water-ethanol solution as a functional of ethanol concentration over a physiological range. Energy ratio is the ratio between separation costs and energy returned during combustion of the pure ethanol. Data and figure obtained from [132].

Centrifugation and flash separation

Beer is taken from the fermenter and centrifuged to separate the cells. This is usually accomplished via continuous methods such as centrifugation or filtration, in the case of bacteria centrifugation is preferred due to the small size of the bacterium. Following that, the beer undergoes a process of flash separation to remove the excess carbon dioxide from the solution as it will agitate and foul the distillation column. These processes are assumed to be of little cost relative to the rest of the process as they rely on fluid pumps as the driving mechanism. They are also unlikely to change with any of the parameters of interest as they are dependent of the physical parameters of the fluid and cells.

Distillation

For distillation we calculate the energy requirements based on an ideal column, that has a bottoms concentration of 0.4% and a product concentration of 90% [30, 33].

$$E_{dis} = 33.041 * c^{-0.949} \quad (4.7)$$

Where c is the beer concentration and E_{dis} is the energy requirement MJ for producing 1 kg of 90% ethanol solution from a beer with ethanol concentration of c percent. The final distillation of the 90% azeotrope and any further processing of the ethanol/distillate is not included as it will not vary with our parameter space.

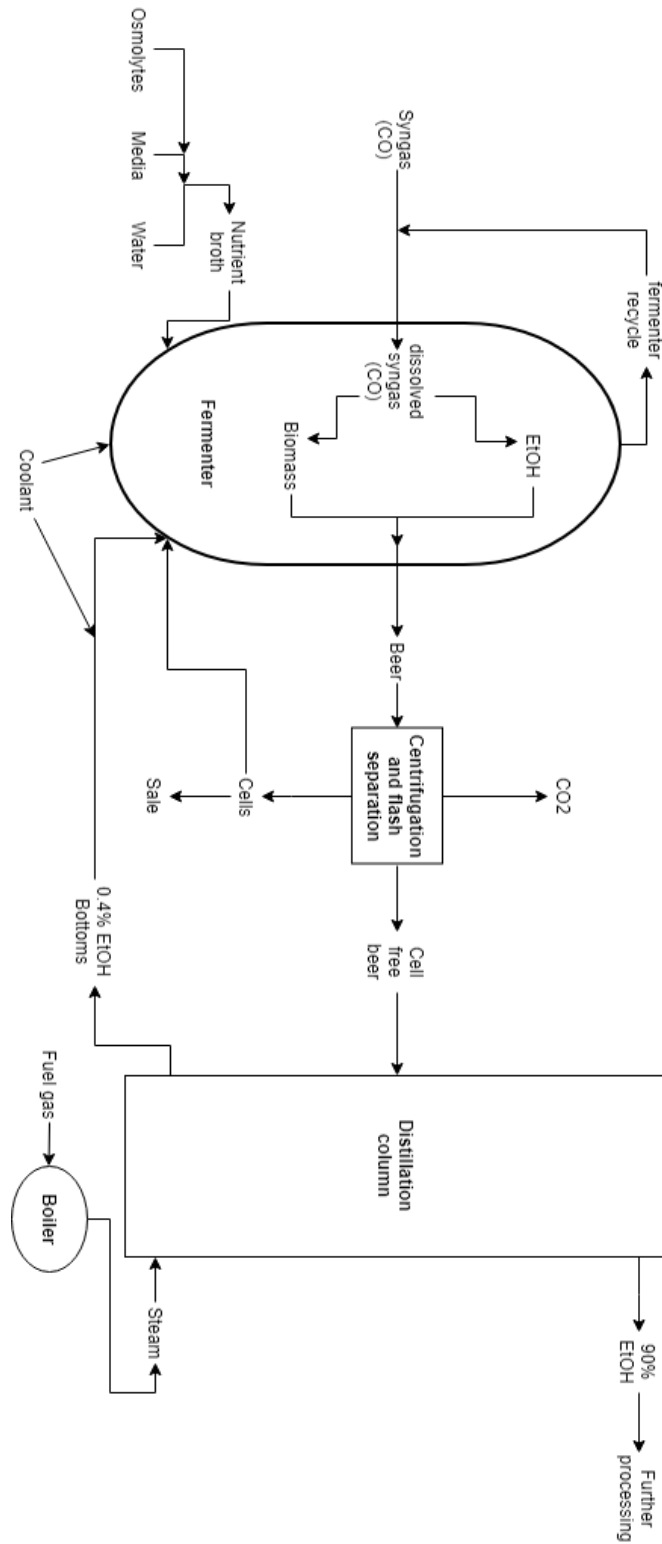


Figure 4.2: Outline of the theoretical bioethanol production process used in the economic modelling and testing

Economic Value	Units	Model value	Range 1yr		Range 5yr	
			low	high	low	high
Ethanol	\$/l	0.41	0.317	0.407	0.317	0.946
Fuel gas	mmBTU	3.5	2.53	4.93	1.68	5.39
Medium	\$/l	0.2 [133]				
CO ₂	\$/ton	0				
Cell mass	\$/ton	0				

Table 4.1: The vales of sale and purchase of various components for the bioreactor process. Where high variation is expected, in commodity products such as ethanol and fuel gas the past ranges are also displayed in both the short and long term. The values for CO₂ production and cell mass are listed as 0 as while the model has the values as variables, the market for cell mass is generally a local property and no carbon tax for the production of CO₂ from biological sources in the United States or European Union.

Plant variable	Units	Model value
Cooling water cost	\$/ton	0.02
Cooling water temp	°C	10
Medium makeup water	\$/ton	0.23
Fuel gas to steam efficiency	%	90
Syngas cost	\$/m ³	0.05 [131]
Syngas CO concentration	%	80 [16]

Table 4.2: Values for plant variables used in the model, these values are fixed throughout all experiments and represent an expected cost based on a large industrial scale plant.

Bioreactor key values	Units	Model value
Syngas CO conversion efficiency	%	86 [28]
Reactor temp	°C	38 [28]

Table 4.3: Model values for the bioreactor based on the patent literature of Scott *et al.*

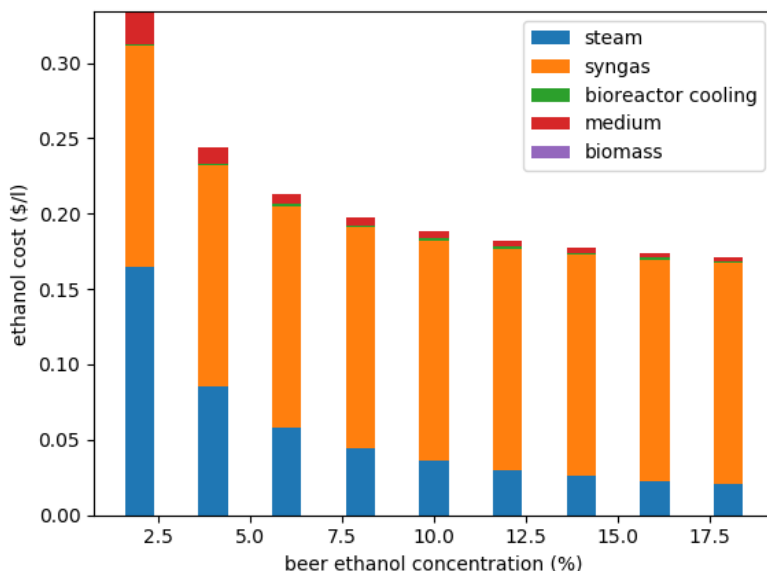


Figure 4.3: Cost per litre of ethanol as calculated by the section of the plant modelled in Fig.4.2 vs the ethanol concentration of the beer produced by the bioreactor. The columns are coloured to represent the breakdown of the costs as calculated. Biomass is not visible due to being set to zero for this simulation, parameters used for simulation are listed in Table 4.1 & 4.2.

4.1.3 Sensitivity analysis

Beer Concentration

The most obvious property to change in this environment is the beer concentration coming out of the bioreactor. In reality this would be achieved by improving the ethanol tolerance of the strain without affecting any of the other parameters of the microbial growth. The results of modifying this single parameter are shown in Fig.4.3, where the greatest cost reduction is in producing the steam to power the distillation column. This drops exponentially with an increase in beer concentration, as would be expected based on Fig.4.1. In addition because less beer is needed to produce the same volume of ethanol per unit time, the volume of medium required is reduced as well.

It is also evident that improving the bacterial tolerance gives diminishing returns, however since the resistance of *C.ljungdahlii* is quoted around 2 to 5% it remains within the sensitive region and therefore even a small increase should save a significant amount of cost. *E.coli*, as shown in section 2.5 has a tolerance already at 5.5% at 37 °C that can increase to 7.25% by reducing temperature to 25 °C is also within the sensitive region of the proposed model. Performing this reduction in temperature would save approximately \$0.06 per litre of ethanol, while small this would be significantly amplified by the output of the plant.

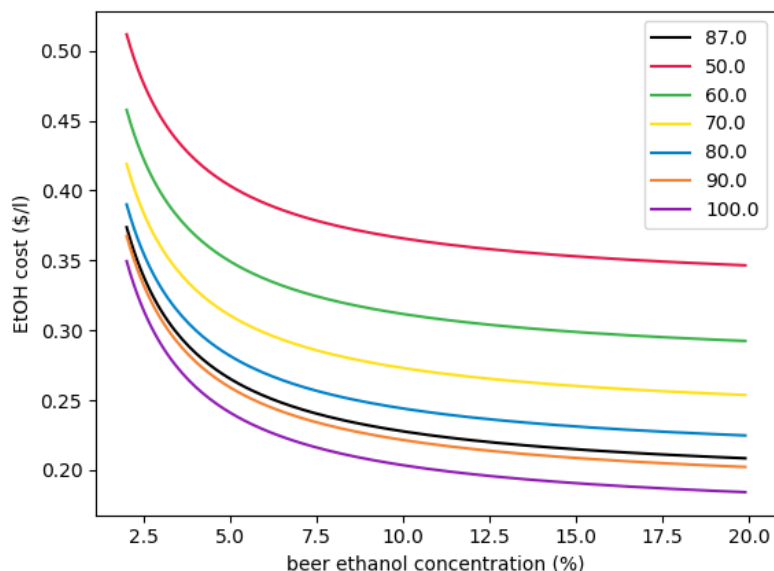


Figure 4.4: Beer concentration vs cost of ethanol production for different carbon monoxide conversion efficiencies. The legend gives the conversion efficiency of the simulated bacterium in percent, with the black line at 87% being the default for the model.

Syngas conversion efficiency

The syngas conversion efficiency is another parameter of the bacteria that could be altered by manipulating the osmoregulatory system. Since the conversion of CO to ethanol is the primary metabolic pathway for the bacteria the osmoregulatory network could be used to increase the energy consumption of the bacteria without increasing the proportion of CO used for growth and thus increasing the total conversion efficiency. The effects of attempting to alter the metabolism are explored in Fig.4.4, where increasing the conversion efficiency reduces the ethanol cost per litre with diminishing returns compared to earlier. As the conversion efficiency of *C.ljungdahlii* is already high (around 87%) and the ethanol tolerance low (approx 3%) altering this efficiency is going to have very limited cost reduction potential, only with around 0.01\$ reduction per litre if the conversion efficiency reaches 100% [26].

Increasing the conversion efficiency would also reduce the growth rate of the bacteria, and therefore increase the pre-growth needed before the bioreactor reaches its full production capacity. It may also affect the maintenance of the production rate, since bacteria get damaged by the stirring action of the reactor, downstream processing such as centrifugation or contamination by external agents and need to be replaced with freshly grown cells. Since this model assumes the plant is already operating in a steady state and cell growth rates for startup would be very particular to the plant setup, there is no reasonable way to estimate the economic impacts.

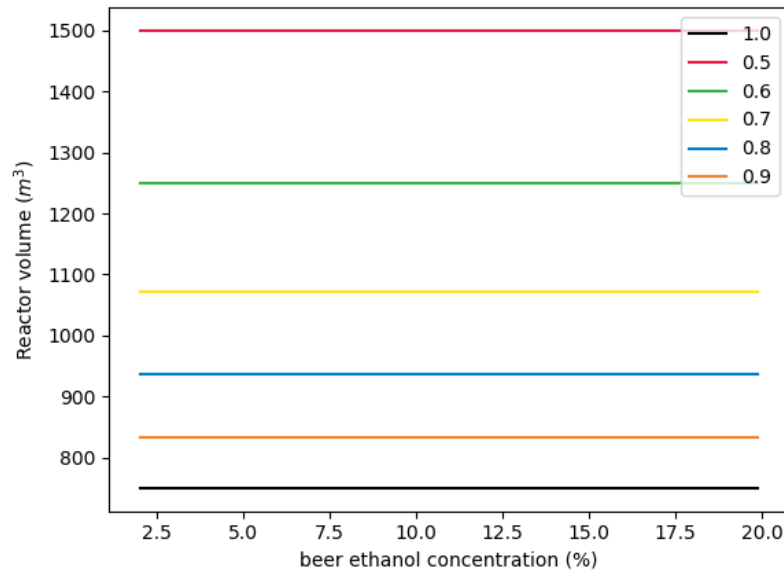


Figure 4.5: Reactor volume required to meet a production rate of 3170 litres of Ethanol per hour (20000 tons per year at 8000hours of operation) at various beer concentrations. Growth rate as proportional to the default model parameter is indicated by the colours and legend.

Growth rate modulation

As has been mentioned before and is demonstrated with the temperature modifications in section 2.5, it is important to consider the impacts that changes to the growth rate have upon the model. Since the model ties the growth rate of the bacteria directly to the ethanol production rate, changes to the growth rate will have no effect on the ethanol cost per litre. Instead, the production rate of the bacteria will influence the size of the bioreactor(s) needed to meet a given production rate. This calculation is presented in Fig.4.5, showing the large increases in bioreactor volume to meet the target production rate.

The largest bioreactors in use in industry are on the order of 800 m³ and as such the production/growth rate of the bacteria requires that at least two bioreactors be used to supply the rate of the plant. Since bioreactors are some of the most expensive pieces of equipment to construct this means any significant reduction in growth rate would lead to a large increase in capital cost for the plant.

4.1.4 Conclusions for production

From the above graphs and sensitivity analysis it is evident that the greatest route of study is the increasing of the ethanol tolerance of the bacterium. The exact savings however would depend on the initial concentration of the beer from the bioreactor, with lower concentrations seeing a more significant benefit for the same level of increase. It is also important to avoid changes to the growth rate

while achieving this as the increase in bioreactor volume (to maintain production volume) required may offset any benefit gained.

4.2 Characterising *E.coli* ethanol tolerance

In order to measure any changes to ethanol tolerance I first designed the protocol given in methods 2.5 to account for evaporation and provide consistent results over multiple days with various strains and media. I chose to use a probabilistic method of determining the lethal ethanol concentration, in a similar manner to MIC calculations, rather than quantify changes to the growth rate or yield directly. This is because ethanol changes the refractive index of the medium upon addition and as demonstrated in chapter 3.1 this would significantly affect the interpretation of the cell masses within the platereader. Cell volume could also be changing with the different conditions as it is known to change with growth rate and stage of growth in the growth curve making calibration difficult. In addition I found that addition of the ethanol caused many of the commonly used buffers, such as those used in Chapter.3.2 where the cell number calibration is stable, to precipitate the salts present both immediately and over time rendering reliable reading of optical densities impossible.

4.2.1 Temperature dependence of ethanol tolerance

Due to an unexpected setting change to our platereader a sample was incubated at a lower temperature than normal, 32 °C instead of 37 °C, I noticed a significant improvement in the ethanol tolerance of our strain. I chose to characterise the effects on our strain particularly the relationship between temperature and the growth rate in order to quantify the trade-off between the tolerance and growth rate and inform the later experiments. As is shown in Fig.4.6 there is a significant increase in the ethanol tolerance, from 5.75% to 7.75% with a reduction to 25 °C. Since the ethanol production of *C.ljungdahlii* is linked directly to the central metabolism its production will be proportional to its growth rate and therefore be reduced with the decrease in temperature. In order to compensate, as is demonstrated in Chap.4.1 the plant must be made significantly larger to compensate and therefore is unlikely to be useful on its own.

4.2.2 Characterising medium supplementation on ethanol tolerance

In an attempt to determine if osmotic agents would be useful at improving ethanol tolerance by growing the bacteria in minimal medium supplemented with osmolytes, specifically choline, proline and glycine betaine. This data is presented in Fig.4.7a I attempted to understand the effect of supplementing minimal salts medium with proline and choline. I also prepared LB with double the normal concentration of components to see if the medium could be improved for ethanol tolerance, Fig.4.7b. Unfortunately we saw no positive effects with either attempt at supplementing the medium, and I was limited exploration of more complex defined medium as salt based buffers and low solubility organic compounds are easily displaced from the medium upon addition of ethanol. The precipitate caused by this not only changes the concentration of the medium but prevents any reading by the platereader as the beam path passes through the bottom of

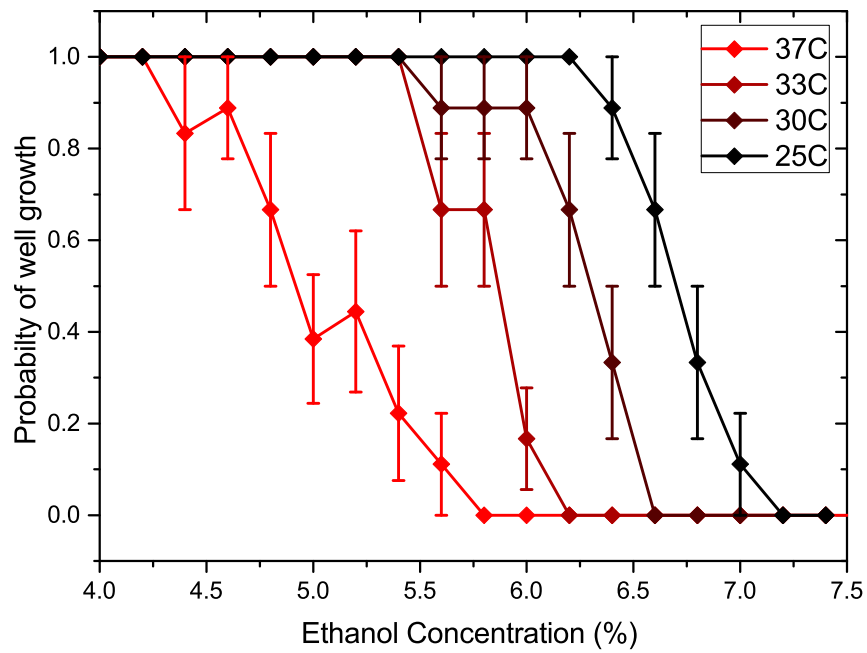


Figure 4.6: Temperature dependence of probability of growth of an inoculated well. Temperatures displayed are 37, 33, 30 and 32 °C increasing temperature is indicated by increasing red brightness. Error bars are the 85% Normal approximation interval calculated by the Wald method.

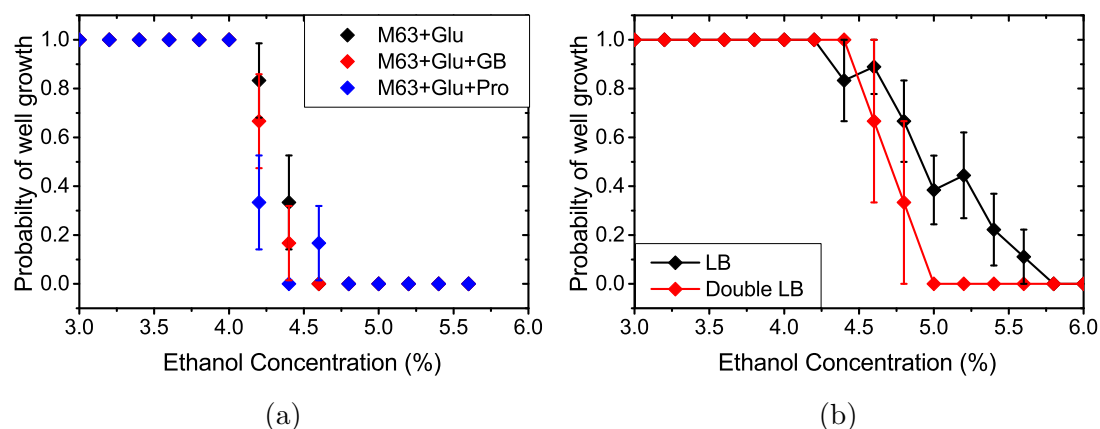


Figure 4.7: The probability of a well growth vs the ethanol concentration for a) M63 with glucose (black) supplemented with choline (red) and proline (blue). b) Normal LB (black) and LB with double the usual yeast extract and tryptone (red). Error bars are the 85% Normal approximation interval calculated by the Wald method.

the well, and thus any precipitate interferes with readings.

4.2.3 Osmotic increase

To determine if osmoregulation provides a useful additional tolerance to bacterium without any further modification to the bacterium I tried exposing the *E.coli* to high osmolarity and then to ethanol. In order to make sure the cells were not exposed to both an osmotic shock from the agent and the ethanol simultaneously I first grew cells in medium of appropriate osmolarity and made frozen stocks of the recovered and growing cells. After this the protocol outlined in methods 2.5 was followed to produce the data present in Fig.4.8. As can be seen, when exposed to either sodium chloride or sucrose, the cells have a lower tolerance for exposure to the same concentrations of ethanol. This probably indicates that the osmolarity and the ethanol are both causing continuous stress on the cells as they grow in line with previous research [87]. This is also supported by the use of combination therapy techniques with antibiotics, where cell growth is inhibited using several mechanisms simultaneously.

4.2.4 Ethanol tolerance of osmoregulatory knockout strains

To determine if any particular parts of the osmoregulatory network is essential for ethanol tolerance in *E.coli*, I decided to test the ethanol tolerance of various Keio collection single gene deletion mutants. Fig.4.9 shows the results of growth of selected mutants with ethanol. While many of the mutants show next to no difference compared to the wildtype or BW25113 (the Keio collection parent strain [107]) the $\Delta proW$ strain shows a significant reduction in ethanol tolerance. Since the *proW* gene is part of the ProU complex, responsible for transporting betaines (glycine and proline betaine) into the cell in response to osmotic stress

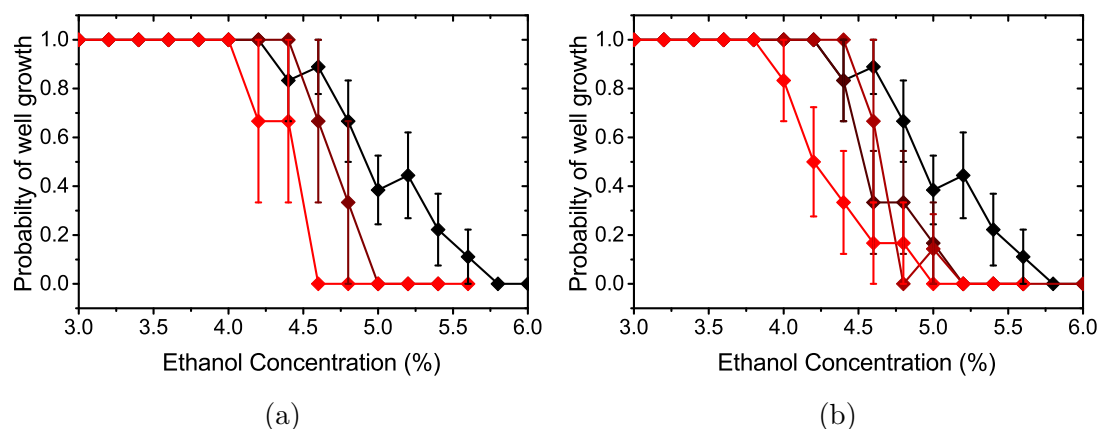


Figure 4.8: The probability of a well growth vs the ethanol concentration for MG1655 at different osmolarities in the presence of sodium chloride (a) sucrose (b). Increasing redness indicates increased osmotic concentration. a) osmolarities are 0, 750 and 1500mOsm with $n \geq 3$. b) osmolarities are 0, 450, 750 and 1500mOsm with $n \geq 6$. Error bars are the 85% Normal approximation interval calculated by the Wald method.

[93, 134, 135], betaines must be important to ethanol tolerance. This may be due to the suggested protein stabilisation properties of glycine betaine [135].

4.2.5 Discussion

Ethanol and osmolarity have a number of similar effects on the cell membrane and protein stability as discussed in the introduction 1.4. The aim of this chapter was to quantify the ethanol tolerance of *E.coli* under varying media conditions as well as test the tolerance of osmoregulatory mutants from the Keio collection. Of interest, is the reduction of ethanol tolerance by the deletion of the *proW* gene by almost 2.5% compared to the wildtype as demonstrated in Fig.4.9. This link between ethanol tolerance and the ProU transporter system, of which ProW is a component, is previously unreported link for *E.coli*. As a result we can infer that osmolytes transported through this transporter must have a crucial role for the ethanol tolerance of *E.coli*.

Since the primary osmolyte transported through this system is glycine betaine, we would expect that adding this osmolyte to otherwise minimal medium would improve the ethanol tolerance. However, upon doing this as in Fig.4.7a we see no improvement to the ethanol tolerance of the wildtype. It may be that another osmolyte is at play here, such as ectoine, or proline betaine which are also substrates for the ProU transporter however these are yet to be tested. Due to the variation and complex environment of the LB medium it is unclear how much of these compounds is present in the LB during the other experiments [62].

When I discovered the effect of changing the temperature of growth had upon the ethanol tolerance, I felt it was important to characterise it completely. As such I determined that the tolerance could be increased significantly, with an increase from 5.75% to 7.75% by reducing growth temperature from 37 °C to

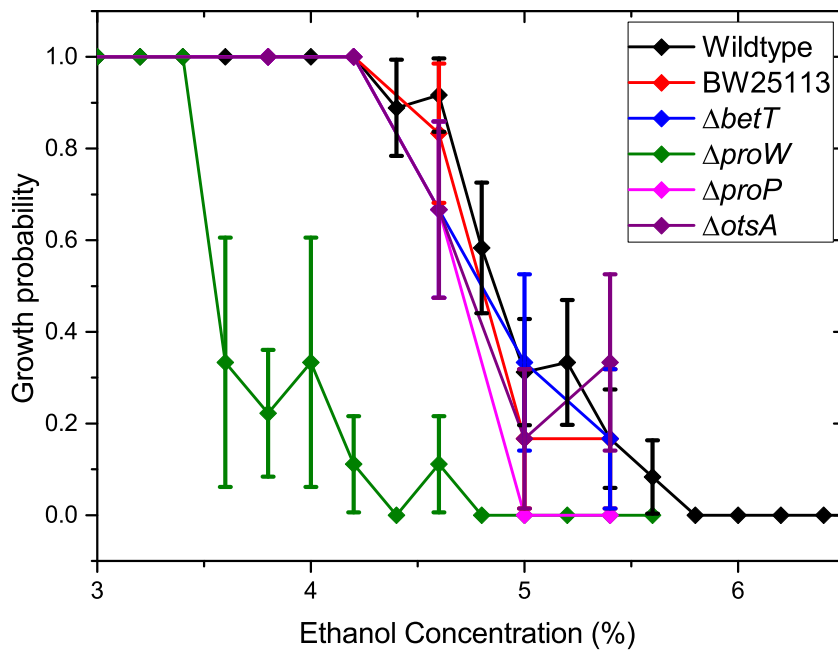


Figure 4.9: The probability of a well growth vs the ethanol concentration for wild-type (MG1655), BW25113 and Keio collection mutants for several osmoregulatory proteins. Error bars are the 85% Normal approximation interval calculated by the Wald method.

25 °C. This effect was to be expected as the stability of proteins [99, 103] and the lipid bilayer of the membrane are improved with a reduction in temperature, along with a reduction in the solvent properties of the ethanol [85, 95, 96, 136, 137].

It did however provide a useful trade off, as reducing the temperature decreases the growth rate of the bacteria by about half while improving the ethanol tolerance. When this data is applied to the model given in section 4.1 we see an improvement of \$0.06 per litre of ethanol but the reduction in growth rate requires a doubling of the bioreactor volume. This trade off is significant in terms of capital cost despite the improvement in production costs.

Chapter 5

E.coli physiology at high osmolarity

As described in the introduction, the reduction in growth at high osmolarity is not currently explained and therefore of interest to research. This would be useful because if any improvements in ethanol tolerance were to arise from the use of high osmolarity, then understanding reasons for the reduction in growth rate at high osmolarity may help mitigate or improve this.

The work in the following chapter is based upon my hypotheses of why cells grow slower at higher osmolarity. In brief, these are:

(i) the allocation of ribosomes to synthesising different components of the osmoregulatory network will lower the number available to synthesis of new ribosomes and cell construction machinery, section 5.1

(ii) transporters and enzymes consume energy or carbon source meaning that there is less for building cells giving a reduction in cell yield, section 5.2

(iii) transport and synthesis of molecules to reverse the osmotic gradient increases the concentration of components in the cytoplasm, which may limit the movement (diffusion) of other molecules, section 5.3

I therefore intend to measure all three of these variables in the following chapter, followed by including them in a coarse grained model to help provide a more quantitative understanding of whether changes to these three variables explain the reduction in growth rate.

5.1 Proteome allocation

It has been shown that the fraction of cell protein content that is made up of ribosomes varies linearly with growth rate when growth rate is modulated by altering the medium nutrient capacity (sometimes called nutrient quality) [71]. While some measurements have been made to observe changes at high osmolarity, there is some indication, as shown in Fig.1.6B and further discussed in the introduction section 1.3.3, that the changes that occur at high osmolarity are different than those that occur due to changes in nutrient quality. I therefore set out to measure these changes myself, with the hope of integrating them with my other measurements to produce a better overall understanding of the reason

for reduced growth.

5.1.1 Ensuring exponential growth

In order to ensure good measurements for all experiments into the physiology of *E.coli* it is important to ensure that all parameters are measured while the cells are in the same phase of growth. The easiest way to do this is to grow cells to a particular OD using the same protocol each time, however, since the eventual goal is to create a model of the bacterial growth at high osmolarity, we would like to understand where the limits of the model will be. Most bacterial measurements are made in the mid-log phase of growth as determined by optical density measurements but as is described in chapter 3.2 these measurements can be misleading and as such do not tell us about the true state of the bacteria.

To determine if the bacteria are truly in a steady state, and for how long, I decided to measure the protein concentration along a series of growth curves. If the bacteria exist in a steady state for a period then the relationship between optical density and protein concentration should be linear until the cells run out of nutrients. When I performed these measurements, shown in Fig.5.1, I found that the protein vs OD relation holds linear to a remarkably high optical density to almost a value of 2. Above this OD the error rate of the protocol starts to climb, producing more of a scatter of data. The reason for this is due to the precipitation and centrifugation steps of the protocol, where small amounts of protein or cells can be lost and therefore create an error between multiple samples and even the calibration curve used to convert the absorbance to protein concentration.

Despite these difficulties, I determined that the bacteria are within a steady state between an OD of 0.1 and 0.6 and thus all further measurements were made within this range.

5.1.2 Verifying previously observed measurements of proteome fraction

Since this investigation is based upon previously described data, and I intend to use the Scott *et al* model to help interpret the changes to the *E.coli* physiology, it was important to prove that I was able to replicate their results. This is further necessary as the wildtype strain I use BW25113 may differ from the EQ2 strain (based on MG1655) used in the previous work.

When I plot my data against the data from Scott *et al* in Fig.5.2 I see some agreement with the slope of the line despite the significant error bars. This is in contrast, however, to comparison of growth rates with my cells having a reduced growth rate in RDM and an increased growth rate in all the M63-media. In addition my data shows little change in the RNA/protein ratio when moving from glycerol to glucose as a carbon source but while showing a more significant change between the absence or presence of casamino acids. It is unclear why this discrepancy exists as the genetic differences between strains do not overlap with any of the primary carbon metabolism genes (with the exception of lactose and arabinose which are not used in these experiments). Further experiments with

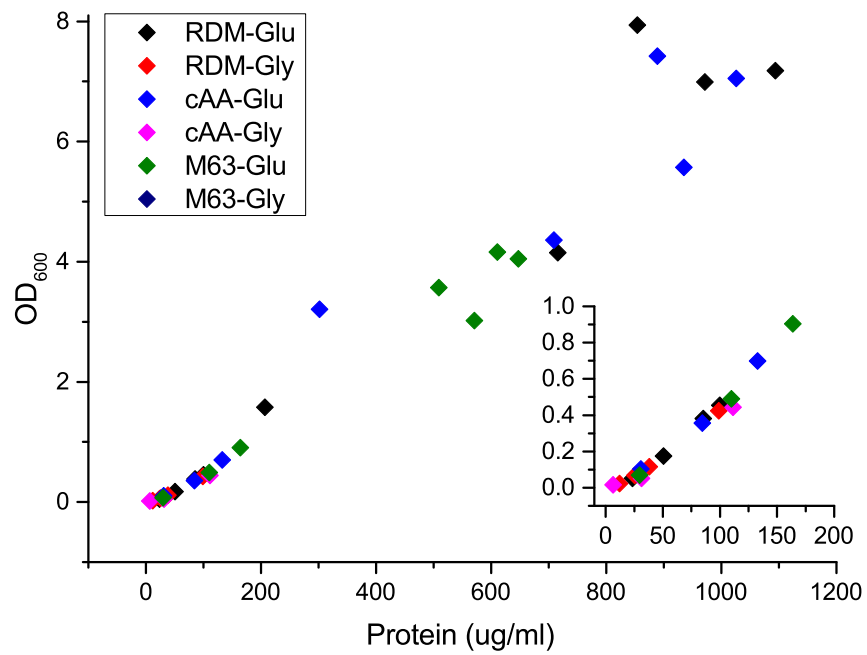


Figure 5.1: Protein content as $\mu\text{g ml}^{-1}$ vs the optical density at which the protein content was measured for 6 different media as defined in section 2.1.3. Inset is a magnified view of the data. Medium richness decreases down the legend.

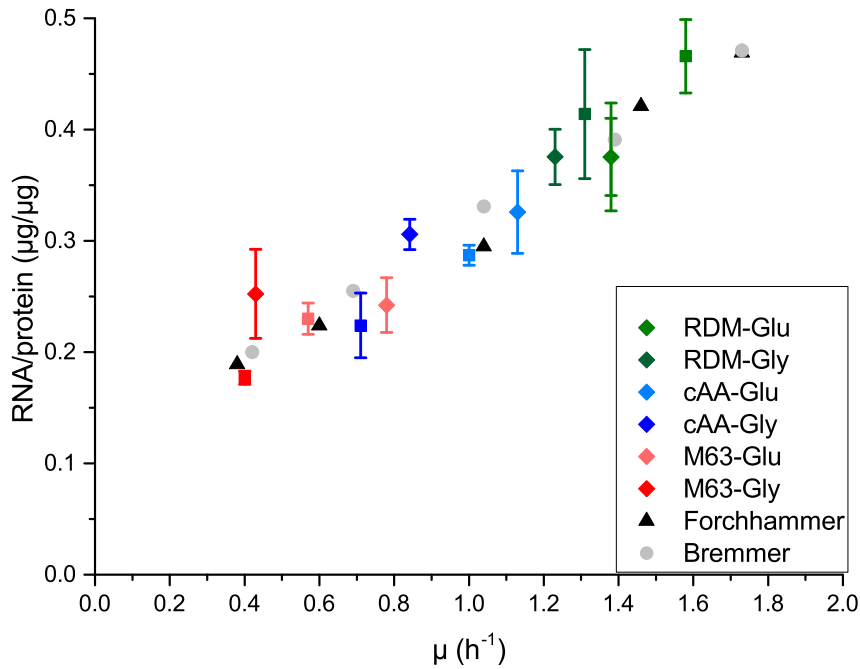


Figure 5.2: The RNA/protein ratio vs growth rate for the bacterial cells grown in different nutrient media. Colours indicate the medium for both squares and diamond data. Squares: Data from Scott *et al* paper [71]. Black triangles and grey circles: historical data from Forchhammer [138] and Bremmer [139]. Diamonds: data from this thesis. Error bars are not given in historical data, bars on Scott and this thesis data are standard error.

different strains and growth conditions may help shed light on this behaviour.

5.1.3 Changes to protein/RNA ratio at high osmolarity

Concurrent with the measurements above, I grew cells at high osmolarity with sucrose and performed the RNA and protein measurements. I chose to only perform the measurements in M63 medium with glucose as the carbon source due to the high growth rate and low cost compared to the RDM and Glycerol media.

The data in Fig.5.3 shows a decrease in growth rate as well as RNA/protein ratio as the osmolarity is increased with sucrose. As can be seen in the projection on the back wall, in medium containing casamino acids (cAA) represented by light blue spheres the decrease in RNA/protein ratio proceeds along the same line as a decrease in nutrient quality in normal osmolarity. In minimal medium containing just glucose and salts (pink spheres) the RNA/Protein ratio is shifted down relative to the line formed by normal osmolarity. While as previously mentioned there is some error in the measurements, the points are shifted systematically in two different ways rather than being randomly noisy. Assuming this difference is real, it is interesting that the two media would produce different responses to the

same osmotic challenge. I hypothesise that this may be due to the fact that caseino acids contain organic osmolytes and therefore the cells grown in its presence may require a smaller proteome fraction to adapt to changes in osmolarity.

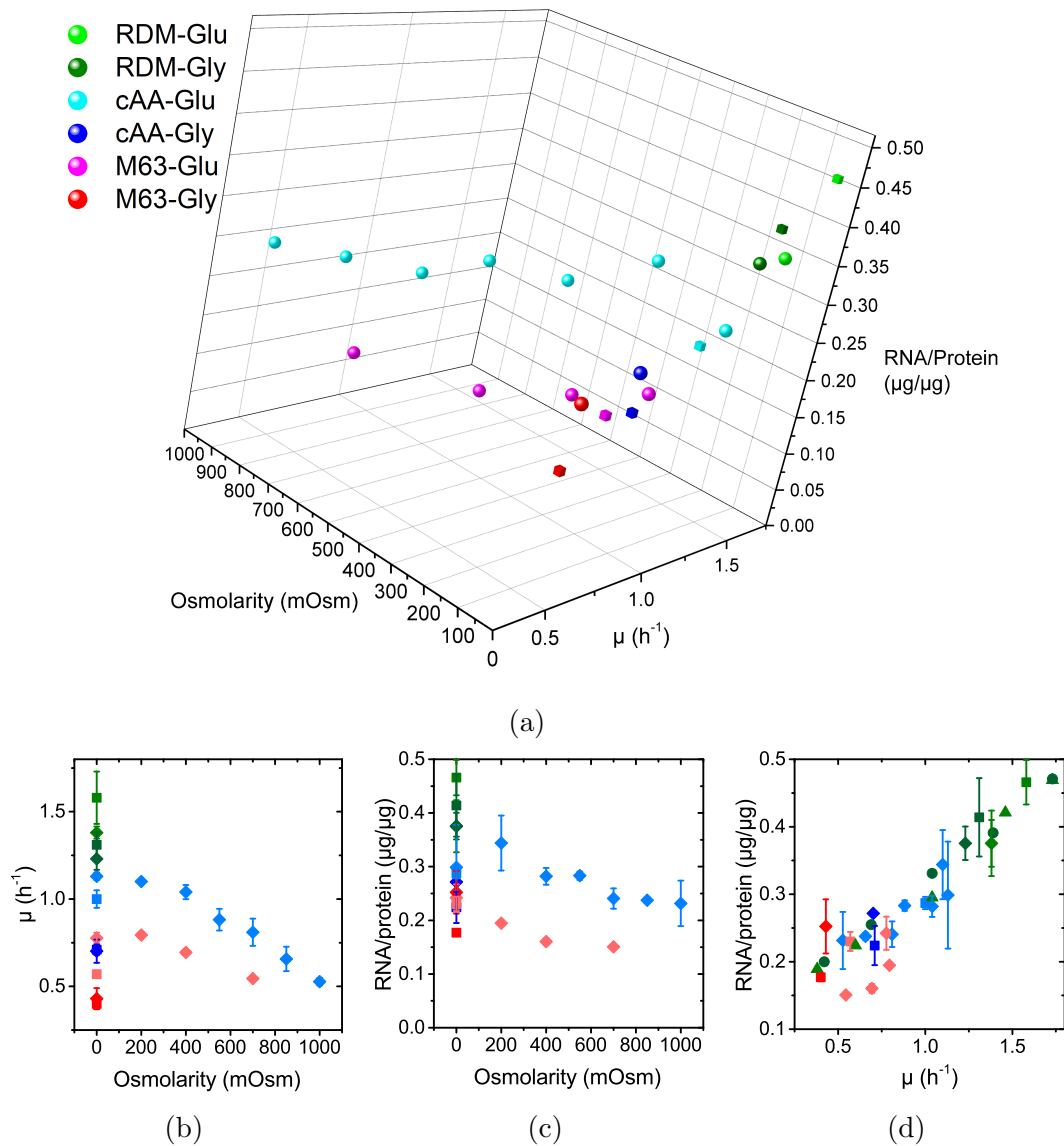


Figure 5.3: The RNA/protein ratio vs growth rate vs added osmolarity for the bacterial cells grown in different nutrient media. Osmolarity was increased by the addition of sucrose to the medium. Colours indicate the medium for both squares and sphere data. Squares: Data from Scott *et al* paper [71] Spheres: data from this thesis. The 0mOsm data is the same data set from 5.2 but error bars are not given for clarity. (b), (c) and (d) contain the projections of the 3D data from (a) along each axis.

5.2 Cell yield at high osmolarity

Another important parameter for the growth of cells at high osmolarity is the efficiency of the cell metabolism; specifically, how many cells you can get for a given amount of nutrients. To measure this I started with the simple concept, that I would grow cells in batch culture and determine the cell concentration at the end of growth phase by counting in the microscope. Unfortunately when attempting to count cells at this point, there was difficulty in determining the cell number accurately, as can be seen in chapter 3.2 Fig.4A where cells continue to divide but smaller when they enter stationary phase.

Instead I chose to perform optical density growth curves, looking for good temporal resolution along the curve so that I can fit to obtain a more accurate asymptote. This can then be converted to a true cell number using the calibration method described in chapter 3.2.

5.2.1 Yield as measured by optical density

I measured the growth curves with the addition of both sucrose and NaCl as shown in Fig.5.4. It should be particularly noted that the measurements given are in osmotic strength and not molarity, i.e. sodium chloride is introduced at half the concentration of sucrose. The growth rates of the curves decrease with increasing osmolarity in the presence of both chemicals as well as demonstrating a greater lag time before both. However it appears that sucrose has a much greater effect on the yield, as the asymptote is almost 50% that of growth at normal osmolarity when grown in the presence of 1000mOsm sucrose. It is worth noting this reduction in asymptote is significant as many experiments are performed at a particular OD, which is usually assumed to correspond to a given stage of growth i.e. mid log. As the asymptote decreases a given OD would correspond to cells at a later stage in growth, where cell size and other cell parameters may differ and could be misinterpreted as effects of high osmolarity. This effect has been noted in the literature such as by Shaevitz and Pilizota, 2014 [36] where they demonstrated the previously observed reduction in cell size at high osmolarity was an artefact of this growth stage shift.

5.2.2 Yield as measured by cell concentration

If you calibrate the data correctly using our method, as I have done in Fig.5.5 you can see that the optical density gives a very misleading appearance of the cell counts. In the media examined, both sodium chloride and sucrose give a similar reduction in cell yield over the osmolarities used, further exemplified in Fig.5.6. The slight increase in yield at 600mOsm is most likely due to the preference of *E.coli* for an osmolarity around 400mOsm, the osmolarity of LB, where our M63 is below optimal osmolarity as a minimal medium.

The decrease in yield indicates an increase in the cost of a producing cell at increasing osmolarities in a manner that is independent of the osmotic agent added. This is unexpected as sucrose and sodium chloride differ in charge, solubility and their membrane permeability and therefore should probably have different

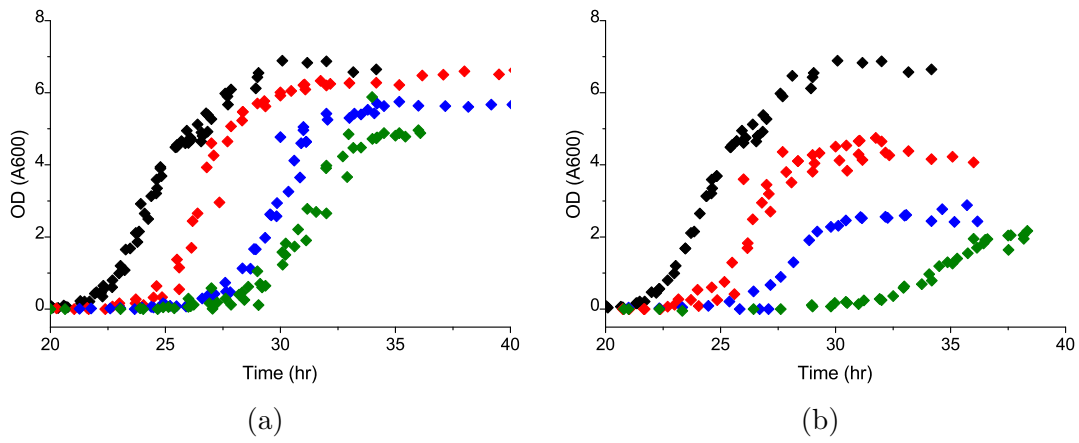


Figure 5.4: Growth curves of BW25113 in M63 with casamino acids and glucose with varying osmolarities of a) Sodium chloride and b) Sucrose. Error bars are not displayed, data is the combined curves of at least 4 separate replicates. Black: normal osmolarity medium; red; 400mOsm added, blue:600mOsm added, green:1000mOsm added

effects on the cell metabolism.

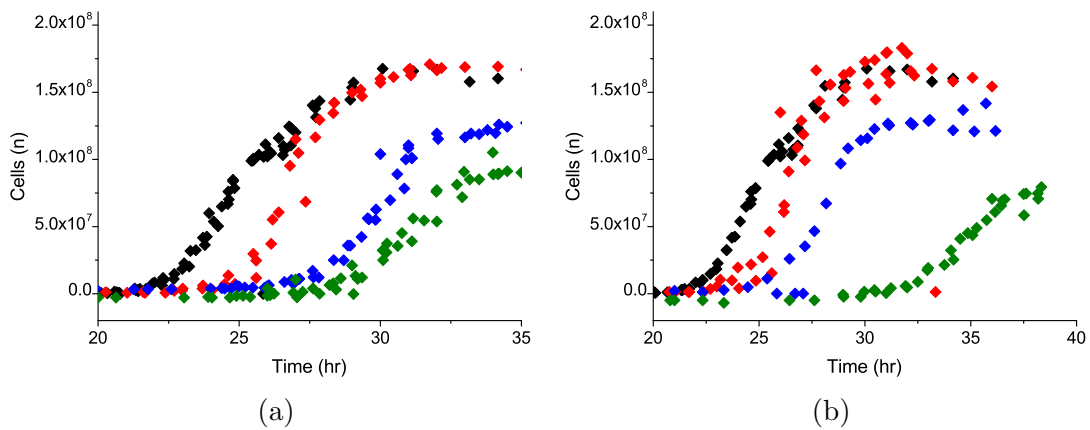


Figure 5.5: Growth curves from Fig.5.4 given now as cell concentrations.

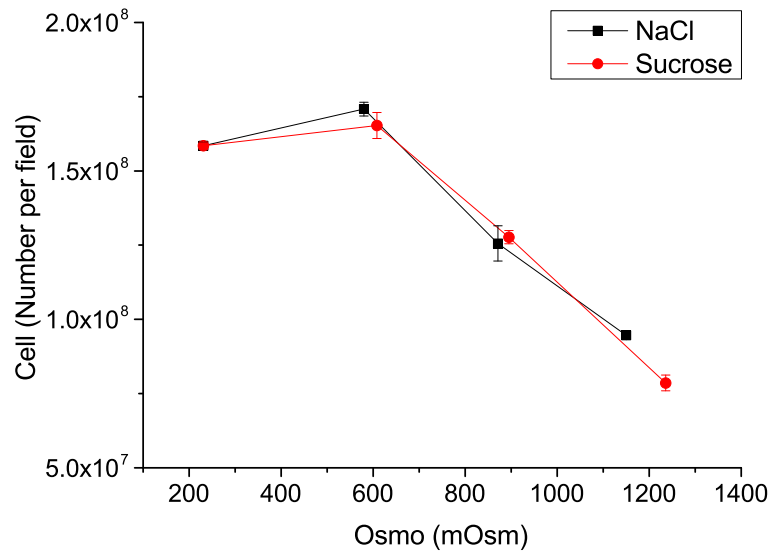


Figure 5.6: The cell concentration given at the asymptote of data in Fig.5.5 vs the measured osmolarity. Data calculated by fitting a modified Gompertz equation [140] to the data in Fig.5.5 and error bars given as the 95% confidence interval of the fit.

5.3 Diffusion constant changes at high osmolarity

The last variable I chose to investigate as a possible cause of reduced growth at high osmolarity was the diffusion constant of particles (such as protein or RNA) within the cytoplasm under steady state growth conditions. To do this I made use of a protein fusion, $\mu NS - GFP$, which is formed from a viral capsid protein attached to a GFP [141]. These proteins, when correctly expressed, form into a single, fluorescent particle within the cell with its size controlled by the expression of protein [109]. Since the intensity of the particle is correlated with the number of GFPs and therefore the intensity can be used as a proxy for particle size. I expressed these particles within the same strain as used in the previous sections, and measured the radius of gyration of particles (described in section 3.1.6 and methods 2.2) in the presence of both sucrose and sodium chloride, the results of which are presented in Fig.5.7. A decrease in the radius of gyration is seen when going from low osmolarity to high osmolarity in the presence of sucrose, where an increase of 1 osmolal decreases the radius by approximately 50%. The radius in sodium chloride however shows significant fluctuation over the range of particle intensities observed. Based on the simulation results in section 3.1.4, further experiments to improve the sample size may change the nature of these trends and therefore the results should be considered preliminary, although potentially interesting, at this stage.

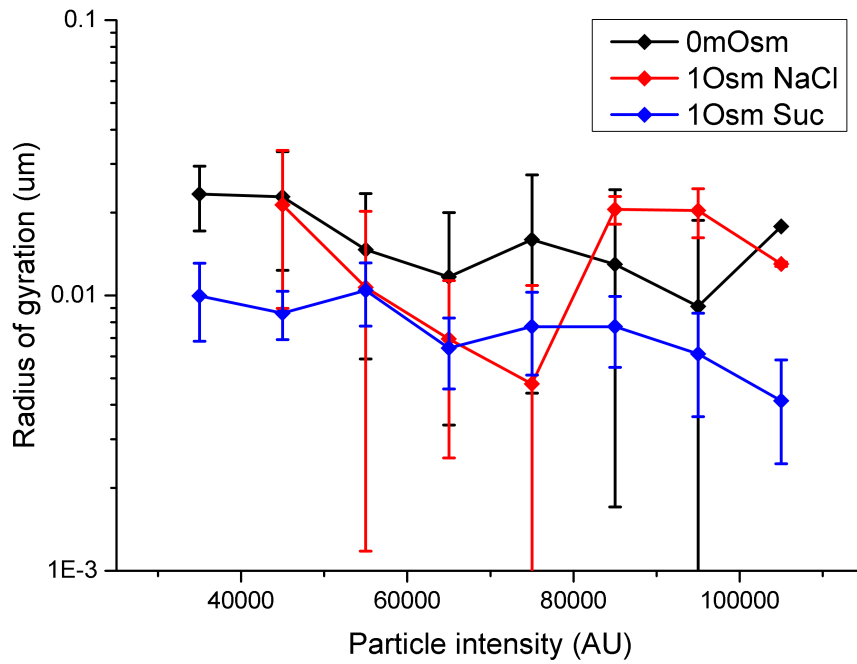


Figure 5.7: Radius of gyration for various intensities of particles in cells grown in M63-Glu-cAA medium. Intensity of particle correlates directly with the particle size and each point represents the mean of between 5 and 10 particles with the bars representing standard error.

5.4 Coarse grained model of growth at high osmolarity

In order to integrate all of my results in a coherent manner, I decided to use a deterministic cell model designed by Weiße *et al* [142] as a basis. This model has a readily present energy variable and the ability to predict changes in the proteome partitioning as a result of actions upon the cell and is therefore of high utility as one of the major findings above is a reduction in cell yield at high osmolarity, indicating a diversion of resources away from growth. To recap, I have seen changes in diffusion constant, cell yield, growth rate and proteome fraction as a result of growth at high osmolarity and thus I need to modify the model to incorporate these different values. Below I have repeated the description of the cell model equations with modifications for osmotic growth indicated in red. For detailed derivation of these different equations see the original paper [142].

5.4.1 Model description

The model uses a single energy variable which is used to drive all reactions within the cell, denoted a , which is produced by converting nutrients, s , to give n_s molecules of a . This a describes all intracellular molecules that can be used for energy and as many molecules can be converted to energy in starvation conditions represents a general metabolite.

Conversion is two step, first the s is transported by a transporter e_t with rate $v_{imp}(e_t, s)$ and then converted to a by a metabolic enzyme e_m with rate $v_{cat}(e_m, s_i)$, where s_i is the internalised s . Finally s_i is diluted by the growth of the cell λs_i , giving the dynamics of s_i as the following:

$$\frac{ds_i}{dt} = v_{imp}(e_t, s) - v_{cat}(e_m, s_i) - \lambda s_i \quad (5.1)$$

The model considers that the only energy consuming reaction is the translation of proteins and that each amino acid added consumes a single a . New proteins are denoted x with total length n_x and are produced at a rate v_x and overall a turnover is given by:

$$\frac{da}{dt} = n_s v_{cat}(e_m, s_i) - v_{osmo}(e_{osmo} v_o) - \sum_x n_x v_x - \lambda a \quad (5.2)$$

Where the sum over x is all types of protein in the cell. Energy is produced by metabolising s_i and is removed by translation and diluted by cell growth. I have modified this equation to include energy consumption by a new class of enzymes representing the osmoregulatory network, e_{osmo} , which consume energy proportional to their number and the energy available to the cell $v_{osmo}(e_{osmo} v_{osmo})$.

Translational elongation rate is given by:

$$v_x = \frac{\gamma(a)}{n_x} c_x \cdot Ok_{tosmo} \quad (5.3)$$

where γ_{max} is the maximal elongation rate, K_γ is energy required to give the half maximal elongation rate and c_x is the number of bound ribosomes transla-

ting mRNA for x . To add osmolarity, the factor k_{tosmo} is added to reduce the translation rate proportional to the osmolarity.

For a given mRNA species x the concentration is given by:

$$\frac{dm_x}{dt} = w_x(a) - k_b m_x r + k_u c_x + v_s - d_m m_x - \lambda m_x \quad (5.4)$$

where it is increased by the transcription $w_x(a)$, and decreased by the rate of degradation, d_m which is assumed equal for all mRNAs. k_b and k_u are the rates of binding and unbinding of ribosomes.

The concentration of bound ribosomes is therefore given as:

$$\frac{dc_x}{dt} = k_b m_x r - k_u c_x - v_x - \lambda c_x \quad (5.5)$$

The model considers only that single ribosome can be bound to a given mRNA at a time, ignoring polysomes, for the sake of simplicity. For free ribosomes the equation is given by:

$$\frac{dr}{dt} = v_r - \lambda r + \sum_x [v_x - k_b m_x r + k_u c_x] \quad (5.6)$$

For all protein fractions, the transcription rate is equal to the following:

$$w_x(a) = \frac{w_x a}{\theta_x + a} \quad (5.7)$$

Where θ is the half maximal transcription rate and w_x is the maximal translation rate. Each θ and w_x is different for each protein fraction reflecting copy number, induction level and length of gene x and are fitted by the model.

For osmoregulatory protein fraction, the transcription rate is for the osmoregulatory protein fraction is proportional to the osmolarity of the medium, O , and some conversion factor K_{osmo} :

$$w_{osmo}(a) = \frac{w_{osmo} a}{\theta_{osmo} + a} O K_{osmo} \quad (5.8)$$

Cell growth is defined as the change of cell mass per time, and the model considers only the proteins as the major contributor to cell growth. At steady state, where cells are growing exponentially the growth rate is therefore:

$$\lambda = \frac{\gamma(a)}{M} \sum_x c_x \quad (5.9)$$

Where M is the mass of a cell in a units or amino acids, which is approximately 10^8 amino acids for *E.coli* and for the sake of simplicity is assumed fixed.

To convert the change in mass to the number of cells, the relevant variable for my experiments, a final equation is used:

$$\frac{dN}{dt} = \lambda N - d_N N \quad (5.10)$$

where the death rate of cells is given by d_N and growth rate obeys eq.5.9.

We used the best fit parameters and rates found by Weiße et al [142], listed in table, based upon single cell measurements of *E.coli* made by Scott et al [71].

Variable	description	default value	unit	source
s	external nutrient	10^4	[moles]	†
d_m	mRNA-degradation rate	0.1	[min ⁻¹]	[143]
n_s	nutrient efficiency	0.5	none	‡
n_r	length of ribosomal proteins	7459	[aa/moles]	[144]
n_x	length of non-ribosomal proteins	300	[aa/moles]	★ [145]
$x \in \{t, m, q, osmo\}$				
γ_{max}	max.transl. elongation rate	1260	[aa/min moles]	†
K_γ	transl. elongation threshold	7	[moles/cell]	§
v_t	max. nutrient import rate	726	[min ⁻¹]	[146]
K_t	max. nutrient import rate	1000	[moles]	
v_m	max. enzymatic rate	5800	[min ⁻¹]	[147]
K_m	enzymatic threshold	1000	[moles/cell]	
w_r	max. ribosome transcription rate	930	[moles/min cell]	§
$w_e = w_t = w_m$	max. enzyme transcription rate	4.14	[moles/min cell]	§
w_q	max. q -transcription rate	948.93	[moles/min cell]	§
θ_r	ribosome transcription threshold	426.87	[moles/cell]	§
θ_{nr}	non-ribosomal transcription threshold	4.38	[moles/cell]	§
K_q	q -autoinhibition threshold	152219	[moles/cell]	§
h_q	q -autoinhibition Hill coeff.	4	none	#
k_b	mRNA-ribosome binding rate	1	[cell/min moles]	*
k_u	mRNA-ribosome unbinding rate	1	[cell/min moles]	
M	total cell mass	10^8	[aa]	◆

Table 5.1: Model parameters. Default values were used except where mentioned. §Parameter optimisation by [142]. †Chosen relative to K_t . ‡chosen such that max growth rate matches that of *E. coli*; ★ *E. coli*'s average; # for steep auto-inhibition; * near the diffusion limit; ◆ order of magnitude; aa denotes number of amino acids

5.4.2 Qualitative testing of model

While constructing the model, I made use of existing data from our plater reader experiments shown in Fig.5.8. It should be noted that the asymptote quoted in the figure is based purely on the optical density of the cells and not cell concentration due to lack of calibration curves for that data. It is also confounded by reduced oxygen in the plater reader and the inclusion of sucrose as the agent for increasing the osmolarity and therefore causes an enhanced reduction in the optical density, and therefore underestimation of yield at high osmolarity.

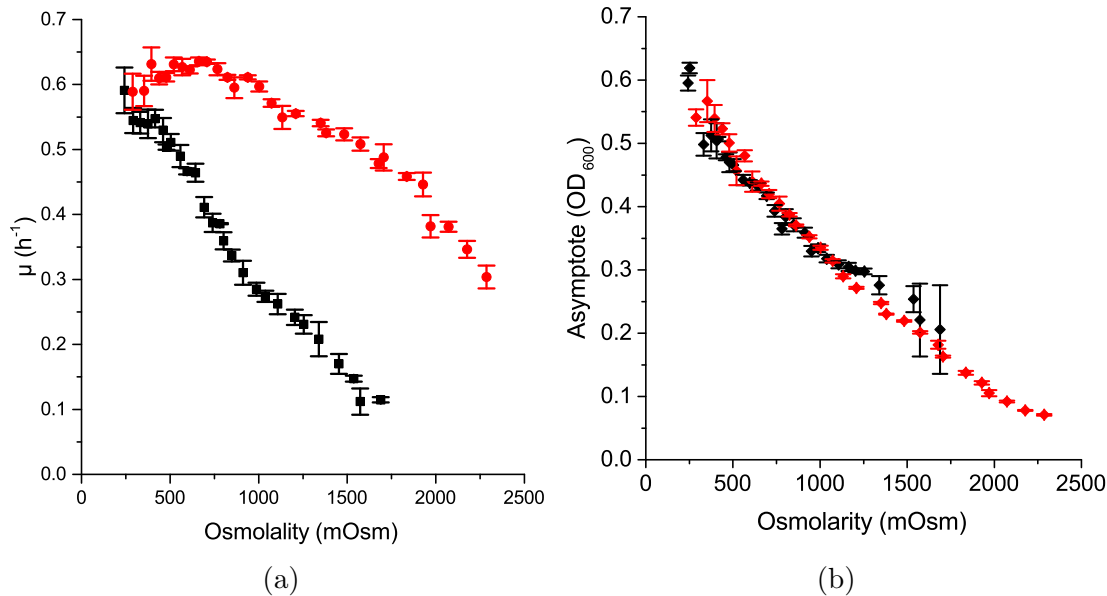


Figure 5.8: Data used for initial testing of the model. Cells grown according to methods 2.1.6 MM9 media with (black) glucose only (red) supplemented with 20 mM glycine betaine and choline (osmolytes).

However, despite these the data was a useful training tool to see if the model could qualitatively reproduce the trends seen before attempting to fit it to greater data sets. To this end I ran the model so that each modified equation could be tested separately as detailed in the table below:

Model name	Details on modifications
Full model	Modifications as above in red for Eq.5.2, Eq.5.3 and Eq.5.8
Energy consumption	Modifications to Eq.5.2: $\frac{da}{dt} = n_s v_{cat}(e_m, s_i) - Ok_{osmo} - \sum_x n_x v_x - \lambda a$
Crowding	Modifications shown in Eq.5.3 only.

Each model type was run for a series of different osmolarities allowing for all the newly added variables to be freely fit while retaining the parameters from the Weiße paper. To perform the fitting a Markov Chain Monte Carlo routine (see section 5.4.3 below) which attempted to fit model results to the data, using

the same fitting routine to analyse both the experimental and model data. This algorithm generated the best fit values for the variables and produced plots for the 50%, 90%, 95% and 99% confidence intervals as shown as the coloured areas in Fig.5.9.

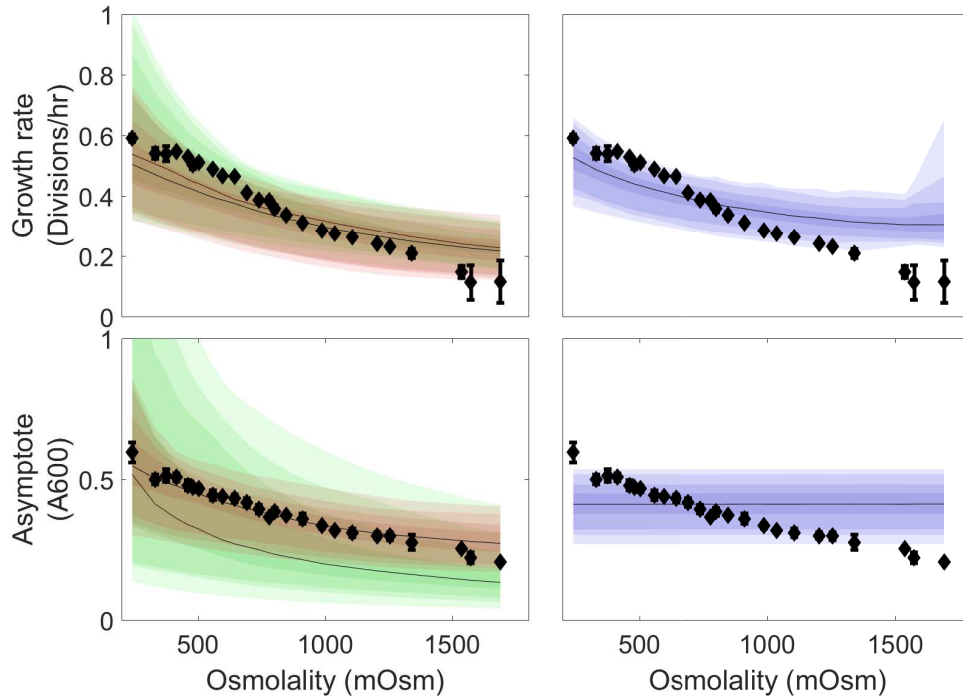


Figure 5.9: Growth rate (top) and Asymptote (bottom) for for simulating three different variants of the model. Brown: Full modification described above. Green: energy consumption. Blue: Crowding, simulated as a reduction in translation. Coloured plots are fitting of a given model variant to the data in the black points (data from Fig.5.8 using the MCMC routine. Bands dark to light, represent the 50, 90, 95 and 99% probabilities.

Based on the plots of the models tested, the full model shows the closest relation to the data, following the trends closely. However, all of the models fail to reproduce the plateau of growth rates in the range of 200-400mOsm media. This is to be expected as ‘normal’ osmolarity for *E.coli* is generally considered to be within this range (according to RDM and LB medium osmolarities) and thus the high osmolarity models may not accurately reflect this region. The diffusion only models do not affect the yield as predicted, as they do not make any modification, either direct or indirect to the cellular energy pool. They also show poor fit even to only the growth rate, indicating that the cells are compensating for the reduction in translation rate, possibly by producing a greater number of ribosomes.

To further understand the relationship between A and GR I introduced osmolytes to the otherwise minimal media, specifically 20mM of glycine betaine and choline Fig.5.8 red data points. As has been previously observed, the addition

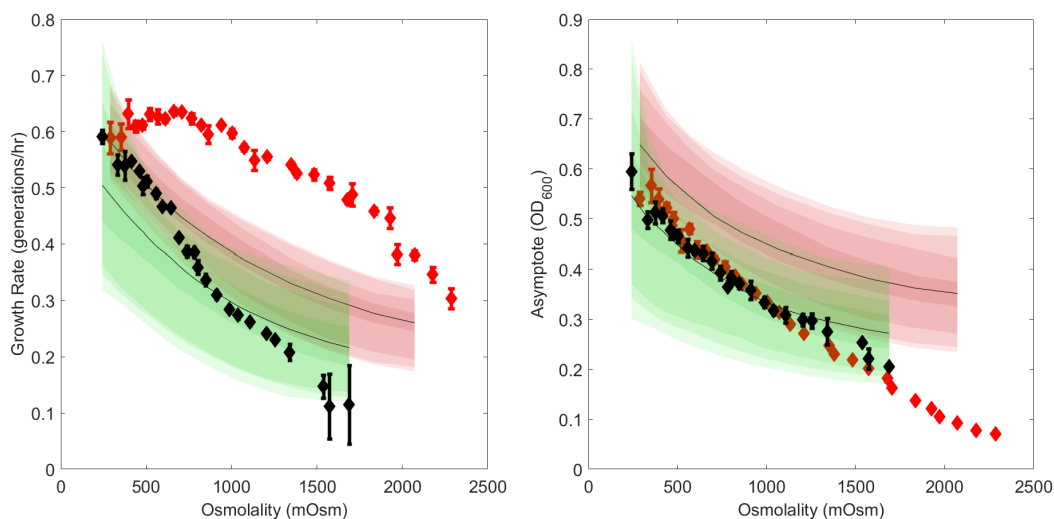


Figure 5.10: Growth rate (left) and Asymptote (right) for minimal media (black) and media supplemented with 20mM glycine betaine and choline (red) (data from Fig.5.8). Model fitted is the full model described above and is fitted to both sets of data simultaneously. Coloured plots are model confidence intervals for each set produced by the model. Bands dark to light, represent the 50, 90, 95 and 99% probabilities.

of the osmolytes increases the growth rates at mid to high osmolarity relative to those without their presence but does not prevent the general decrease of growth rate. Of significance is the lack of a corresponding change in the A of the growth curves in the presence of osmolytes, instead the A values remain almost identical to the minimal medium. This change implies a change growth rate that is not related to changes in yield and hence the inclusion of the diffusion only models in the tests. When the models were applied to both data sets with and without osmolytes, they produced poor results. The areas in Fig.5.10 show the attempted fit of the full model. Despite allowing all the osmotic variables to change between the two media types, along with the n_s parameter, the model fails to reproduce the data and is unable to separate the growth rate from the asymptote to a great enough degree.

5.4.3 Model fitting

The variants of the model were submitted to a MATLAB [148] MCMC routine, found here <http://helios.fmi.fi/~lainema/mcmc/index.html>, which executed optimisation of the available parameters. Parameters already obtained by the original paper were not allowed to vary. I allowed the routine to perform 500 simulations and to provide the sampling data for the 50,90,95 and 99% confidence statistics plotted in the figures. For each model the model was fitted by normalising the first osmolality of the fitted region as 1mOsm to correct for the low osmolality plateau and to prevent calculation errors from zeros. For each osmolality measured, the sum of squares of the experimental to model data was calculated and

used to refine the fitting by the function.

It should be noted that the growth rates calculated for the model and data in Fig.5.8 are not done using the gaussian fitting algorithm [114] used elsewhere in the thesis. Instead, since the model is constructed in MATLAB and that fitting routine is constructed in Python, I use a logistic growth curve model [140] shown in Eq.5.11 and the MATLAB non linear fitting routine. Parameters for fitting were optimised by the robust bi-square method and allowed to run as long as required until the fits converge.

Logistic equation is defined so that variables are biologically relevant where A is the asymptote, λ_m is the max growth rate, l is the lag time and N is the number of cells:

$$N = A \cdot \exp\left(-\exp\left(\frac{\lambda_m e}{A}(l - t) + 1\right)\right) \quad (5.11)$$

5.5 Discussion

In the previous chapter, I have explored the reasons for reduction in growth at high osmolarity through the measurement of the proteome, yield and cytoplasmic diffusion constant. I aimed to improve the understanding of changes to growth at high osmolarity in order to be able to compensate for negative side effects of using the osmoregulatory network in improving ethanol tolerance so as to not affect the ethanol production rates. This understanding would also assist the field in general and my lab in particular as we aim to understand the energetics of bacterial growth to a greater degree through pH and proton motive force measurements.

The yield, section 5.2, showed some surprising results with sucrose and NaCl showing the same reduction in yield despite their difference in molecular weight, charge and capacity to pass through the plasma membrane. It also demonstrated that with the addition of 1M of either substance to the solution, the cost of producing a cell increased by almost 50%.

When studying the proteome fraction at increasing osmolarities, I observed two different trends depending on the media used. When osmolytes in the form of casamino acids are present, the RNA/protein ration decreases along the linear relationship defined by Scott *et al.* [71] in equation 1.1. Without osmolytes present, the trend deviated heavily below this line. This is opposite to the relationship seen in their follow-up paper [149] and Fig.1.6B where the RNA/protein ratio rises above the line of nutrient limitation with increasing osmolarity. In that paper they grow cells in minimal media with glucose and increase the osmolarity with NaCl and explain this relationship by showing that ribosomes are inactivated by osmolarity and the translational elongation rate is reduced. In my case I use sucrose to increase the osmolarity, and use both minimal media and media with osmolytes which may go some way to explaining this difference in trends. With the use of the model in future, I hope to test this hypothesis using both sets of data to inform the fit.

Finally, I measure the diffusion constant of μ NS-GFP particles within the cytoplasm of *E. coli* and find different trends in both sucrose and NaCl. In NaCl the middle range particles show a decrease in radius of gyration with large and small particles similar to the normal osmolarity. For sucrose the trend is consistently below the wildtype. All datapoints have a fairly large error due to the low number of samples and inherent distribution in particle sizes and stochastic nature of the motion. If these trends are real, then it may go some way to explaining the difference in RNA/protein measurements above, as sucrose and NaCl affect the diffusion and therefore the rates of chemical reactions differently.

Chapter 6

Discussion and future work

6.1 Improving ethanol tolerance

Ethanol and osmolarity have a number of similar effects on the cell membrane and protein stability. The aim of this thesis was to attempt to use knowledge of the osmoregulation network of *E. coli* to attempt to improve the ethanol tolerance of bacteria.

I investigated how varying conditions of growth would affect the ethanol tolerance of *E. coli*, focussing primarily on trying to change the conditions that the bacteria were grown in. I found that addition of osmolytes to minimal medium did not make give significant improvements to ethanol tolerance, nor did increasing the concentration of normal components of LB. Increasing the osmolarity of the medium led to a decrease in tolerance to ethanol most likely due to the combination of stresses upon the cell.

One mechanism we found that could improve the tolerance of bacteria was a reduction in the temperature at which the cells were grown. While this does decrease the growth rate, it does improve the tolerance significantly with an increase from 5.75% to 7.75% with a reduction from 37 °C to 25 °C. This effect is likely due to the effect of increased membrane and protein stability with a reduction in temperature [85, 101]

I also explored the importance of osmoregulatory components for ethanol tolerance by exposing single gene knockouts to various concentrations of ethanol. The proW gene, a subcomponent of the proU transport system, showed a link to ethanol tolerance with the mutant having a significantly reduced tolerance with a reduction of 2.5% compared to wildtype *E. coli*. This would suggest that glycine betaine provides protection to ethanol, however, supplementing the media with glycine betaine as in chapter 2.5 did not help with tolerance. Its possible another substrate of the transport system is required for resistance, such as ectoine or proline betaine. It is unclear however, how much of these compounds is present in the LB that the bacteria were growing in [62]. Based on this future work should start by probing the other components of the ProU transport system to see if they also had a link with ethanol tolerance as well as trying other osmolytes of ectoine or proline betaine.

In addition the model of industrial bio-production of ethanol detailed in chap-

ter 4.1 provides a simple yet useful way of converting any improvement to a monetary value when used in the industrial process. Furthermore I suggest that evolving strains of *E.coli* at high osmolarity may yield improved ethanol tolerance through some of the cross-talk of the osmoregulatory systems to ethanol tolerance.

6.2 *E.coli* physiology at high osmolarity

The most interesting result of this thesis is the quantification of the reduction in yield that occurs at high osmolarity, with an approximately 50% yield reduction with the addition of 1000mOsm sucrose to the medium and a similar value for NaCl. This has not been reported much in the literature but is somewhat expected due to the energy consuming nature of the osmoregulatory network. What is unusual is the magnitude of the cost of growth, being significant enough to double the cost of producing a single *E.coli cell*.

I also saw changes to the proteome fraction and diffusion constants, however there is some contradiction with existing literature in the trends obtained. It remains to be seen if the trends will be borne out with further sampling. Assuming the trends are real then they suggest that the media and the osmotic agent have a significant effect on the proteome fraction as we obtained two different trends with and without cassamino acids and both trends differ from the measurements by Scott *et al.* [71].

The coarse grained model presented in chapter 5.4 may offer some explanation if all of the data is integrated into it. However, the qualitative fitting attempts demonstrate that the model currently lacks the capacity to fit minimal and rich media using the current parameters and as such requires some further modification.

6.3 Future directions

To enhance further experiments or measurements for diffusion constants at high osmolarity, a new piece of imaging equipment would be useful; a Single Photon Avalanche Diode. This would allow much faster imaging than is currently possible in our setup, eliminating the underestimation of diffusion constant present in current data.

In addition when combined with the confinement model in chapter 3.1, it could be possible to simulate confined diffusion in subcellular compartments using the saturation of mean square displacement as an indicator of the effective volume the particle is moving within in a manner similar to [150]. The subcellular compartments are theorised by Poolman *et al.* [83, 151] to be formed during high osmolarity, accounting for lower crowding of smaller proteins but the apparent slowdown of diffusion of larger particles seen here and in the Dai *et al.* study [70].

Bibliography

- [1] J.R. Moreira. Water Use and Impacts Due Ethanol Production in Brazil. In *Proc. Linkages between Energy Water Manag. Agric. Dev. Countries. Hyderabad, India, January 29– 30, 2007*, page 24, 2007.
- [2] Max Nelson. *The barbarian’s beverage: A history of beer in ancient Europe*. Taylor & Francis, Abingdon, UK, feb 2005.
- [3] Hyunok Lee, Joseph W. Glauber, and Daniel A. Sumner. Increased Industrial Uses of Agricultural Commodities Policy, Trade and Ethanol. *Contemp. Econ. Policy*, 12(3):22–32, jul 1994.
- [4] Kristina J. Anderson-Teixeira, Sarah C. Davis, Michael D. Masters, and Evan H. Delucia. Changes in soil organic carbon under biofuel crops. *GCB Bioenergy*, 1(1):75–96, feb 2009.
- [5] Sujit K. Mohanty and Manas R. Swain. Bioethanol Production From Corn and Wheat: Food, Fuel, and Future. In *Bioethanol Prod. from Food Crop.*, pages 45–59. Academic Press, jan 2018.
- [6] Günther Reuss, Walter Disteldorf, Armin Otto Gamer, and Albrecht Hilt. Ullmann’s Encyclopedia of Industrial Chemistry: Formaldehyde. *Ullmann’s Encycl. iIndustrial Chem.*, 15:735–768, jun 2012.
- [7] Haythem Latif, Ahmad A Zeidan, Alex T Nielsen, and Karsten Zengler. Trash to treasure: production of biofuels and commodity chemicals via syngas fermenting microorganisms. *Curr. Opin. Biotechnol.*, 27:79–87, jun 2014.
- [8] Albara Mustafa, Rajnish Kaur Calay, and Mohamad Y. Mustafa. A Techno-economic Study of a Biomass Gasification Plant for the Production of Transport Biofuel for Small Communities. In *Energy Procedia*, volume 112, pages 529–536. Elsevier, mar 2017.
- [9] Rostyslav Kravchuk. *Modelling and simulation of syngas fermentation for the production of biofuels precursors*. PhD thesis, The University College of Southeast Norway, 2017.
- [10] C.R. South, D.A.L. Hogsett, and L.R. Lynd. Modeling simultaneous saccharification and fermentation of lignocellulose to ethanol in batch and continuous reactors. *Enzyme Microb. Technol.*, 17(9):797–803, sep 1995.

- [11] A. Aden, M. Ruth, K. Ibsen, J. Jechura, K. Neeves, J. Sheehan, B. Wallace, L. Montague, A. Slayton, and J. Lukas. Lignocellulosic Biomass to Ethanol Process Design and Economics Utilizing Co-Current Dilute Acid Prehydrolysis and Enzymatic Hydrolysis for Corn Stover. Technical report, 2002.
- [12] Ricardo Morales-Rodriguez, Anne S. Meyer, Krist V. Gernaey, and Gürkan Sin. Dynamic model-based evaluation of process configurations for integrated operation of hydrolysis and co-fermentation for bioethanol production from lignocellulose. *Bioresour. Technol.*, 102(2):1174–1184, 2011.
- [13] Junling Guo, Miguel Suástegui, Kelsey K. Sakimoto, Vanessa M. Moody, Gao Xiao, Daniel G. Nocera, and Neel S. Joshi. Light-driven fine chemical production in yeast biohybrids. *Science*, 362(6416):813–816, 2018.
- [14] Mohammad J Taherzadeh and Keikhosro Karimi. Pretreatment of lignocellulosic wastes to improve ethanol and biogas production: A review, 2008.
- [15] Frank R. Bengelsdorf, Melanie Straub, and Peter Dürre. Bacterial synthesis gas (syngas) fermentation. *Environ. Technol. (United Kingdom)*, 34(13-14):1639–1651, jul 2013.
- [16] Reinhard Rauch, Jitka Hrbek, and Hermann Hofbauer. Biomass Gasification for Synthesis Gas Production and Applications of the Syngas. In *Adv. Bioenergy Sustain. Chall.*, volume 3, pages 73–91. John Wiley & Sons, Ltd, jul 2015.
- [17] G Maschio, A Lucchesi, and G Stoppato. Production of syngas from biomass. *Bioresour. Technol.*, 48(2):119–126, 1994.
- [18] Ching-Whan; Ko, Michael Sean Slape, Peter S; Bell, and Kim Ocfemia. Method of Operation Of Process To Produce Syngas From Carbonaceous Material, 2014.
- [19] Donghai Mei, Roger Rousseau, Shawn M Kathmann, Vassiliki-Alexandra Glezakou, Mark H Engelhard, Weilin Jiang, Chongmin Wang, Mark A Gerber, James F White, and Don J Stevens. Ethanol synthesis from syngas over Rh-based/SiO₂ catalysts: A combined experimental and theoretical modeling study. *J. Catal.*, 271(2):325–342, may 2010.
- [20] G Vanderlee. On the selectivity of Rh catalysts in the formation of oxygenates. *J. Catal.*, 98(2):522–529, apr 1986.
- [21] Madan M Bhasin. Importance of surface science and fundamental studies in heterogeneous catalysis. *Catal. Letters*, 59:1–7, 1999.
- [22] James Daniell, Michael Köpke, and Séan Simpson. Commercial Biomass Syngas Fermentation. *Energies*, 5(12):5372–5417, dec 2012.

- [23] R S Tanner, Letrisa M Miller, and D Yang. *Clostridium ljungdahlii* sp-Nov, an acetogenic species in clostridial ribosomal-RNA homology Group-I. *Int. J. Syst. Bacteriol.*, 43(2):232–236, 1993.
- [24] Ghasem D. Najafpour, Mohamad Hekarl Uzir, Habibollah Younesi, Maedeh Mohammadi, and Abdul Rahman Mohamed. Kinetic Studies on Fermentative Production of Biofuel from Synthesis Gas Using *Clostridium ljungdahlii*. *Sci. World J.*, 2014(1):1–8, 2014.
- [25] Habibollah Younesi, Ghasem Najafpour, and Abdul Rahman Mohamed. Ethanol and acetate production from synthesis gas via fermentation processes using anaerobic bacterium, *Clostridium ljungdahlii*. *Biochem. Eng. J.*, 27:110–119, 2005.
- [26] Easyg Llc Evans, T.C., Gavrilovich, E., Mihai, R.C. and Isbasescu, I., Darryl Thelen, J A Martin, S M Allen, and Slane SA. Process for Fermenting Co-Containing Gaseous Substrates, 2014.
- [27] Ineos, Grangemouth, About.
- [28] Scott Syrona, Ryan Senaratne, and Ching-whan Ko. Syngas Fermentation Process and Medium, nov 2013.
- [29] Marshall D. Bredwell, Prashant Srivastava, and R. Mark Worden. Reactor design issues for synthesis-gas fermentations. *Biotechnol. Prog.*, 15(5):834–844, oct 1999.
- [30] Eric Kvaalen, Philip C. Wankat, and Bruce A. McKenzie. AE-117.
- [31] Clark Shove Robinson and Edwin Richard Gilliland. *Elements of Fractional Distillation*. McGraw-Hill Book Company, Inc., New York, fourth edition, 1950.
- [32] Stephen T. Jones, Roger A. Korus, Wudneh Admassu, and Richard C. Heimsch. Ethanol fermentation in a continuous tower fermentor. *Biotechnol. Bioeng.*, 26(7):742–747, jul 1984.
- [33] P W Madson. Ethanol distillation: the fundamentals. *alcohol Textb.*, pages 319–336, 2003.
- [34] M. A.S.S. Ravagnani, M. H.M. Reis, R. Maciel Filho, and M. R. Wolf-Maciel. Anhydrous ethanol production by extractive distillation: A solvent case study. *Process Saf. Environ. Prot.*, 88(1):67–73, jan 2010.
- [35] Gert-Jan A. F. Fien and Y. A. Liu. Heuristic Synthesis and Shortcut Design of Separation Processes Using Residue Curve Maps: A Review. *Ind. Eng. Chem. Res.*, 33(11):2505–2522, nov 1994.
- [36] Teuta Pilizota and Joshua W. Shaevitz. Origins of *Escherichia coli* growth rate and cell shape changes at high external osmolality. *Biophys. J.*, 107(8):1962–9, oct 2014.

- [37] Enrique R Rojas and Kerwyn Casey Huang. Regulation of microbial growth by turgor pressure. *Curr. Opin. Microbiol.*, 42:62–70, apr 2018.
- [38] D S Cayley, Harry J. Guttman, M T Record, D. Scott Cayley, Harry J. Guttman, and M. Thomas Record. Biophysical Characterization of Changes in Amounts and Activity of *Escherichia coli* Cell and Compartment Water and Turgor Pressure in Response to Osmotic Stress. *Biophys. J.*, 78(4):1748–1764, 2000.
- [39] Scott Cayley, Barbara A. Lewis, Harry J. Guttman, and M. Thomas Record. Characterization of the cytoplasm of *Escherichia coli* K-12 as a function of external osmolarity. Implications for protein-DNA interactions in vivo. *J. Mol. Biol.*, 222(2):281–300, 1991.
- [40] Yi Deng, Mingzhai Sun, and Joshua W Shaevitz. Direct measurement of cell wall stress stiffening and turgor pressure in live bacterial cells. *Phys. Rev. Lett.*, 107(15), 2011.
- [41] L N Csonka and Andrew D Hanson. Prokaryotic osmoregulation: genetics and physiology. *Annu. Rev. Microbiol.*, 45(1):569–606, oct 1991.
- [42] Susanne Morbach and Reinhard Krämer. Body shaping under water stress: Osmosensing and osmoregulation of solute transport in bacteria. *ChemBioChem*, 3(5):384–397, 2002.
- [43] W. W. Baldwin, R. Myer, T. Kung, E. Anderson, and A. L. Koch. Growth and buoyant density of *Escherichia coli* at very low osmolarities. *J. Bacteriol.*, 177(1):235–237, 1995.
- [44] M. Thomas Record, Elizabeth S. Courtenay, D. Scott Cayley, and Harry J. Guttman. Responses of *E. coli* to osmotic stress: Large changes in amounts of cytoplasmic solutes and water. *Trends Biochem. Sci.*, 23(4):143–148, 1998.
- [45] Janet M. Wood. Bacterial responses to osmotic challenges. *J. Gen. Physiol.*, 145(5):381–388, may 2015.
- [46] Teuta Pilizota and Joshua W. Shaevitz. Fast, multiphase volume adaptation to hyperosmotic shock by *Escherichia coli*. *PLoS One*, 7(4):1–10, 2012.
- [47] Wolfgang Epstein. Osmoregulation by potassium transport in *Escherichia coli*. *FEMS Microbiol. Rev.*, 2(1-2):73–78, 1986.
- [48] D McLaggan, T M Logan, D G Lynn, and W Epstein. Involvement of gamma-glutamyl peptides in osmoadaptation of *Escherichia coli*. *J. Bacteriol.*, 172(7):3631–6, jul 1990.
- [49] D. C. Dosch, G. L. Helmer, S. H. Sutton, F. F. Salvacion, and W. Epstein. Genetic analysis of potassium transport loci in *Escherichia coli*: Evidence for three constitutive systems mediating uptake of potassium. *J. Bacteriol.*, 173(2):687–696, 1991.

- [50] D. B. Rhoads. Cation transport in *Escherichia coli*. VIII. Potassium transport mutants. *J. Gen. Physiol.*, 67(3):325–341, 1976.
- [51] L M Stewart, E P Bakker, and I R Booth. Energy coupling to K⁺ uptake via the Trk system in *Escherichia coli*: the role of ATP. *J. Gen. Microbiol.*, 131(1):77–85, 1985.
- [52] Anand Ballal, Bhakti Basu, and Shree Kumar Apte. The Kdp-ATPase system and its regulation. *J. Biosci.*, 32(3):559–568, 2007.
- [53] Janet M Wood. Osmosensing by Bacteria. *Sci. Signal.*, 2006(357):pe43, 2006.
- [54] Doreen E. Culham, James Henderson, Rebecca A. Crane, and Janet M. Wood. Osmosensor ProP of *Escherichia coli* responds to the concentration, chemistry, and molecular size of osmolytes in the proteoliposome lumen. *Biochemistry*, 42(2):410–420, 2003.
- [55] A R Strøm and I Kaasen. Trehalose metabolism in *Escherichia coli*: stress protection and stress regulation of gene expression. *Mol. Microbiol.*, 8(2):205–210, 1993.
- [56] D T Welsh, R H Reed, and R a Herbert. The role of trehalose in the osmoadaptation of *Escherichia coli* NCIB 9484: interaction of trehalose, K⁺ and glutamate during osmoadaptation in continuous culture. *J. Gen. Microbiol.*, 137(4):745–750, 1991.
- [57] E. N. Miller and L. O. Ingram. Combined effect of betaine and trehalose on osmotic tolerance of *Escherichia coli* in mineral salts medium. *Biotechnol. Lett.*, 29(2):213–217, 2007.
- [58] A. L. Koch, M. L. Higgins, and R. J. Doyle. The Role of Surface Stress in the Morphology of Microbes. *Microbiology*, 128(5):927–945, 1982.
- [59] Hongyuan Jiang and Sean X Sun. Morphology, growth, and size limit of bacterial cells. *Phys. Rev. Lett.*, 105(2), 2010.
- [60] Enrique Rojas, Julie a Theriot, and Kerwyn Casey Huang. Response of *Escherichia coli* growth rate to osmotic shock. *Proc. Natl. Acad. Sci. U. S. A.*, 111(21):7807–12, 2014.
- [61] Enrique Rojas, Julie a Theriot, and Kerwyn Casey Huang. Response of *Escherichia coli* growth rate to osmotic shock.-SI. *Proc. Natl. Acad. Sci. U. S. A.*, 111(21):7807–12, may 2014.
- [62] Guennadi Sezonov, Danièle Joseleau-Petit, and Richard D’Ari. *Escherichia coli* physiology in Luria-Bertani broth. *J. Bacteriol.*, 189(23):8746–8749, 2007.
- [63] D B Rhoads and W Epstein. Energy coupling to net K⁺ transport in *Escherichia coli* K-12. *J. Biol. Chem.*, 252(4):1394–1401, 1977.

- [64] Susan V. MacMillan, David A. Alexander, Doreen E. Culham, H. Jörg Kunte, Emmalee V. Marshall, Denis Rochon, and Janet M. Wood. The ion coupling and organic substrate specificities of osmoregulatory transporter ProP in *Escherichia coli*. *Biochim. Biophys. Acta - Biomembr.*, 1420(1-2):30–44, 1999.
- [65] Bruce Alberts, Alexander Johnson, Julian Lewis, David Morgan, Martin Raff, Keith Roberts, and Peter Walter. *Molecular Biology of the Cell*. Garland Science, aug 2017.
- [66] J. E. Purvis, L. P. Yomano, and L. O. Ingram. Enhanced trehalose production improves growth of *Escherichia coli* under osmotic stress. *Appl. Environ. Microbiol.*, 71(7):3761–3769, jul 2005.
- [67] M. O. Walderhaug, J. W. Polarek, P. Voelkner, J. M. Daniel, J. E. Hesse, K. Altendorf, and W. Epstein. KdpD and KdpE, proteins that control expression of the kdpABC operon, are members of the two-component sensor-effector class of regulators. *J. Bacteriol.*, 174(7):2152–2159, 1992.
- [68] K. I. Racher, R. T. Voegelé, E. V. Marshall, D. E. Culham, J. M. Wood, H. Jung, M. Bacon, M. T. Cairns, S. M. Ferguson, W. J. Liang, P. J F Henderson, G. White, and F. R. Hallett. Purification and reconstitution of an osmosensor: Transporter ProP of *Escherichia coli* senses and responds to osmotic shifts. *Biochemistry*, 38(6):1676–1684, feb 1999.
- [69] Matthew Scott, Carl W. Gunderson, Eduard M. Mateescu, Zhongge Zhang, and Terence Hwa. Interdependence of cell growth and gene expression: Origins and consequences. *Science (80-.)*, 330(6007):1099–1102, 2010.
- [70] Xiongfeng Dai, Manlu Zhu, Mya Warren, Rohan Balakrishnan, Hiroyuki Okano, James R. Williamson, Kurt Fredrick, and Terence Hwa. Slowdown of Translational Elongation in *Escherichia coli* under Hyperosmotic Stress. *MBio*, 9(1):93, feb 2018.
- [71] Matthew Scott, Eduard M Mateescu, Zhongge Zhang, and Terence Hwa. Interdependence of Cell Growth Origins and Consequences. *Science (80-.)*, 330(November):1099–1102, 2010.
- [72] Hans Bremer and Patrick P Dennis. Modulation of Chemical Composition and Other Parameters of the Cell by Growth Rate. *Escherichia coli Salmonella Cell. Mol. Biol.*, 2009.
- [73] Jes Forchhammer and Lasse Lindahl. Growth rate of polypeptide chains as a function of the cell growth rate in a mutant of *Escherichia coli* 15. *J. Mol. Biol.*, 55(3):563–568, 1971.
- [74] R. Mikkola and C. G. Kurland. Evidence for demand-regulation of ribosome accumulation in *E. coli*. *Biochimie*, 73(12):1551–1556, dec 1991.

- [75] T Ruusala, D Andersson, M Ehrenberg, and C.G. Kurland. Hyper-accurate ribosomes inhibit growth. *EMBO J.*, 3(11):2575–2580, 1984.
- [76] Jacek T Mika and Bert Poolman. Macromolecule diffusion and confinement in prokaryotic cells. *Curr. Opin. Biotechnol.*, 22(1):117–126, feb 2011.
- [77] Jacek T. Mika, Geert Van Den Bogaart, Liesbeth Veenhoff, Victor Krasnikov, and Bert Poolman. Molecular sieving properties of the cytoplasm of *Escherichia coli* and consequences of osmotic stress. *Mol. Microbiol.*, 77(1):200–207, jul 2010.
- [78] Johan Elf, Gene Wei Li, and X Sunney Xie. Probing transcription factor dynamics at the single-molecule level in a living cell. *Science (80-.)*, 316(5828):1191–1194, may 2007.
- [79] Michael C Konopka, Irina A Shkel, Scott Cayley, M Thomas Record, and James C Weisshaar. Crowding and confinement effects on protein diffusion in vivo. *J. Bacteriol.*, 188(17):6115–6123, 2006.
- [80] Michael B Elowitz, Michael G Surette, † Pierre-Etienne Wolf, Jeffry B Stock, and Stanislas Leibler. Protein Mobility in the Cytoplasm of *Escherichia coli*. Technical Report 1, 1999.
- [81] Somenath Bakshi, Albert Siryaporn, Mark Goulian, and James C Weisshaar. Superresolution imaging of ribosomes and RNA polymerase in live *Escherichia coli* cells. *Mol. Microbiol.*, 85(1):21–38, jul 2012.
- [82] Anja Nenninger, Giulia Mastroianni, and Conrad W Mullineaux. Size dependence of protein diffusion in the cytoplasm of *Escherichia coli*. *J. Bacteriol.*, 192(18):4535–4540, sep 2010.
- [83] Boqun Liu, Zariif Hasrat, Bert Poolman, and Arnold J Boersma. Decreased Effective Macromolecular Crowding in *Escherichia coli* Adapted to Hyperosmotic Stress. *J. Bacteriol.*, 201(10), 2019.
- [84] Xiongfeng Dai, Manlu Zhu, Mya Warren, Rohan Balakrishnan, Vadim Pat-salo, Hiroyuki Okano, James R. Williamson, Kurt Fredrick, Yi Ping Wang, and Terence Hwa. Reduction of translating ribosomes enables *Escherichia coli* to maintain elongation rates during slow growth. *Nat. Microbiol.*, 2:16231, 2016.
- [85] K. M. Dombek and L. O. Ingram. Effects of ethanol on the *Escherichia coli* plasma membrane. *J. Bacteriol.*, 157(1):233–239, 1984.
- [86] L. O. Osman, Y. A. and Ingram. Mechanism of alcohol inhibition of fermentation in *Zymomonas mobilis* strain CP4. *J. Bacteriol.*, 164(1):164–175, oct 1985.
- [87] Lonnie O. Ingram. Ethanol Tolerance in Bacteria. *Crit. Rev. Biotechnol.*, 9(4):305–319, jan 1989.

- [88] Sonja Isken and Jan A M De Bont. Bacteria tolerant to organic solvents. *Extremophiles*, 2(3):229–238, 1998.
- [89] Ján Šajbidor. Effect of some environmental factors on the content and composition of microbial membrane lipids. *Crit. Rev. Biotechnol.*, 17(2):87–103, 1997.
- [90] Daniel C Sévin and Uwe Sauer. Ubiquinone accumulation improves osmotic-stress tolerance in *Escherichia coli*. *Nat. Chem. Biol.*, 10(4):266–72, 2014.
- [91] W. Epstein. Cation Transport in *Escherichia coli*: V. Regulation of cation content. *J. Gen. Physiol.*, 49(2):221–234, 1965.
- [92] D. B. Rhoads and W Epstein. Cation transport in *Escherichia coli*. IX. Regulation of K transport. *J. Gen. Physiol.*, 72(3):283–95, sep 1978.
- [93] B. Perroud and D. Le Rudulier. Glycine betaine transport in *Escherichia coli*: Osmotic modulation. *J. Bacteriol.*, 161(1):393–401, 1985.
- [94] Escherichia K, Mary E Stalmach, Suzanne Grothe, and Janet M Wood. Two proline porters in Two Proline Porters in *Escherichia coli* K-12. *J. Bacteriol.*, 156(2):481–6, nov 1983.
- [95] Hung V Ly and Marjorie L Longo. The influence of short-chain alcohols on interfacial tension, mechanical properties, area/molecule, and permeability of fluid lipid bilayers. *Biophys. J.*, 87(2):1013–1033, 2004.
- [96] Albert Leo, Corwin Hansch, and David Elkins. Partition coefficients and their uses. *Chem. Rev.*, 71(6):525–616, 1971.
- [97] Y Hatefi and W G Hanstein. Destabilization of membranes with chaotropic ions. *Methods Enzymol.*, 31:770–90, 1974.
- [98] J Y Maillard. Bacterial target sites for biocide action. *Symp. Ser. Soc. Appl. Microbiol.*, 92(31):16S–27S, 2002.
- [99] Paul H Yancey. Organic osmolytes as compatible, metabolic and counteracting cytoprotectants in high osmolarity and other stresses. *J. Exp. Biol.*, 208(Pt 15):2819–2830, 2005.
- [100] Youxing Qu, C. L. Bolen, and D W Bolen. Osmolyte-driven contraction of a random coil protein. *Proc. Natl. Acad. Sci.*, 95(16):9268–9273, aug 2002.
- [101] S. C. Hand and G. N. Somero. Urea and methylamine effects on rabbit muscle phosphofructokinase. Catalytic stability and aggregation state as a function of pH and temperature. *J. Biol. Chem.*, 257(2):734–741, 1982.
- [102] Teresa Caldas, Nathalie Demont-Caulet, Alexandre Ghazi, and Gilbert Richarme. Thermoprotection by glycine betaine and choline. *Microbiology*, 145(9):2543–2548, 1999.

- [103] Jiang Hong, Lila M. Gierasch, and Zhicheng Liu. Its Preferential Interactions with Biopolymers Account for Diverse Observed Effects of Trehalose. *Biophys. J.*, 109(1):144–153, 2015.
- [104] J L Milner, D J McClellan, and J M Wood. Factors reducing and promoting the effectiveness of proline as an osmoprotectant in *Escherichia coli* K12. *J. Gen. Microbiol.*, 133(7):1851–60, 1987.
- [105] M Jebbar, R Talibart, K Gloux, T Bernard, and C Blanco. Osmoprotection of *Escherichia coli* by ectoine: uptake and accumulation characteristics. *J. Bacteriol.*, 174(15):5027–35, 1992.
- [106] Roy D. Sleator and Colin Hill. Bacterial osmoadaptation: The role of osmolytes in bacterial stress and virulence. *FEMS Microbiol. Rev.*, 26(1):49–71, 2002.
- [107] Tomoya Baba, Takeshi Ara, Miki Hasegawa, Yuki Takai, Yoshiko Okumura, Miki Baba, Kirill A Datsenko, Masaru Tomita, Barry L Wanner, and Hirotsada Mori. Construction of *Escherichia coli* K-12 in-frame, single-gene knockout mutants: the Keio collection. *Mol. Syst. Biol.*, 2:2006.0008, 2006.
- [108] Teuta Pilizota and Joshua W. Shaevitz. Plasmolysis and cell shape depend on solute outer-membrane permeability during hyperosmotic shock in *E.coli*. *Biophys. J.*, 104(12):2733–2742, 2013.
- [109] Bradley R. Parry, Ivan V. Surovtsev, Matthew T. Cabeen, Corey S. O’Hern, Eric R. Dufresne, Christine Jacobs-Wagner, Corey S. O’Hern, Eric R. Dufresne, and Christine Jacobs-Wagner. The bacterial cytoplasm has glass-like properties and is fluidized by metabolic activity. *Cell*, 156(1-2):183–194, jan 2014.
- [110] Thomas J. Silhavy, Michael L. Berman, and Lynn W. Enquist. *Experiments with gene fusions*. Cold Spring Harbor Laboratory Press, 1984.
- [111] M9 minimal medium (standard). *Cold Spring Harb. Protoc.*, 2010(8):pdb.rec12295, aug 2010.
- [112] M9 Salts. *Cold Spring Harb. Protoc.*, 2006(1):pdb.rec614, jun 2006.
- [113] Frederick C Neidhardt, Philip L Bloch, and David F Smith. Culture medium for enterobacteria. *J Bacteriol*, 119(3):736–747, 1974.
- [114] Peter S Swain, Keiran Stevenson, Allen Leary, Luis F. Montano-Gutierrez, Ivan B.N. N Clark, Jackie Vogel, and Teuta Pilizota. Inferring time derivatives including cell growth rates using Gaussian processes. *Nat. Commun.*, 7:13766, dec 2016.
- [115] Yao Kuan Wang, Ekaterina Krasnopeevea, Ssu-Yuan Lin, Fan Bai, Teuta Pilizota, and Chien-Jung Lo. Comparison of *Escherichia coli* surface attachment methods for in vivo single-cell microscopy. *Prep.*, 2019.

- [116] Renata Buda, Yunxiao Liu, Jin Yang, Smitha Hegde, Keiran Stevenson, Fan Bai, and Teuta Pilizota. Dynamics of *Escherichia coli* 's passive response to a sudden decrease in external osmolarity. *Proc. Natl. Acad. Sci.*, 113(40):E5838–E5846, oct 2016.
- [117] Gary L. Peterson. A simplification of the protein assay method of Lowry et al. which is more generally applicable. *Anal. Biochem.*, 83(2):346–356, dec 1977.
- [118] S. Benthin, J. Nielsen, and J. Villadsen. A simple and reliable method for the determination of cellular RNA content. *Biotechnol. Tech.*, 5(1):39–42, 1991.
- [119] A. Einstein. Über die von der molekularkinetischen Theorie der Wärme geforderte Bewegung von in ruhenden Flüssigkeiten suspendierten Teilchen [AdP 17, 549 (1905)]. *Ann. Phys.*, 19(4):371–381, 1906.
- [120] Marshall Fixman. Radius of gyration of polymer chains. *J. Chem. Phys.*, 36(2):306–310, jan 1962.
- [121] David R. Latulippe and Andrew L. Zydney. Radius of gyration of plasmid DNA isoforms from static light scattering. *Biotechnol. Bioeng.*, 107(1):134–142, may 2010.
- [122] John C. Crocker and David G. Grier. Methods of digital video microscopy for colloidal studies. *J. Colloid Interface Sci.*, 179(1):298–310, apr 1996.
- [123] Keiran Stevenson, Alexander F. McVey, Ivan B N Clark, Peter S Swain, and Teuta Pilizota. General calibration of microbial growth in microplate readers. *Sci. Rep.*, 6(1):38828, dec 2016.
- [124] Olaf Ronneberger, Philipp Fischer, and Thomas Brox. U-net: Convolutional networks for biomedical image segmentation. In *Lect. Notes Comput. Sci. (including Subser. Lect. Notes Artif. Intell. Lect. Notes Bioinformatics)*, volume 9351, pages 234–241, 2015.
- [125] Martín Abadi, Ashish Agarwal, Paul Barham, Eugene Brevdo, Zhifeng Chen, Craig Citro, Greg S Corrado, Andy Davis, Jeffrey Dean, Matthieu Devin, Sanjay Ghemawat, Ian Goodfellow, Andrew Harp, Geoffrey Irving, Michael Isard, Yangqing Jia, Rafal Jozefowicz, Lukasz Kaiser, Manjunath Kudlur, Josh Levenberg, Dan Mané, Rajat Monga, Sherry Moore, Derek Murray, Chris Olah, Mike Schuster, Jonathon Shlens, Benoit Steiner, Ilya Sutskever, Kunal Talwar, Paul Tucker, Vincent Vanhoucke, Vijay Vasudevan, Fernanda Viégas, Oriol Vinyals, Pete Warden, Martin Wattenberg, Martin Wicke, Yuan Yu, Xiaoqiang Zheng, and Google Research. TensorFlow: Large-Scale Machine Learning on Heterogeneous Distributed Systems. Technical report, 2015.
- [126] Diederik P. Kingma and Jimmy Ba. Adam: A Method for Stochastic Optimization. In *ICLR 2015*, dec 2014.

- [127] François Chollet and Others. Keras. [\url{https://keras.io}](https://keras.io), 2015.
- [128] Herbert Bay, Tinne Tuytelaars, and Luc Van Gool. SURF: Speeded up robust features. In *Lect. Notes Comput. Sci. (including Subser. Lect. Notes Artif. Intell. Lect. Notes Bioinformatics)*, volume 3951 LNCS, pages 404–417. Springer, Berlin, Heidelberg, 2006.
- [129] X Ester, M., Kriegel, H. P., Sander, J., & Xu. A Density-Based Algorithm for Discovering Clusters in Large Spatial Databases with Noise. *Kdd*, 96(34):226–231, 1996.
- [130] Peter; Simpson Bell and Ko Ching-Whan. Bioreactor for syngas fermentation. 002(15):354, 2014.
- [131] Prem B Parajuli, Y Deng, H Kim, and F Yu. Cost Analysis Model for Syngas Production Cost Evaluation Using the Graphical User Interface. *Energy and Power*, 4(2):35–40, 2014.
- [132] Wei Dong Huang and Y. H. Percival Zhang. Analysis of biofuels production from sugar based on three criteria: Thermodynamics, bioenergetics, and product separation. *Energy Environ. Sci.*, 4(3):784–792, 2011.
- [133] Jie Gao. *Development of Low Cost Medium for Ethanol Production From Syngas by Clostridium Ragsdalei*. PhD thesis, Oklahoma State University, 2012.
- [134] P. I. Larsen, L. K. Sydnes, B. Landfald, and A R Strøm. Osmoregulation in *Escherichia coli* by accumulation of organic osmolytes: betaines, glutamic acid, and trehalose. *Arch. Microbiol.*, 147(1):1–7, feb 1987.
- [135] S. Cayley, B. A. Lewis, and M. T. Record. Origins of the osmoprotective properties of betaine and proline in *Escherichia coli* K-12. *J. Bacteriol.*, 174(5):1586–1595, mar 1992.
- [136] Sarah Huffer, Melinda E. Clark, Jonathan C Ning, Harvey W Blanch, and Douglas S Clark. Role of Alcohols in Growth, Lipid Composition, and Membrane Fluidity of Yeasts, Bacteria, and Archaea. *Appl. Environ. Microbiol.*, 77(18):6400–6408, 2011.
- [137] L. O. Ingram. Regulation of fatty acid composition in *Escherichia coli*: A proposed common mechanism for changes induced by ethanol, chaotropic agents, and a reduction of growth temperature. *J. Bacteriol.*, 149(1):166–172, 1982.
- [138] Jes Forchhammer and Lasse Lindahl. Growth rate of polypeptide chains as a function of the cell growth rate in a mutant of *Escherichia coli* 15. *J. Mol. Biol.*, 55(3):563–568, feb 1971.
- [139] Patrick P. Dennis and Hans Bremer. Modulation of Chemical Composition and Other Parameters of the Cell at Different Exponential Growth Rates. *EcoSal Plus*, 3(1), sep 2008.

- [140] Marcel H. Zwietering, I Jongenburger, F M Rombouts, and K van 't Riet. Modeling of the bacterial growth curve. *Appl. Environ. Microbiol.*, 56(6):1875–81, jun 1990.
- [141] Teresa J Broering, Michelle M Arnold, Cathy L Miller, Jessica A Hurt, Patricia L Joyce, and Max L Nibert. Carboxyl-Proximal Regions of Reovirus Nonstructural Protein NS Necessary and Sufficient for Forming Factory-Like Inclusions. *J. Virol.*, 79(10):6194–6206, may 2005.
- [142] Andrea Y. Weiße, Diego A. Oyarzún, Vincent Danos, and Peter S. Swain. Mechanistic links between cellular trade-offs, gene expression, and growth. *Proc. Natl. Acad. Sci. U. S. A.*, 112(9):E1038–47, mar 2015.
- [143] Yuichi Taniguchi, Paul J Choi, Gene-Wei Li, Huiyi Chen, Mohan Babu, Jeremy Hearn, Andrew Emili, and X Sunney Xie. Quantifying *E.coli* proteome and transcriptome with single-molecule sensitivity in single cells. *Science*, 329(5991):533–8, jul 2010.
- [144] Ingrid M Keseler, Julio Collado-Vides, Alberto Santos-Zavaleta, Martin Peralta-Gil, Socorro Gama-Castro, Luis Muniz-Rascado, César Bonavides-Martinez, Suzanne Paley, Markus Krummenacker, Tomer Altman, Pallavi Kaipa, Aaron Spaulding, John Pacheco, Mario Latendresse, Carol Fulcher, Malabika Sarker, Alexander G Shearer, Amanda Mackie, Ian Paulsen, Robert P Gunsalus, and Peter D Karp. EcoCyc: A comprehensive database of *Escherichia coli* biology. *Nucleic Acids Res.*, 39(SUPPL. 1):583–590, 2011.
- [145] Florian Brandt, Stephanie A. Etchells, Julio O. Ortiz, Adrian H. Elcock, F. Ulrich Hartl, and Wolfgang Baumeister. The Native 3D Organization of Bacterial Polysomes. *Cell*, 136(2):261–271, jan 2009.
- [146] K. Dornmair, P. Overath, and F. Jahnig. Fast measurement of galactoside transport by lactose permease. *J. Biol. Chem.*, 264(1):342–346, 1989.
- [147] Kathy R. Albe, Margaret H. Butler, and Barbara E. Wright. Cellular concentrations of enzymes and their substrates. *J. Theor. Biol.*, 143(2):163–195, mar 1990.
- [148] The MathWorks Inc. MATLAB and Statistics Toolbox, 2010.
- [149] Stefan Klumpp, Matthew Scott, Steen Pedersen, and Terence Hwa. Molecular crowding limits translation and cell growth. *Proc. Natl. Acad. Sci. U. S. A.*, 110(42):16754–9, 2013.
- [150] Tapomoy Bhattacharjee and Sujit S Datta. Bacterial hopping and trapping in porous media. *Nat. Commun.*, 10(1):2075, dec 2019.
- [151] Jan Spitzer and Bert Poolman. How crowded is the prokaryotic cytoplasm? *FEBS Lett.*, 587(14):2094–2098, 2013.